Optical Properties of the Waters of the Strait of Georgia, BC, Canada

by

Eduardo Loos
B.Sc., Universidade do Estado do Rio de Janeiro, 1997
M.Sc., University of Victoria, 2002

A Dissertation Submitted in Partial Fulfillment
of the Requirements for the Degree of

DOCTOR OF PHILOSOPHY

in the Department of Geography

Supervisory Committee

Optical Properties of the Waters of the Strait of Georgia, BC, Canada

by

Eduardo Loos
B.Sc., Universidade do Estado do Rio de Janeiro, 1997
M.Sc., University of Victoria, 2002

Supervisory Committee

Dr. Maycira Costa, Department of Geography
Supervisor

Dr. Olaf Niemann, Department of Geography
Departmental Member

Dr. Sophia Johannessen, Department of Geography
Departmental Member

Dr. Alexandre Brolo, Department of Chemistry
Outside Member

Abstract

Supervisory Committee
Dr. Maycira Costa, Department of Geography
Supervisor
Dr. Olaf Niemann, Department of Geography
Departmental Member
Dr. Sophia Johannessen, Department of Geography
Departmental Member
Dr. Alexandre Brolo, Department of Chemistry
Outside Member

Ocean optical studies have been conducted extensively in open ocean waters but less so in coastal waters where the influence of human population is increasing dramatically. The waters of the Strait of Georgia, British Columbia, Canada, are very important to the rearing of young salmon and herring, and to the fishing industry of British Columbia overall. The oceanography and plankton communities of the Strait have been researched extensively, however the forces behind the frequent occurrence of phytoplankton blooms in these waters still causes debate among researchers. In order to shed some light onto this topic and increase our knowledge of the characteristics of the waters of the Strait of Georgia, optical and bio-physical data were measured in the euphotic waters of the Strait in late spring and early summer of 2006. Hyperspectral optical data were measured for the first time in these waters using *in situ* optical profilers to collect inherent optical properties and radiometric quantities that were later used to derive apparent optical properties. The inherent optical properties included absorption coefficient, spectral beam attenuation coefficient, chromophoric dissolved organic matter absorption coefficient, particulate absorption coefficient, and particulate scattering coefficient. *In situ* irradiances and radiances were used to derive various diffuse attenuation coefficients. Water masses in the euphotic zone of the Strait of Georgia were then classified into three optical water masses according to their inherent optical properties using a clustering algorithm. OM1 waters were characterized by high and spectrally-invariant particulate scattering due to inorganic particles carried by the Fraser River plume. Absorption and scattering showed some spectral dependence in OM2 waters, with particles and chromophoric dissolved organic matter contributing equally to light absorption. The deepest waters, OM3, were the least influenced by the Fraser River, and the contribution of chromophoric dissolved organic matter to absorption was greater than in OM1 and OM2.

A radiative transfer model, Hydrolight, was used to model some of the optical properties that were not collected *in situ* and then used to assess the magnitude of light available to phytoplankton in the Strait. Based on the minimum light requirements for photosynthesis of two of the main phytoplankton species in the Strait, the analysis presented here showed that there was enough light available for photosynthesis in the photosynthetically-available radiation range for the two phytoplankton species in all three optical water masses.

Table of Contents

List of Tables

List of Figures

List of Symbols

Symbol	Name	Units
	Fundamental Quantities and other symbols	
A	Area	m^2
B_{wd}	Wavelength-dependence of the backscattering coefficient	-
C	Chlorophyll concentration	μg L^{-1}
f_C	CDOM fluorescence	ppb QSDE
l	Cuvette length	m
λ	Wavelength	nm
r	Distance	m
S	CDOM slope	nm^{-1}
$\overline{S}$	Average CDOM slope	nm^{-1}
z	Geometric depth	m
$Z_{1\%}$	Depth of 1% irradiance	m
Z_c	Irradiance compensation depth	m
t	Time	s
τ	Optical depth	-
V	Volume	L
Ξ	Upward and downward directions	-
Ξ_u	Hemisphere of upward directions	-

Symbol	Name	Units
	Fundamental Quantities and other symbols	
Ξ_d	Hemisphere of downward directions	-
ϕ	Azimuthal angle	rd or deg
θ	Nadir (polar) angle	rd or deg
ψ	Scattering angle	rd or deg
Ω	Solid angle	sr
	Radiometric Quantities	
Q	Quantity of radiant energy	J
Φ_i	Incident (total) radiant power	W
Φ_a	Absorbed radiant power	W
Φ_s	Scattered radiant power	W
Φ_t	Transmitted radiant power	W
L	Radiance	W m^{-2} sr^{-1}
L_u	Upwelling radiance	W m^{-2} sr^{-1}
E	Irradiance	W m^{-2}
E_s	Above-water downwelling irradiance	W m^{-2}
E_d	In-water downwelling irradiance	W m^{-2}
E_u	In-water upwelling irradiance	W m^{-2}
E_o	Scalar irradiance	W m^{-2}
E_{od}	Downwelling scalar irradiance	W m^{-2}
E_{ou}	Upwelling scalar irradiance	W m^{-2}

Symbol	Name	Units
	Radiometric Quantities	
E_c	Compensation irradiance	μE m^{-2} s^{-1} or W m^{-2}
	Inherent Optical Properties	
A	Absorptance	-
B	Scatterance	-
T	Transmittance	-
a	Absorption coefficient	m^{-1}
a_T	Measured total absorption coefficient	m^{-1}
a_t	Measured total absorption coefficient without water absorption coefficient	m^{-1}
$a_{t'}$	Scattering-corrected absorption coefficient	m^{-1}
a_w	Water absorption coefficient	m^{-1}
a_p	Particulate absorption coefficient	m^{-1}
$a_{p'}$	Scattering-corrected particulate absorption coefficient	m^{-1}
a_C	CDOM absorption coefficient	m^{-1}
$a_{c'}$	Scattering-corrected CDOM absorption coefficient	m^{-1}
a_{phy}	Phytoplankton absorption coefficient	m^{-1}
a_{min}	Mineral/inorganic absorption coefficient	m^{-1}
a_{chl}	Modelled chlorophyll absorption coefficient	m^{-1}
a^*_{chl}	Chlorophyll-specific absorption coefficient	m^2 μg^{-1}
a_{CDOM}	Spectrophotometric CDOM absorption coefficient	m^{-1}

Symbol	Name	Units
	Inherent Optical Properties	
a_{Cspec}	Fitted spectrophotometric CDOM absorption coefficient	m^{-1}
b	Scattering coefficient	m^{-1}
b_T	Total scattering coefficient	m^{-1}
$b_{t'}$	Total scattering coefficient without water scattering coefficient	m^{-1}
b_w	Water scattering coefficient	m^{-1}
b_p	Particulate scattering coefficient	m^{-1}
$b_{p'}$	Particulate scattering coefficient without water scattering coefficient	m^{-1}
b_{phy}	Phytoplankton scattering coefficient	m^{-1}
b_{min}	Mineral/inorganic scattering coefficient	m^{-1}
b_b	Backscattering coefficient	m^{-1}
b_{bt}	Modelled total backscattering coefficient	m^{-1}
b_{bw}	Modelled pure water backscattering coefficient	m^{-1}
$b_{b'}$	Modelled particulate backscattering coefficient	m^{-1}
c	Beam attenuation coefficient	m^{-1}
c_T	Measured total beam attenuation coefficient	m^{-1}
c_t , $c_{t'}$	Measured total beam attenuation coefficient without water beam attenuation coefficient	m^{-1}
c_w	Pure water beam attenuation coefficient	m^{-1}
c_p	Particulate beam attenuation coefficient	m^{-1}
c_C	CDOM attenuation coefficient	m^{-1}

Symbol	Name	Units
	Inherent Optical Properties	
β	Volume scattering function (VSF)	m^{-1} sr^{-1}

Symbol	Name	Units
	Apparent Optical Properties	
R_r	Radiance reflectance	sr^{-1}
K_{Ed}	Downwelling irradiance attenuation coefficient	m^{-1}
K_{Lu}	Upwelling radiance attenuation coefficient	m^{-1}
K_{Eo}	Scalar irradiance attenuation coefficient	m^{-1}
$\overline{K}_{Eo}$	Mean scalar irradiance attenuation coefficient	m^{-1}
$\overline{\mu}$	Average cosine	-
$\overline{\mu}_d$	Average downwelling cosine	-
$\overline{\mu}_u$	Upwelling average cosine	-

List of Acronyms and Abbreviations

Acronym	Name
ac-S	Hyperspectral Absorption-attenuation Meter
AOP	Apparent Optical Property
C	Chlorophyll concentration
C-cline	Attenuation Cline
CDOM	Chromophoric Dissolved Organic Matter
Chl *a*	Chlorophyll *a*
CTD	Conductivity-Temperature-Depth
DI	Deionised Water
DOC	Dissolved Organic Carbon
DOM	Dissolved Organic Matter
FF	Fournier-Forand
GF/F	Glass-fibre Filter
HPLC	High-performance Liquid Chromatography
HyperPRO	Hyperspectral Profiler
IOP	Inherent Optical Property
Minispec OCR	Miniature Hyperspectral Ocean Colour Radiometer
MSV	Marine Science Vessel
OM	Optical Water Mass

Acronym	Name
PAR	Photosynthetically-available Radiation
ppb	Parts per billion
QSDE	Quinine Sulphate Dihydrate Equivalent
SoG	Strait of Georgia
S.D.	Standard Deviation
TSM	Total Suspended Material
VSF	Volume Scattering Function

Acknowledgements

This dissertation would not have been successful without those who were kind enough to provide me with lots of support. I would like to thank all of my committee members, Maycira Costa (Geography, UVic), Sophie Johannessen (Institute of Ocean Sciences), Olaf Niemann (Geography, UVic), and Alexandre Brolo (Chemistry, UVic) for their assistance and guidance. Thanks also to NSERC for providing the funding for the ship time.

Nick Komick and Jenn O'Neill (Geography, UVic) were exceptional during my cruises. Akash Sastri, Rana El-Sabaawi, John Dower, and Damian Grundle (Biology, UVic) allowed me to borrow their Niskin bottles for water collection. Scott Scholz (Biochemistry, UVic) allowed me to use their deep freezer to store my photosynthetic pigment samples. Ricardo Rossin (SEOS, UVic) improved our HPLC procedure and adapted it to my needs. Melanie Quenneville (Institute of Ocean Sciences) offered her expertise in HPLC to help me understand the complexities of pigment analysis. Cynthia Wright (Institute of Ocean Sciences) kindly shared her BC coastline vectors for the ODV software. Thiago Silva, Chris Piller, and Laurie Gallagher were great lab mates and offered their precious time whenever I needed it the most. Captain Ken Brown, Ian Blazey, and the crew of the MSV Strickland were incredibly accommodating and great fun to work with.

The optical sensors and their accompanying software I used were not easy to handle and the folks at Satlantic and WET Labs were extremely helpful in solving any issues. My deepest thanks go to Darrel Adams, Cyril Dempsey, Marlon Lewis (Satlantic, Inc.), Ian Walsh, Dave Stahlke, and Dave Romanko (WET Labs, Inc.). Dan Paradis (Anachemia) and Mark Rushforth (Dionex) were vital in setting up the water purification system and the HPLC, respectively.

Hydrolight and Ocean Data View were fundamental programs for my analysis and I would not have presented any results without the priceless assistance of Curtis Mobley, Lydia Sundman (Sequoia, Inc.), and Reiner Schlitzer (Alfred Wegener Institut für Polarund Meeresforschung). The email discussions with David McKee (University of Strathclyde) over ocean optics helped me very much whenever I felt at a dead end.

I would not have survived the university bureaucracy without Kathie Merriam, Diane Braithwaite, Darlene Li, Jill Jahansoozi, and Marta Ausio-Esteve. Computer, network, and software licence issues were solved by Rick Sykes. Sarwan Dillon (Purchasing, UVic) helped me navigate the ins and outs of buying equipment for the lab and my analyses.

I must also thank the Geography faculty at UVic for all of their support, especially Rosaline Canessa, Doug Porteous, Ian Walker, Trisalyn Nelson, and Dan Smith. Dariusz Stramski (University of California) and Robert Bukata (Environment Canada) also provided some needed advice.

My mother Consuelo, my brothers Rudi and Rafa, my in-laws Jane and David, and all of my relatives gave me the strength I needed to accomplish this goal. My wife Sarah has always been at my side through all the dark and less memorable moments of this endeavour and for this I am eternally grateful.

Thank you all.

Eddie Loos
July 2008
Victoria, BC

Chapter 1: Introduction

1.1 General Introduction

The field of optical oceanography has seen an increase in research in the second half of the last century fuelled by the development of new methods and technology (Dickey, 2002; Dickey *et al.*, 2006). In addition, existing sensors for measuring and monitoring processes that control the interactions of light with ocean water have also improved (Dickey, 1991; Dickey, 2003). Because light and its utilization are fundamental to life in the oceans, it is important to realize that light will not only interact with living organisms but also with particulate and dissolved matter in the ocean. The degree of these interactions, which are dependent on the absorption and scattering of light, is responsible for the colour of the ocean.

Recently, coastal oceans have received increasing attention from scientific research because of their importance to human populations. The world's population living within the coastal zone is, arguably, somewhere between 37% and 60%, according to Cohen *et al.* (1997) and World Resources Institute (1996), respectively. The coastal zone is important to the human population because of the proximity to the oceans and the resources and benefits they provide, such as fisheries, transport of goods, recreation, and defence, to name a few.

Most studies on ocean optical properties have been conducted in the open ocean, where roughly 98% of the world's oceans characteristics are dominated by phytoplankton (Li *et al.*, 2000; Hooker *et al.*, 2004). The remaining 2% constitute coastal waters of high ecological and economic importance, which are optically dominated by a complex assemblage of organic and inorganic matter. This complex assemblage has hindered the use of ocean colour satellites and remotely-sensed optical data for deriving biogeophysical quantities (Frette *et al.*, 1998; Bergmann *et al.*, 2004; Chang *et al.*, 2006). Nevertheless, optical data have been used for coastal studies (Jerlov, 1976; Doxaran *et al.*, 2006) and optical classification of water bodies (Chang *et al.*, 2002; Reinart *et al.*, 2003), thus providing information on marine primary productivity (Oliver *et al.*, 2004), fisheries (Laurs, 1989; Santos, 2000; Ware & Thomson, 2005), coastal sedimentation and sediment dispersal (Griffin & Kellogg, 2004; Bowers & Binding, 2006), harmful algal blooms (Cullen *et al.*, 1997; Barocio-León *et al.*, 2008), organic matter content (Højerslev *et al.*, 1996; Chen *et al.*, 2004; Coble, 2007), raw sewage disposal (Baker & Spencer, 2004), and pollution (Arst, 2003).

Life on earth depends on the ability of phytoplankton to use light to synthesize organic compounds from inorganic materials, a process known as photosynthesis (Lalli & Parsons, 1997). Marine primary productivity is the rate of formation of such organic compounds and varies considerably depending on seasons, geographical location, nutrient concentration, temperature, depth, currents, vertical mixing, and light availability (Nybakken, 1988). Photosynthesis would not be possible without light. However, it is not so much the availability of light that is relevant as the magnitude and quality of the available light that will determine if phytoplankton communities will flourish (Levinton, 2001). Water absorbs visible light (400-700 nm), and consequently there is a decrease of light availability with depth. The presence of dissolved and particulate materials will also have an impact on the light fields because they will not only absorb but also scatter light. These effects are not constant throughout the electromagnetic spectrum but differ quite significantly according to the material interacting with the available light (Mobley, 1995). Chromophoric dissolved organic matter (CDOM) and total suspended material (TSM) play an important role in the attenuation of photosynthetically-available radiation (PAR, 400-700 nm), and therefore on primary productivity (Coble *et al.*, 2004). This has been demonstrated in several regions, such as the West Florida Shelf (Del Castillo *et al.*, 2000), the East Sound, WA (Twardowski & Donaghay, 2001), the Rhode River, MD (Gallegos & Neale, 2002), the Baltic Sea (Woźniak *et al.*, 2003), the Lower St. Johns River, FL (Gallegos, 2005), and the English Channel (Vantrepotte *et al.*, 2007).

CDOM competes with phytoplankton for photons, particularly in the blue region of the spectrum (~400-500 nm; Blough & Del Vecchio (2002)). Furthermore, the absorption of light by CDOM leads to the breakage of molecular bonds and the photochemical formation of chemically-different organic compounds (Schofield *et al.*, 2004) that can ultimately impact primary productivity (Bissett *et al.*, 2001). Suspended material also affects primary productivity by attenuating light necessary for photosynthesis (Van Duin *et al.*, 2001). TSM usually determines the magnitude of the beam attenuation ($c(z,\lambda)$) of coastal ocean waters, and is responsible for most of its temporal and spatial variability (Mobley, 1994). The magnitude of $c(z,\lambda)$ (where z is depth and λ is wavelength) is greater in estuarine areas than in open ocean waters because of the high concentrations of mineral particles. Similarly to other estuaries (Gallegos *et al.*, 2005; Doxaran *et al.*, 2006), high $c(z,\lambda)$ has been observed in the waters of the Strait of Georgia (SoG) under the influence of the Fraser River (Johannessen *et al.*, 2006). However, the relative contributions of particles and CDOM to light attenuation in the SoG are presently not known.

1.2 Research Goal and Objectives

The goal of this study was to combine optical data from *in situ* and laboratory measurements with modelling to provide the first quantitative analysis of the spatial variability of the inherent optical properties (IOPs) and apparent optical properties (AOPs) of the euphotic zone of the SoG. The three objectives of this research were:

1. To develop a method, which may be extrapolated to other coastal seas influenced by large riverine systems, for defining water masses according to their IOPs using cluster analysis;
2. To complement the optical characterization of the upper water masses of the SoG using radiometric quantities and AOPs; and
3. To assess light availability for primary productivity based on *in situ* and modelled AOPs, radiometric quantities, and IOPs. For this, a radiative transfer model, Hydrolight, was used.

Goal 1 was accomplished by the collection and analysis of *in situ* IOPs (attenuation and absorption of light by particulate and CDOM) within the euphotic zone of the SoG. In addition to these measurements, the concentrations of optical water constituents were also determined. Cluster analysis of the optical data was then performed and three distinct optical water masses were defined. Goal 2 consisted of the collection and analysis of radiometric quantities and AOPs and their descriptions for each optical water mass defined in Goal 1. Goal 3 was achieved by running a radiative transfer model, Hydrolight, to obtain IOPs and AOPs that had not been collected *in situ*, such as average cosine and scalar irradiance. Modelling results were then used in combination with *in situ* data to determine the light available for photosynthesis in the waters of the SoG.

The results presented here will provide baseline information to advance knowledge of how light is attenuated by particulate and dissolved constituents in coastal waters under the influence of a large riverine system. Furthermore, the optical characteristics of light attenuation will provide a better understanding of the light available for major phytoplankton groups for photosynthesis in the waters of the SoG. Finally, this study, being the first to provide a full description of the optical properties of the SoG, will enhance the body of knowledge surrounding the importance of light to the oceanography and ecology of the waters of the SoG.

1.3 Water Optics

Water optics, also known as hydrologic optics (Mobley, 1995), a sub-discipline of modern physics, is concerned with the quantitative description of the interactions of light with any water body, e.g. oceans, estuaries, lakes, and rivers. More specifically, the discipline of marine optics (Jerlov, 1976) or optical oceanography focuses solely on the description and quantification of optical properties of ocean waters. These water optical properties have been grouped into two classes (Preisendorfer, 1976): inherent optical properties and apparent optical properties. IOPs depend solely on the medium (ocean water, dissolved and particulate materials) and are not dependent on the ambient light field. On the other hand, AOPs depend on both the medium and the directional structure of the ambient light field.

To obtain IOPs, it is necessary to consider the total spectral radiant power $\Phi_i(\lambda)$ of a collimated monochromatic light beam (Equation 1) as the summation of the fraction of $\Phi_i(\lambda)$ that is absorbed, $\Phi_a(\lambda)$, within a small volume of water ΔV of thickness Δr, scattered, $\Phi_s(\lambda)$, out of the beam at a certain angle ψ, and transmitted, $\Phi_t(\lambda)$, through ΔV without change in direction (Mobley, 1995).

$$\Phi_i(\lambda) = \Phi_a(\lambda) + \Phi_s(\lambda) + \Phi_t(\lambda) \ \ (\mathrm{W\ nm^{-1}}) \qquad (1)$$

The fractions of power yield spectral absorptance $A(\lambda)$, spectral scatterance $B(\psi,\lambda)$, and spectral transmittance $T(\lambda)$ (Equations 2-4).

$$A(\lambda) = \frac{\Phi_a(\lambda)}{\Phi_i(\lambda)} \tag{2}$$

$$B(\psi,\lambda) = \frac{\Phi_s(\psi,\lambda)}{\Phi_i(\lambda)} \tag{3}$$

$$T(\lambda) = \frac{\Phi_t(\lambda)}{\Phi_i(\lambda)} \tag{4}$$

Spectral absorption and scattering coefficients (*a(λ)* and *b(λ)*, respectively) (Equations 5 and 6) can then be described as spectral absorptance and scatterance per unit distance Δr in water, respectively.

$$a(\lambda) = \lim_{\Delta r \to 0} \frac{A(\lambda)}{\Delta r} \ (\mathrm{m}^{-1}) \tag{5}$$

$$b(\lambda) = \lim_{\Delta r \to 0} \frac{B(\lambda)}{\Delta r} \ (\mathrm{m}^{-1}) \tag{6}$$

Scattering *b(λ)* is the summation of forward, $b_f(\lambda)$, and backward, $b_b(\lambda)$, scattering coefficients. The backward scattering coefficient is also known as backscattering coefficient and is calculated as

$$b_b(\lambda) = 2\pi \int_{\pi/2}^{\pi} \beta(\psi,\lambda) sin\psi \, d\psi \ (\mathrm{m}^{-1}) \tag{7}$$

where

$$\beta(\psi,\lambda) = \lim_{\Delta r\to 0}\lim_{\Delta\Omega\to 0}\frac{B(\psi,\lambda)}{\Delta r\Delta\Omega} = \lim_{\Delta r\to 0}\lim_{\Delta\Omega\to 0}\frac{\Phi_s(\psi,\lambda)}{\Phi_i(\lambda)\Delta r\Delta\Omega}\ (\mathrm{m^{-1}\ sr^{-1}}) \tag{8}$$

is the volume scattering function (VSF), ψ is the scattering angle, and $\Delta\Omega$ is the solid angle in steradians.

The spectral beam attenuation coefficient, $c(\lambda)$, is then given by

$$c(\lambda) = a(\lambda) + b(\lambda)\ (\mathrm{m^{-1}}) \tag{9}$$

To understand AOPs, it is necessary to explore the various radiometric quantities used to calculate them. Radiance, L, is the most important radiometric quantity in hydrologic optics simply because it provides a detailed description of the light field: positional, temporal, directional, and spectral characteristics (Equation 10).

$$L(x,y,z,t,\theta,\phi,\lambda) = \frac{\Delta Q}{\Delta t\Delta A\Delta\Omega\Delta\lambda}\qquad (\mathrm{J\ s^{-1}\ m^{-2}\ sr^{-1}\ nm^{-1}}) \tag{10}$$

where

$L(x,y,z,t,\theta,\phi,\lambda)$ is radiance as a function of space (x, y, z), time (t), nadir angle (θ), azimuthal angle (ϕ), and wavelength (λ);

ΔQ is the quantity of incident radiant energy;

Δt is the time interval centered at t;

ΔA is the surface area located at x, y, z;

$\Delta\Omega$ is the solid angle as a function of θ and ϕ normal to ΔA containing all the directions through which the incident energy arrives; and

$\Delta\lambda$ is the wavelength of the incident energy centered on wavelength λ.

Irradiance, *E*, differs from radiance by measuring the energy flux over an entire hemisphere of directions, instead of restricting the collection to a certain solid angle (Equation 11).

$$E_d(z,\lambda) = \frac{\Delta Q}{\Delta A \Delta\lambda} \quad (\mathrm{W\ m^{-2}\ nm^{-1}}) \tag{11}$$

where

$E_d(z,\lambda)$ is the spectral downward plane irradiance (also known as spectral downwelling irradiance) taken with the spectrometer pointing upward.

Light beams that reach a planar irradiance sensor at oblique angles must be corrected for the angle of incidence at the surface (cosine law for irradiance) (Equation 12):

$$E_d(z,\lambda) = \int_{\Xi d} L(z,\theta,\phi,\lambda)\,|\cos\theta|\,d\Omega \quad (\mathrm{W\ m^{-2}\ nm^{-1}}) \tag{12}$$

where

Ξ_d denotes the hemisphere of downward directions such that $0 \leq \theta \leq \pi/2$ and $0 \leq \phi \leq 2\pi$, with θ measured from nadir.

E_u is collected by turning the spectrometer upside down:

$$E_u(z,\lambda) = \int_{\Xi u} L(z,\theta,\phi,\lambda)\,|\cos\theta|\,d\Omega \quad (\mathrm{W\ m^{-2}\ nm^{-1}}) \tag{13}$$

where E_u is the spectral upward plane irradiance and Ξ_u denotes the hemisphere of upward directions such that $0 \leq \theta \leq \pi/2$ and $0 \leq \phi \leq 2\pi$, with θ measured from zenith.

By using a spherical sensor, all photons reach the sensor's surface at perpendicular angles. Thus, scalar irradiance, $E_o(z,\lambda)$, is the summation of radiances over all directions (Equation 14).

$$E_{od}(z,\lambda)+E_{ou}(z,\lambda)=E_o(z,\lambda)=\int_{\Xi} L(z,\theta,\phi,\lambda)d\Omega \quad (\mathrm{W\ m^{-2}\ nm^{-1}}) \tag{14}$$

where E_{od} is the spectral downward scalar irradiance (Equation 15) and E_{ou} is the spectral upward scalar irradiance (Equation 16).

$$E_{od}(z,\lambda)=\int_{\Xi d} L(z,\theta,\phi,\lambda)d\Omega \quad (\mathrm{W\ m^{-2}\ nm^{-1}}) \tag{15}$$

$$E_{ou}(z,\lambda)=\int_{\Xi u} L(z,\theta,\phi,\lambda)d\Omega \quad (\mathrm{W\ m^{-2}\ nm^{-1}}) \tag{16}$$

The photosynthetically available radiation (PAR) is given by

$$E_o(z,PAR)=\int_{400nm}^{700nm} \frac{\lambda}{hc}E_o(z,\lambda)d\lambda \quad (\mathrm{\mu E\ m^{-2}\ s^{-1}}) \tag{17}$$

where

$h = 6.625 \cdot 10^{-34}$ J s is Planck's constant;

$c = 2.998 \cdot 10^{8}$ m s^{-1} is the speed of light in the vacuum.

$E_o(z,PAR)$ is usually given in unit μE m^{-2} s^{-1} where 1 mole of photons equals 1 E (Einstein).

Multiplying $\frac{\lambda}{hc}$ by E_0 (Watts) converts the energy units into quantum units (E s^{-1}). It is important to note that the number of photons and not their total energy is what is relevant to the chemical transformations generated by photosynthesis. Any photons within the visible wavelength range induce the same chemical transformations independently of wavelength (Mobley, 1994).

AOPs are derived from the radiometric quantities, which makes them dependent on the ambient radiance distribution of a water body. The radiance reflectance, $R_r(z,\lambda)$, is computed as

$$R_r(z,\lambda) = \frac{L_u(z,\lambda)}{E_d(z,\lambda)} \ (\mathrm{sr}^{-1}) \tag{18}$$

where $L_u(z,\lambda)$ is the upwelling radiance.

The spectral diffuse attenuation coefficient for spectral downwelling irradiance, $K_{Ed}(z,\lambda)$, is given by

$$K_{Ed}(z,\lambda) = -\frac{1}{E_d(z,\lambda)} \frac{dE_d(z,\lambda)}{dz} \ (\mathrm{m}^{-1}) \tag{19}$$

Analogously, the spectral diffuse attenuation coefficient for spectral upwelling radiance, $K_{Lu}(z,\lambda)$, is given by

$$K_{Lu}(z,\lambda) = -\frac{1}{L_u(z,\lambda)}\frac{dL_u(z,\lambda)}{dz} \text{ (m}^{-1}\text{)} \tag{20}$$

Another important AOP is the spectral average cosine, $\bar{\mu}(z,\lambda)$, which describes the total irradiance distribution and is given by

$$\bar{\mu}(z,\lambda) = \frac{E_d(z,\lambda) - E_u(z,\lambda)}{E_o(z,\lambda)} \tag{21}$$

The spectral average cosine can be decomposed into spectral downwelling average cosine, $\bar{\mu}_d(z,\lambda)$, and spectral upwelling average cosine, $\bar{\mu}_u(z,\lambda)$, according to

$$\bar{\mu}_d(z,\lambda) = \frac{E_d(z,\lambda)}{E_{od}(z,\lambda)} \tag{22}$$

$$\bar{\mu}_u(z,\lambda) = \frac{E_u(z,\lambda)}{E_{ou}(z,\lambda)} \tag{23}$$

Values for the spectral average cosine range from -1 to +1; when $\bar{\mu}(z,\lambda) = 0$, the radiance distribution is isotropic (diffuse), and when $\bar{\mu}(z,\lambda) = -1$ or $\bar{\mu}(z,\lambda) = 1$, the radiance distribution is said to be composed of collimated beams in a particular direction (Mobley, 1994).

Lastly, depth can also be explained in terms of the inherent optical properties of a water body (Mobley, 1994). The relationship between the geometric depth, z, and the optical depth, τ, is given by

$$d\tau = c(z,\lambda)\, dz \tag{24}$$

Consequently, completely transparent waters would have an optical depth of zero and waters containing particles and dissolved substances would have optical depths greater than zero.

1.4 Area of Study

The Strait of Georgia in British Columbia, Canada (Figure 1), is approximately 222 km long and 28 km wide with an average depth of 155 m (Thomson, 1981). The movement of water in this system is dominated by estuarine circulation characterized by a two-layer exchange flow driven by strong freshwater discharge, particularly from the Fraser River, i.e., a seaward (southward) surface flow with lower salinity and a landward (northward) subsurface flow carrying more saline and nutrient-rich waters from the Pacific Ocean to the SoG (Li *et al.*, 2000). Intense tidal mixing occurs in Haro Strait and at Boundary Pass, where nutrient-rich deeper waters from the Pacific Ocean are mixed with surface waters (Masson & Cummins, 2004). This region is also influenced by semi-diurnal tides and seasonal variation in wind patterns and riverine discharge (Tully & Dodimead, 1957; Waldichuk, 1957).

Approximately 75% of freshwater runoff into the SoG is attributed to the Fraser River, which has the third largest discharge in the Northeastern Pacific Ocean and is the largest source of sediment on the west coast of North America (Thomson, 1981). The discharge of the Fraser River is dominated by snowmelt, leading to low winter and high summer discharge, with a strong freshet in June each year (Environment Canada, 2006). This high discharge enters the SoG in the form of a riverine plume, which carries high loads of inorganic suspended matter and dissolved matter into the waters of the SoG (Johannessen *et al.*, 2003). The inorganic suspended matter is classified into wash load and bed-material load, the former constituted of clays, silts, and very fine sand in continuous suspension, and the latter formed by coarser bed material that is often transported along the bottom (Kostaschuk *et al.*, 1998). Most of this material sinks to the bottom, where it tends to be trapped in sediments of the SoG (Johannessen *et al.*, 2005). The greatest light attenuation due to suspended matter occurs in surface waters, particularly in the spring and summer (Johannessen *et al.*, 2006).

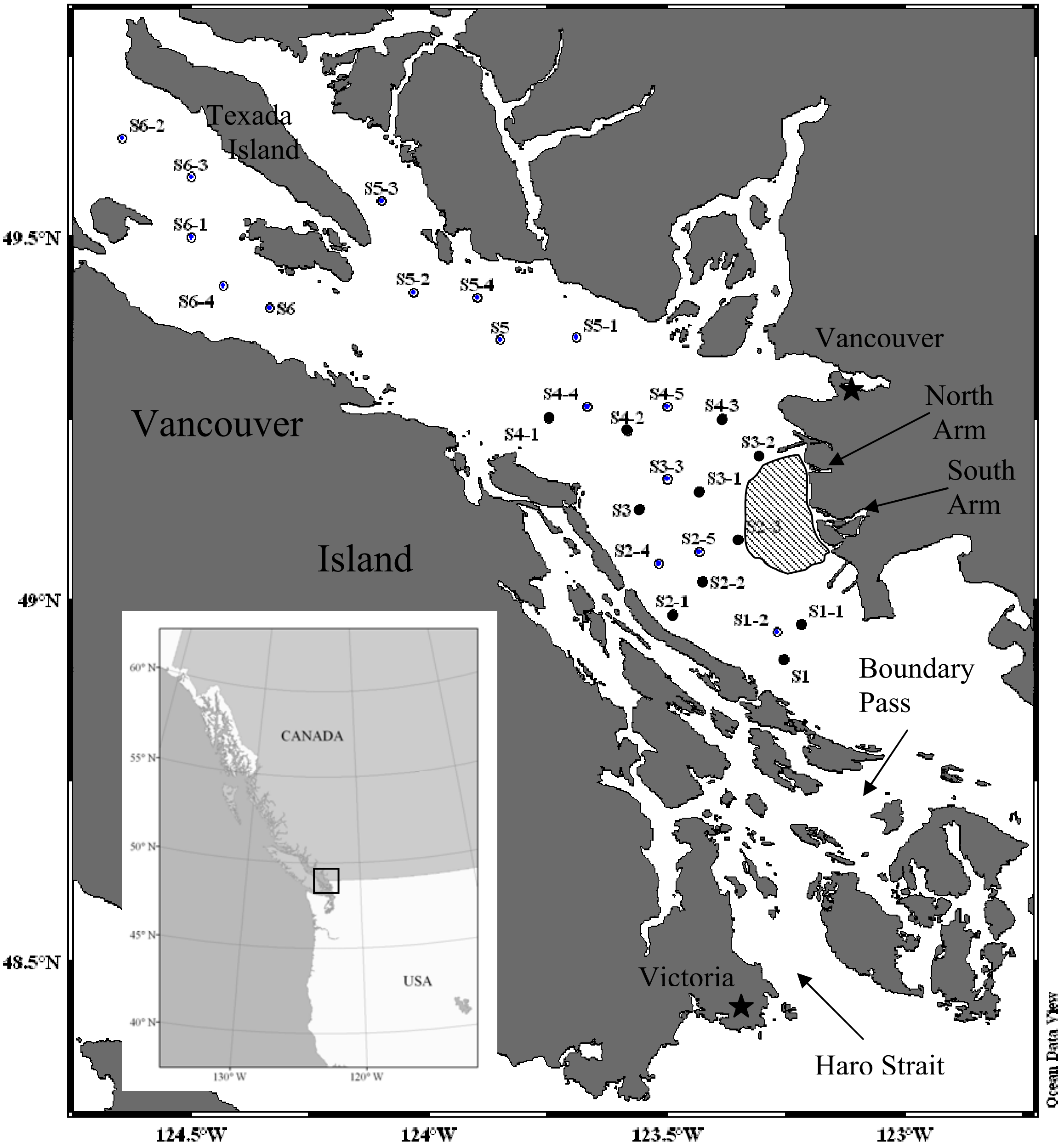

Figure 1 - Study area and sampling stations in the Strait of Georgia, BC, Canada. North and South Arms of the Fraser River are also indicated. Diagonal-filled area represents the mudflats at the mouth of the river. April stations are represented as black dots and July stations include all stations.

The SoG is a highly-productive, semi-enclosed coastal marine system important to fisheries and rearing of young salmon and herring (Stockner *et al.*, 1979; Li *et al.*, 2000). Primary productivity is limited by nutrients and grazing in the spring and summer, and by light in the winter (Takahashi *et al.*, 1973; Stockner *et al.*, 1979). A series of short phytoplankton blooms usually occurs in the spring, driven by a combination of factors, such as entrainment of inflowing nutrient-rich deep seawater into the surface layer (Thomson, 1981; Harrison *et al.*, 1991), tidal currents, winds (Yin *et al.*, 1996; Yin *et al.*, 1997a; Yin *et al.*, 1997b), and light availability (Allen & Harris, 2004; Collins, 2005). These blooms often continue into the summer months and occasionally occur in the fall or winter. Recent studies have shown that wind plays the most important role on the variance of the timing of the spring bloom, i.e. water stratification is disrupted by high winds, delaying the development of the phytoplankton blooms. Among the variables controlling the time of the spring bloom, light availability was considered the most important (Collins, 2005).

The phytoplankton species assemblage is dominated by diatoms, particularly during blooms and around the Fraser River plume (Harrison *et al.*, 1983; Hobson & McQuoid, 1997) with *Skeletonema spp.* and *Thalassiosira spp.* being the most common groups throughout the year and during the spring blooms, respectively. Flagellates are found in smaller numbers but sometimes dominate in the winter. In general, diatoms dominate over other phytoplankton groups in the spring and summer around areas influenced by the Fraser River plume (Harrison *et al.*, 1983).

The SoG has not been the subject of many optical studies, except for a brief mention of extinction coefficient by Stockner *et al.* (1979) and Harrison *et al.* (1983), and the recent works by Johannessen *et al.* (2006), who used beam attenuation coefficient at 660 nm as a proxy for the distribution of suspended particles; and Masson & Peña (2009), who used the same transmissometer data together with measurements of $PAR(z)$ to estimate the depth of the euphotic zone and phytoplankton self-shading.

There are no absorption data available for the waters of the SoG from which to assess the contribution of CDOM to light attenuation. However, CDOM is a component of the total dissolved organic matter (DOM) pool (Coble, 2007), and dissolved organic carbon (DOC) has been estimated to comprise more than 80% of the total organic carbon in the SoG (Johannessen *et al.*, 2003), implying that CDOM may well have a significant effect on the underwater light climate of the Strait.

1.5 Dissertation Overview

This thesis encompasses a large collection of datasets. For clarity, Chapter 2 describes the methodology utilised in the acquisition and processing of hydrographic, biogeophysical, and optical data, and radiative transfer modelling. Chapter 3 examines the results for each dataset and the determination of water masses according to their optical properties.

Chapter 4 provides an explanation of the results and discusses their connectedness. And finally, Chapter 5 provides a summary of all findings.

Chapter 2: Methodology

2.1 Discrete Water Samples - Acquisition and Processing

A total of 38 stations was sampled during April 25-29 (11 stations) and July 12-18 2006 (27 stations) onboard the MSV John Strickland (Figure 1). (Sampling did not take place during the peak discharge at the end of May for logistical reasons.) The sampling stations were positioned (1) to capture the optical variability of the waters of the SoG, from northern waters, close to Texada Island, to central waters under stronger influence of the Fraser River plume, and (2) to coincide with sampling locations used by Pawlowicz *et al.* (2004), Collins (2005), and Johannessen *et al.* (2006) for the purpose of future comparisons with on-going research in the region. The influence of daily oscillations of tides, currents, winds, and river discharge precluded synoptic sampling. However, these are the first such data for the region. For each station, water samples were collected from at least three depths: subsurface (0.5 m), at the chlorophyll *a* (chl *a*) maximum (2-8 m in April and 0-9 m in July, as indicated by a WET Labs profiling fluorometer), and just below the depth of 1% surface irradiance, $Z_{1\%}$, (4-20 m in April and 3-22 m in July). $Z_{1\%}$ was defined based on real-time measurements of in-water spectral downwelling irradiance, $E_d(0\text{-},z,PAR)$, and above-water spectral downwelling irradiance, $E_s(0+,PAR)$, collected with Satlantic Minispec OCR-3000 sensors on a vertical profiler and above water. The water samples were collected with 5 L Niskin bottles and stored in the dark at 4°C for a maximum of nine hours before filtration for chl *a*, TSM, and CDOM analysis.

For TSM analysis, the water samples were filtered (volumes ranging from 1 L to 3 L) through pre-combusted and pre-weighed 0.7 μm Whatman GF/F filters. After filtration, the filters were dried at 60°C for 6 hours until they reached a constant weight. The mass of total suspended material was calculated as the difference between the final and initial masses of the filters (Clesceri *et al.*, 1998). Finally, the weights of filter blanks were also subtracted from the total TSM weight. For chl *a*, water samples (volumes ranging from 1 L to 3 L) were filtered through 0.7 μm Whatman GF/F filters and stored folded in Falcon tubes. The tubes were kept frozen at -80°C until the pigments were extracted and their concentrations determined by reverse-phase high-performance liquid chromatography (HPLC) (Arar, 1997) (see Appendix A).

Samples (volume of 1 L) were also filtered for CDOM using a 0.2 μm Pall Supor® membrane disc filter and stored frozen at -30°C in 60-mL amber bottles that had been previously rinsed with deionised water, DI, and pre-combusted at 450°C for 1 h. These samples were then thawed and analysed using an Ocean Optics S2000 single-beam spectrophotometer. A 10-cm quartz cuvette was used to measure the absorbance, $A(\lambda)$, of CDOM between 250 and 875 nm, as suggested by Chen & Gardner (2004) and Kowalczuk *et al.* (2005). Absorbance measurements were baseline-corrected by subtracting the mean $A(\lambda)$ between 650 and 875 nm due to the negligible absorption of CDOM in that interval. These values were then converted to $a_{CDOM}(\lambda)$ values by rearranging Beer-Lambert's Law into

$$a_{CDOM}(\lambda) = 2.303\frac{A(\lambda)}{l}, \tag{25}$$

where *l* was the cuvette length in metres. DI was used as the reference standard.

The slope *S(λ)* was calculated according to Blough & Del Vecchio (2002):

$$S(\lambda) = \frac{Ln\left[\frac{a_{CDOM}(411)}{a_{CDOM}(\lambda)}\right]}{\lambda - 411} \text{ (nm}^{-1}\text{)} \tag{26}$$

CDOM absorption spectra were then fitted to an exponential function as

$$a_{Cspec}(\lambda) = \frac{a_{CDOM}(411)}{e^{\bar{S}(\lambda - 411)}} \text{ (m}^{-1}\text{)} \tag{27}$$

where $\bar{S}(\lambda)$ was the mean of *S(λ)* from 415 to 500 nm, where in general sampling noise was low.

2.2 Inherent Optical Properties - Acquisition and Processing

Total beam attenuation, total absorption, and CDOM absorption coefficients were measured *in situ* with a WET Labs ac-S instrument. Salinity, temperature and depth were measured simultaneously using a SeaBird CTD (conductivity-temperature-depth profiler). Water samples were collected at specific depths (Section **2.1**) following the instrumental profiles. All instruments were integrated in the same cage and measurements were time-stamped to facilitate the manipulation of data sets. The measured total beam attenuation coefficient, $c_T(z,\lambda)$, is the sum of the total absorption coefficient, $a_T(z,\lambda)$, and total scattering coefficient, $b_T(z,\lambda)$ (Equations 28 to 28.3). In turn, the measured total absorption coefficient, $a_T(z,\lambda)$, is the sum of the component absorption coefficients: water, $a_w(z,\lambda)$, particulate material, $a_p(z,\lambda)$, and CDOM, $a_C(z,\lambda)$, (Equation 29). The particulate absorption coefficient $a_p(z,\lambda)$ can be further decomposed into phytoplankton absorption coefficient $a_{phy}(z,\lambda)$ and mineral/inorganic absorption coefficient $a_{min}(z,\lambda)$ (Equation 30). Similarly, the total scattering coefficient $b_T(z,\lambda)$ is the sum of its component scattering coefficients of water, $b_w(z,\lambda)$, and particulate material, $b_p(z,\lambda)$, (Equation 31), which can be decomposed into phytoplankton, $b_{phy}(z,\lambda)$, and mineral/inorganic, $b_{min}(z,\lambda)$, scattering coefficients (Equation 32), with the general assumption that scattering due to CDOM is negligible (Mobley, 1994). The *in situ* absorption and attenuation by particles were not separated into phytoplankton and inorganic components.

$$c_T(z,\lambda) = c_w(z,\lambda) + c_p(z,\lambda) + c_C(z,\lambda) = a_T(z,\lambda) + b_T(z,\lambda) \tag{28}$$

$$c_w(z,\lambda) = a_w(z,\lambda) + b_w(z,\lambda) \tag{28.1}$$

$$c_p(z,\lambda) = a_p(z,\lambda) + b_p(z,\lambda) \tag{28.2}$$

$$c_C(z,\lambda) = a_C(z,\lambda) \tag{28.3}$$

where $c_w(z,\lambda)$, $c_p(z,\lambda)$, and $c_C(z,\lambda)$ are the attenuation coefficients of water, particulates, and CDOM, respectively.

$$a_T(z,\lambda) = a_w(z,\lambda) + a_p(z,\lambda) + a_C(z,\lambda), \tag{29}$$

where

$$a_p(z,\lambda) = a_{phy}(z,\lambda) + a_{min}(z,\lambda) \tag{30}$$

$$b_T(z,\lambda) = b_w(z,\lambda) + b_p(z,\lambda), \tag{31}$$

where

$$b_p(z,\lambda) = b_{phy}(z,\lambda) + b_{min}(z,\lambda) \tag{32}$$

The attenuation and absorption sensors each acquire data in 86 channels over the spectral range of 400-737 nm, with a spectral resolution of approximately 4 nm, at a frequency of 4 Hz. The pathlength of each sensor is 25 cm. The absorption and attenuation meters were factory-calibrated before the field sampling and during the cruise with DI to monitor any drifts in the measurements (Pegau *et al.*, 2003). The CDOM absorption coefficient was acquired by fitting a vented Pall mini-capsule 0.2 µm sterile filter on the absorption tube intake of the ac-S (Twardowski *et al.*, 1999). The capsule had been previously flushed with 1 L of DI to rinse out any impurities on the filter membranes (Ian Walsh, WET Labs, personal communication). CDOM fluorescence ($f_C(z)$) was measured with a fluorometer (WET Labs, Inc.). The CDOM fluorometer excitation and emission wavelengths were 370 nm and 460 nm, respectively, with a sensitivity of 0.25 ppb of Quinine Sulphate Dihydrate Equivalent (QSDE).

A series of processing steps was applied to the measured coefficients: 1) The optical data were extracted from the ac-S with software provided by WET Labs, Inc., using the original factory calibration files. Pure water attenuation, $c_w(z,\lambda)$, and absorption, $a_w(z,\lambda)$, were subtracted from $c_T(z,\lambda)$, $a_T(z,\lambda)$, and $a_C(z,\lambda)$, using the coefficients from Pope & Fry (1997), yielding $c_t(z,\lambda)$, $a_t(z,\lambda)$, and $a_c(z,\lambda)$, respectively (WET Labs, 2008). Each final file contained either a descending or ascending vertical profile of $c_t(z,\lambda)$, $a_t(z,\lambda)$, $a_c(z,\lambda)$, temperature, salinity, depth, and CDOM concentration ($f_C(z)$ converted to QSDE). In order to minimise the effect of bubbles in the ac-S sensors and thus noise in the data, only upcast measurements were analysed; 2) The data were binned to 1-m intervals, followed by DI calibration and temperature and salinity corrections (Sullivan *et al.*, 2006; WET Labs, 2008); 3) Scattering-corrected absorption coefficients, $a_{t'}(z,\lambda)$ and $a_{c'}(z,\lambda)$, were obtained through Equations 33 and 34 by using $c_t(z,717)$, $a_t(z,716)$, and $a_C(z,716)$; this correction minimises the unwanted scattered light in the absorption meter (Zaneveld *et al.*, 1994). For consistency of notation, $c_t(z,\lambda)$ will be presented as $c_{t'}(z,\lambda)$ hereafter. Beam scattering, $b_{t'}(z,\lambda)$, was obtained directly through the subtraction of $a_{t'}(z,\lambda)$ from $c_{t'}(z,\lambda)$ (Equation 35). Furthermore, the particulate absorption coefficient, $a_{p'}(z,\lambda)$, was obtained from the subtraction of $a_{c'}(z,\lambda)$ from $a_{t'}(z,\lambda)$ (Equation 36).

Scattering correction for $a_t(z,\lambda)$ (Zaneveld *et al.*, 1994):

$$a_{t'}(z,\lambda) = a_t(z,\lambda) - \frac{a_t(z,716)}{c_t(z,717) - a_t(z,716)}\left(c_t(z,\lambda) - a_t(z,\lambda)\right) \tag{33}$$

Scattering correction for $a_c(z,\lambda)$:

$$a_{c'}(z,\lambda) = a_C(z,\lambda) - a_C(z,716) \tag{34}$$

$$b_{t'}(z,\lambda) = c_{t'}(z,\lambda) - a_{t'}(z,\lambda) = b_{p'}(z,\lambda) \tag{35}$$

$$a_{p'}(z,\lambda) = a_{t'}(z,\lambda) - a_{c'}(z,\lambda) \tag{36}$$

2.3 Radiometric Quantities and Apparent Optical Properties - Acquisition and Processing

In-water spectral downwelling irradiance, $E_d(0\text{-},z,\lambda)$, and in-water spectral upwelling radiance, $L_u(0\text{-},z,\lambda)$, were collected with Satlantic Minispec OCR-3000 sensors (calibrated spectral range of 400-800 nm) installed on a free-falling profiler. Above-water spectral downwelling irradiance, $E_s(0+,\lambda)$, was collected using a Satlantic Minispec OCR-3000 installed at the top of a 6-m pole on the upper deck of the MSV Strickland in order to avoid shadowing. Irradiance and radiance duplicates were averaged, then underwater radiance reflectance, $R_r(0\text{-}z,\lambda)$, was computed using equation 37 from surface to $Z_{1\%}$. Satlantic's ProSoft software was used to process and bin the data to 1-m depth intervals as well as for calculating the AOP: diffuse attenuation coefficients for spectral downwelling irradiance, $K_{Ed}(z,\lambda)$, (Equation 38) and for spectral upwelling radiance, $K_{Lu}(z,\lambda)$, (Equation 39).

$$R_r(0-,z,\lambda) = \frac{L_u(0-,z,\lambda)}{E_d(0-,z,\lambda)} \ (\mathrm{sr}^{-1}) \tag{37}$$

$$K_{Ed}(z,\lambda) = -\frac{1}{E_d(0-,z,\lambda)}\frac{dE_d(0-,z,\lambda)}{dz} \ (\mathrm{m}^{-1}) \tag{38}$$

$$K_{Lu}(z,\lambda) = -\frac{1}{L_u(0-,z,\lambda)}\frac{dL_u(0-,z,\lambda)}{dz} \ (\mathrm{m}^{-1}) \tag{39}$$

2.4 Radiative Transfer Modelling

Numerical modelling of the optical properties of the waters of the SoG was performed with Hydrolight 4.3 (Sequoia Scientific, Inc.) (Mobley, 1994) to obtain certain IOPs and AOPs that had not been acquired *in situ*. Hydrolight carries out radiative transfer calculations through invariant imbedding techniques that require IOP and environmental conditions as input. The entire set of field data was entered into Hydrolight's model

ABACBB to solve the radiative transfer equations and calculate backscattering and absorption components as well as some radiometric quantities and average cosines. The input dataset consisted of IOPs ($c_{t'}(z,\lambda)$, $a_{t'}(z,\lambda)$, $a_{c'}(z,\lambda)$, all within the spectral range of 400-700 nm), pure water absorption values from Pope & Fry (1997), chl *a* concentrations obtained from HPLC measurements, wind speeds, cloud cover, air pressure, downwelling irradiance, $E_s(0+,\lambda)$, and date and time of field sampling. The ABACBB model separated the optical constituents into pure water, particulate matter (detritus and phytoplankton), and CDOM. To ensure that Hydrolight output would closely match *in situ* data, it was necessary to input backscattering ratios, $b_b(z,\lambda)/b_t(z,\lambda)$. However, since those had not been collected *in situ*, they were chosen from the Hydrolight library and input as Fournier-Forand (FF) scattering phase functions (Bergmann *et al.*, 2004). FF values were optimized for each station (values ranging from 0.004 to 0.028) by examining the closure between *in situ* and modelled $R_r(0\text{-}z,\lambda)$. All simulations were performed to the bottom of $Z_{1\%}$ as defined in section **2.1**. Modelled IOPs and AOPs were then compared with *in situ* measured data to assess the performance of the simulation.

Chlorophyll absorption, $a_{chl}(z,\lambda)$, is calculated in Hydrolight according to Morel (1991) and given by

$$a_{chl}(z,\lambda) = \left[a_w(\lambda) + 0.06\, a^*_{chl}(z,\lambda)\, C^{0.65}\right]\left[1 + 0.2\, e^{[0.014(\lambda-440)]}\right] \qquad (40)$$

where $a^{*}_{chl}(z,\lambda)$ is the statistically-derived chlorophyll-specific absorption coefficient and C is chlorophyll concentration. Consequently, $a_{chl}(z,\lambda)$ can be substituted for $a_{phy}(z,\lambda)$ in equation 30.

Chapter 3: Results

3.1 Hydrographic and Biophysical Data

The mean discharge of the Fraser River at the time of data acquisition in late April was 2578 m^3s^{-1}, thus representing more than twice the pre-freshet discharge of around 645 m^3s^{-1} (Environment Canada, 2006); in July, the mean discharge was 3933 m^3s^{-1} (Environment Canada, 2006) (Figure 2). The high discharge throughout our sampling period resulted in a hydrographically-distinct plume of warm, brackish water (salinity and temperature means of 20.4 and 10.4°C, respectively, in April, and 12.1 and 16.6°C in July), typical of spring and summer conditions (Tully & Dodimead, 1957; Waldichuk, 1957) (Figure 3). Both the halocline and the thermocline were well defined, but their strength decreased with increasing distance from the river mouth. In general, the water column became less stratified with distance, with vertical salinity and temperature ranges of 25.6-29.0 and 8.7-10.7°C, respectively, in April, and 8.5-29.4 and 10.1-17.2°C in July within $Z_{1\%}$.

The measured concentrations of chl *a*, CDOM and TSM were closely related to the hydrographic variability. For instance, TSM and CDOM concentrations showed significant inverse relationships with salinity (Figure 4). The low salinity waters closest to the Fraser River mouth (stations S1-1, S2-3, S3-2, and S4-3) (Figure 1) carried large amounts of sediments in the spring, reaching values of 11.8 mg L^{-1} at surface (S3-2) and increasing to 13.4 mg L^{-1} (S2-3 at 15 m) below $Z_{1\%}$ (4 m) in April; in July, when $Z_{1\%}$ was at 2 m, TSM concentrations were relatively higher at 15.1 mg L^{-1} at surface (S3-2) and 18.2 mg L^{-1} at 3 m (S2-3). High TSM concentrations were also found in southern waters (S1 and S1-1). Overall, CDOM concentrations ranged from 5.6-32.1 ppb QSDE and from 6.0-15.7 ppb QSDE in April and July, respectively. Chl *a* was inversely related to salinity, but only statistically significant in July (Figure 4). In lower salinity waters, chl *a* concentrations were lower in July than in April, and in general, chl *a* maxima occurred below the plume. Concentrations of chl *a* varied greatly between April and July, with a maximum of 11.3 μg L^{-1} occurring between salinities of 26.0 and 28.0 in April, and 9.3 μg L^{-1} between salinities of 20.0 and 22.0 in July.

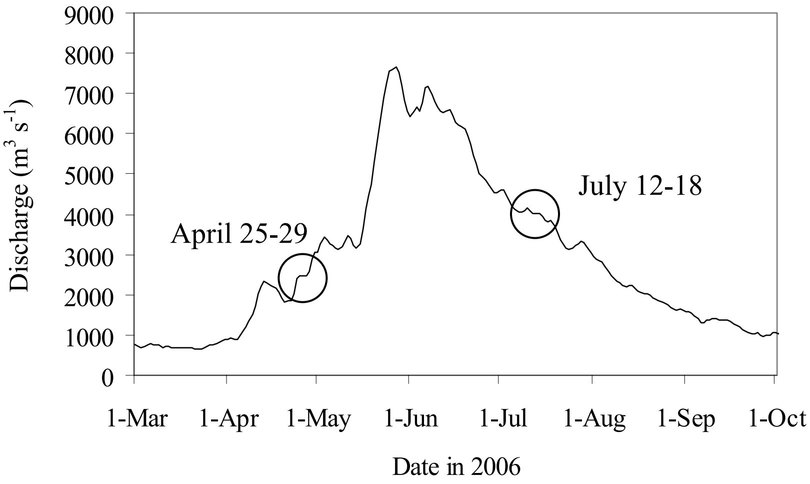

Figure 2 - Fraser River discharge in 2006 (Environment Canada, 2006). Circles indicate discharge during data acquisition.

The stations located in the western and northern regions of the SoG (S1, S2-1, S3, S4-1, S6 stations, and S5 stations) displayed generally lower concentrations of the same biophysical properties (OM3 in Table 1). For these waters, $Z_{1\%}$ occurred at about 20 m in April and 22 m in July, when TSM and CDOM values were relatively lower.

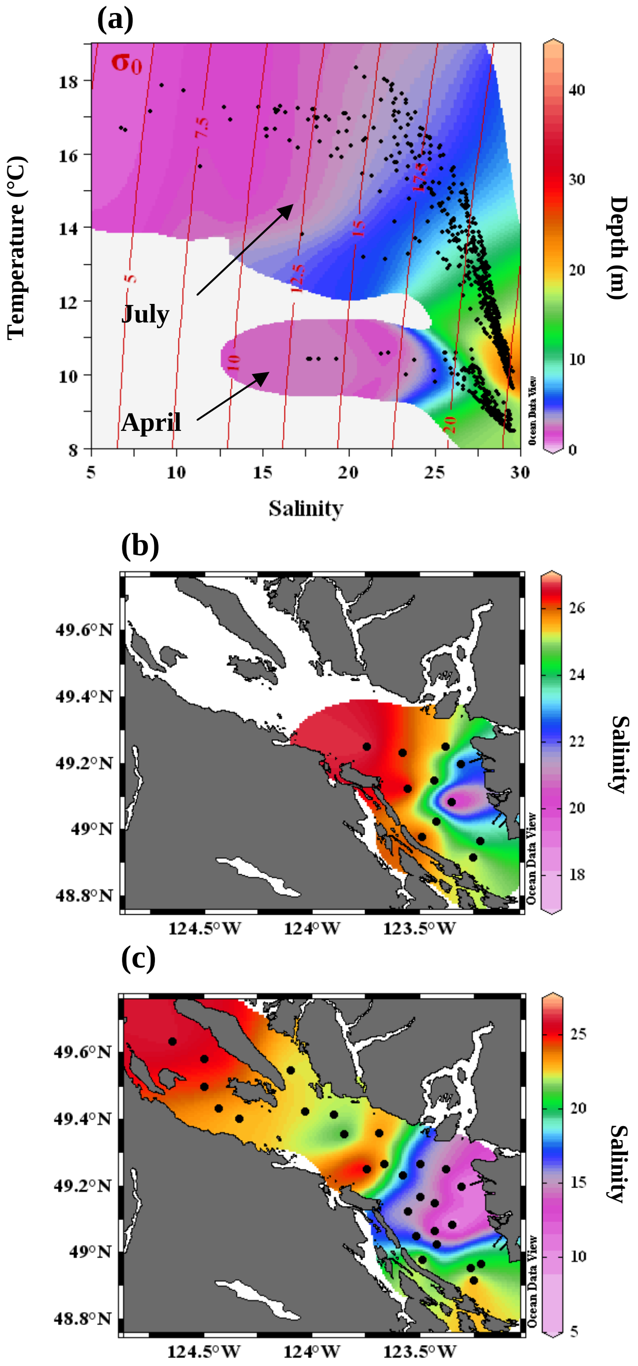

Figure 3 - (a) Temperature-salinity plot of all stations in April and July. Depth is displayed in colour and isopycnals are displayed in red. Surface plots of salinity in (b) April and (c) July show the westward migration of the Fraser River plume.

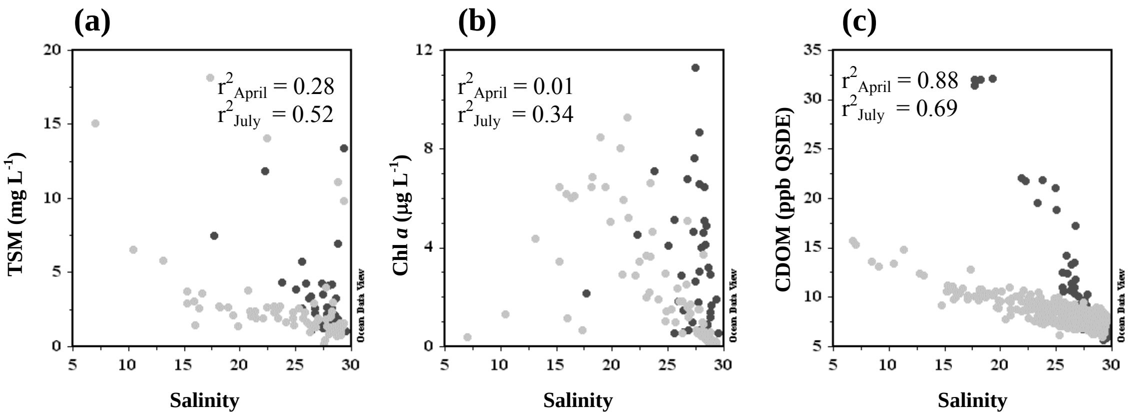

Figure 4 - (a) TSM, (b) chl a, and (c) CDOM versus salinity in April (dark dots) and July (light dots).

Table 1 - Biophysical characteristics of three optical water masses observed in the Strait of Georgia, British Columbia, Canada, in April and July 2006 (Ranges, and mean ± 1 S.D.).

	April					
Water Mass	Salinity	Temperature (°C)	Depth (m)	CDOM (ppb QSDE)	chl *a* (µg L^{-1})	TSM (mg L^{-1})
OM1	17.7-26.7	9.6-10.6	0.0-5.5	24.7 ± 6.8	4.5 ± 2.0	6.9 ± 3.7
OM2	25.6-29.3	8.7-10.5	0.0-23.5	8.4 ± 1.8	4.2 ± 2.6	3.0 ± 1.2
OM3	25.6-29.6	8.5-10.7	1.0-25.2	7.4 ± 0.9	2.4 ± 2.5	2.6 ± 2.8

	July					
Water Mass	Salinity	Temperature (°C)	Depth (m)	CDOM (ppb QSDE)	chl *a* (µg L^{-1})	TSM (mg L^{-1})
OM1	6.8-23.4	13.1-17.8	0.0-6.6	12.6 ± 1.8	2.6 ± 2.6	9.9 ± 6.3
OM2	14.7-28.8	11.0-18.1	0.0-23.6	10.4 ± 0.3	3.8 ± 2.4	2.6 ± 2.0
OM3	24.1-29.5	9.6-15.9	2.6-41.5	7.7 ± 0.6	0.6 ± 0.7	1.9 ± 2.3

3.2 Hyperspectral Analysis

Given the observed, *almost* wavelength-independent behaviour of some of the measured IOPs (Section **3.2.1**) and for ease of reporting and discussing the results in the following sections, the analysis of the optical variables is presented for only three wavelengths (411, 530, and 650 nm) of the 86 sampled. These specific wavelengths characterize well the interactions among light, particles, and dissolved matter, and are close to wavelengths used by other authors (Bricaud *et al.*, 1981; Mobley, 1994; Kowalczuk *et al.*, 2003; Kowalczuk *et al.*, 2005) and by authors who used similar sensors to the ones used here (Twardowski & Donaghay, 2001; Oliver *et al.*, 2004; Chang *et al.*, 2006). Attenuation by TSM is almost constant throughout the visible spectrum (Mobley, 1995), and a red wavelength at around 650-660 nm is often used to characterise TSM (Carder *et al.*, 1993; Binding *et al.*, 2003; Chang *et al.*, 2006; Johannessen *et al.*, 2006). In addition to the three wavelengths mentioned above, absorption and scattering at 675 nm were also analyzed for application to chl *a* absorption (Sathyendranath *et al.*, 1987; Cleveland, 1995).

After defining the IOPs at the four different wavelengths, a clustering algorithm (Zhang *et al.*, 1997) was used to differentiate the water masses according to their optical properties in April and July. Preliminary data analysis showed that the optical beam attenuations at 411 and 650 nm ($c_{t'}(z,411,650)$), and absorption-to-scattering ratios at 411 and 530 nm ($a_{t'}(z,411)/b_{p'}(z,411)$, $a_{t'}(z,411)/b_{p'}(z,530)$) at each station were the IOPs most representative of the optical changes within the water masses of the SoG. Consequently, these IOPs and IOP ratios were used to define the optical water masses (OM) clusters.

3.2.1 Inherent Optical Properties - Definition and Characteristics of the Optical Water Masses

As shown in section **3.1**, the biophysical constituents, which define the spectral magnitude of the IOPs, were closely related to the hydrographic data, particularly salinity. Total attenuation, for example, was inversely correlated with salinity (Figure 5) and decreased in magnitude as plume waters mixed with SoG waters. Attenuation also decreased with increasing depth and increasing distance from the river mouth. Specifically, for waters closer to the river mouth (Figures 6a and 7a), total beam attenuation, $c_{t'}(z,\lambda)$, was at least one order of magnitude higher than for northern and deep waters (Figures 6c and 7c).

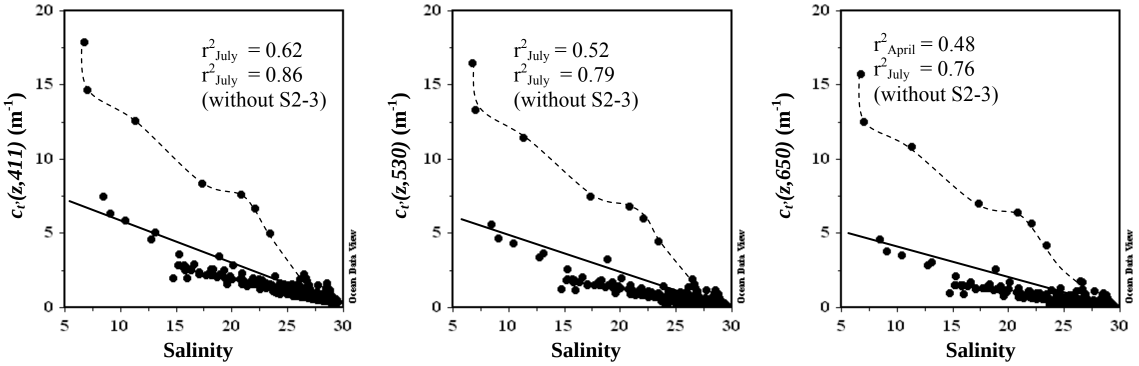

Figure 5 - Negative relationships between $c_{t'}(z,411,530,650)$ and salinity in July. Dashed line represents station S2-3.

Total attenuation was constant through the red wavelengths and increased slightly towards the blue wavelengths (Figure 6). This higher attenuation at short wavelengths was due mostly to absorption, rather than scattering. However, the general magnitude of $c_{t'}(z,\lambda)$ at all wavelengths was determined primarily by the magnitude of particulate scattering, except in deeper waters and in waters far from the influence of the Fraser River plume (Figure 7c), where absorption was also important. Total absorption was generally higher towards the blue wavelengths as a result of the absorption by CDOM and particles. CDOM absorption dominated $a_{t'}(z,\lambda)$ towards the blue end of the spectrum in deep waters close to the Fraser River mouth (Figure 6c), as well as below the plume and in deep waters away from the river mouth (Figures 7b and 7c, respectively). The chl *a* absorption peak at 675 nm was visible in waters away from the river plume (Figure 7), although it was not visible close to the Fraser River mouth (Figure 6), probably because of the strong scattering and absorption by inorganic particles in the plume.

The measured IOPs were used in a cluster analysis to classify water masses of the upper SoG (euphotic zone) according to their optical similarities. From this analysis, three optical water masses (OM1, OM2, and OM3) were defined. As the cluster descriptives show (Table 2), cluster centroids decreased in magnitude from OM1 to OM3 for both $c_{t'}(z,411)$ and $c_{t'}(z,650)$. The opposite occurred with the IOP ratios used in the cluster analysis, thus indicating the increasing dominance of $a_{t'}(z,411)$ over $b_{p'}(z,411)$ and $b_{p'}(z,530)$.

OM1, defined as the low salinity riverine plume waters, was characterized by the highest attenuation at 411 nm (14.8 m^{-1} in April and 17.9 m^{-1}in July). It was always located close to the river mouth, above the optical attenuation cline, *c-cline*, and never deeper than 5.5 m in April and 6.6 m in July (Figure 8). Generally, concentrations of chl *a* around 4.5 µg L^{-1} and 2.6 µg L^{-1} were found in OM1 in April and July, respectively, where the ratio $a_{t'}(z,411)/b_{p'}(z,530)$ ranged from 0.2 to 0.6 in April and from 0.1 to 0.4 in July, and where $c_{t'}(z,650)$ ranged from 2.91 to 11.85 m^{-1} in April and 3.55 to 15.75 m^{-1} in July. The highest attenuation values were always found at station S2-3 caused by the higher discharge of the river at the South Arm and its associated high TSM concentrations (18.2 mg L^{-1}).

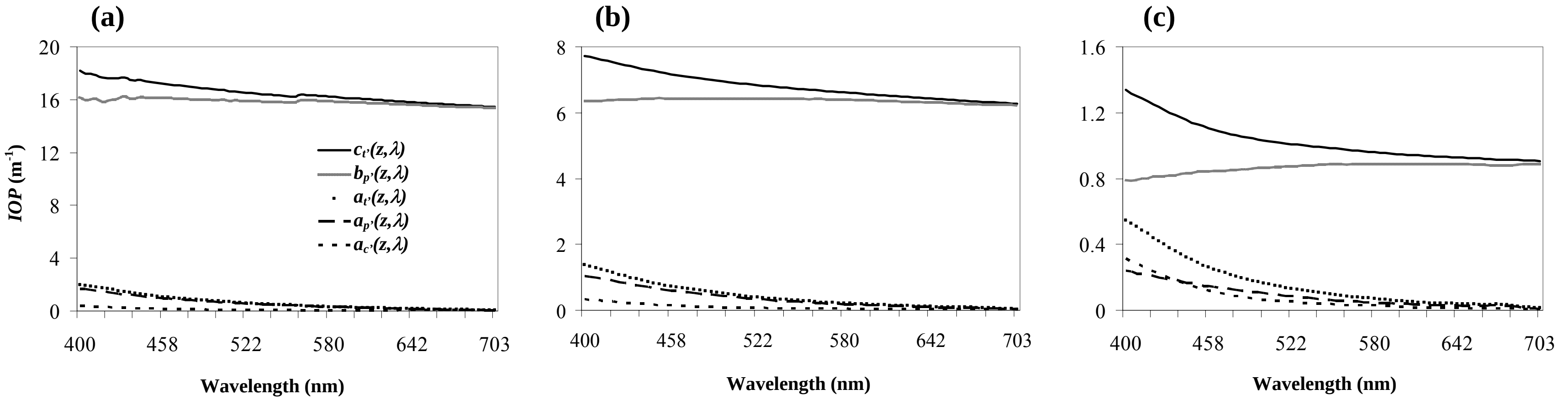

Figure 6 - Hyperspectral IOPs in (a) OM1, (b) OM2, and (c) OM3 at station S2-3 in July. Note the different magnitudes for the IOP-axis.

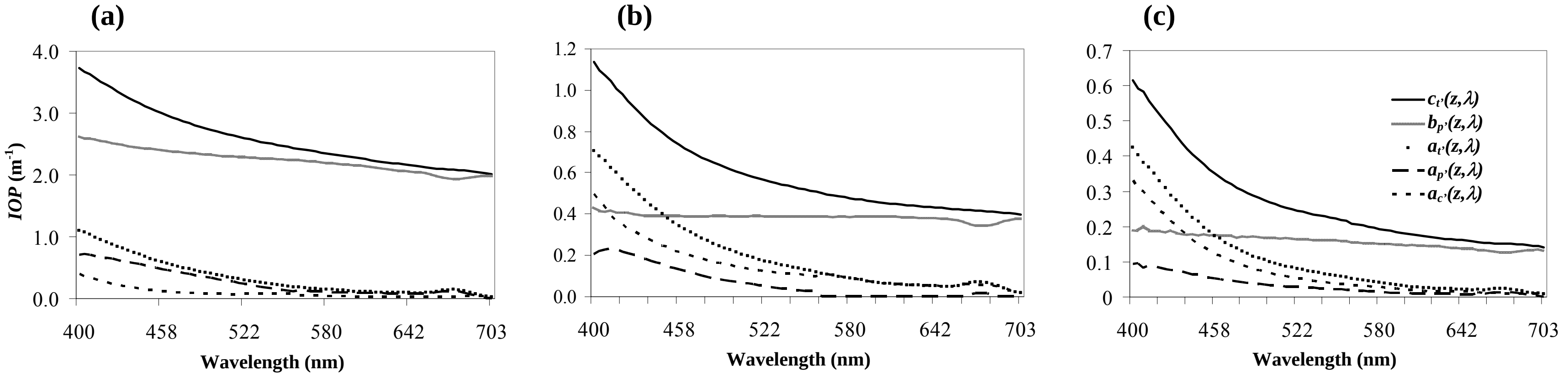

Figure 7 - Hyperspectral IOPs in (a) OM1, (b) OM2, and (c) OM3 at station S3 in July. Note the different magnitudes for the IOP-axis.

Table 2 - Cluster centroids (mean ± 1 S.D.) of the three optical water masses.

April	$c_{t'}(z,411)$ (m^{-1})	$c_{t'}(z,650)$ (m^{-1})	$a_{t'}(z,411)/b_{p'}(z,411)$	$a_{t'}(z,411)/b_{p'}(z,530)$
OM1 Riverine Plume	7.45 ± 3.68	5.14 ± 3.13	0.38 ± 0.13	0.40 ± 0.13
OM2 Estuarine Plume	1.26 ± 0.49	0.74 ± 0.33	0.77 ± 0.20	0.72 ± 0.16
OM3 Below Plume	0.65 ± 0.14	0.26 ± 0.09	1.46 ± 0.28	1.43 ± 0.28

July	$c_{t'}(z,411)$ (m^{-1})	$c_{t'}(z,650)$ (m^{-1})	$a_{t'}(z,411)/b_{p'}(z,411)$	$a_{t'}(z,411)/b_{p'}(z,530)$
OM1 Riverine Plume	7.79 ± 4.31	6.07 ± 4.15	0.24 ± 0.09	0.25 ± 0.09
OM2 Estuarine Plume	1.12 ± 0.55	0.53 ± 0.36	1.11 ± 0.31	1.21 ± 0.36
OM3 Below Plume	0.49 ± 0.12	0.13 ± 0.04	2.27 ± 0.40	2.52 ± 0.42

As river water mixed with SoG waters, attenuation decreased. The transitional waters comprising the estuarine plume, which was usually found below the river plume (at the c-cline) and extending to the surface at other locations as the influence of the riverine plume decreased were defined as OM2 (Table 2). In OM2, relatively high chl *a* concentrations (~ 11.3 μg L^{-1}) were found where $c_{t'}(z,650)$ was below 5.0 m^{-1} and $a_{t'}(z,411)/b_{p'}(z,530)$ was lower than 2.0 m^{-1} (Figure 9).

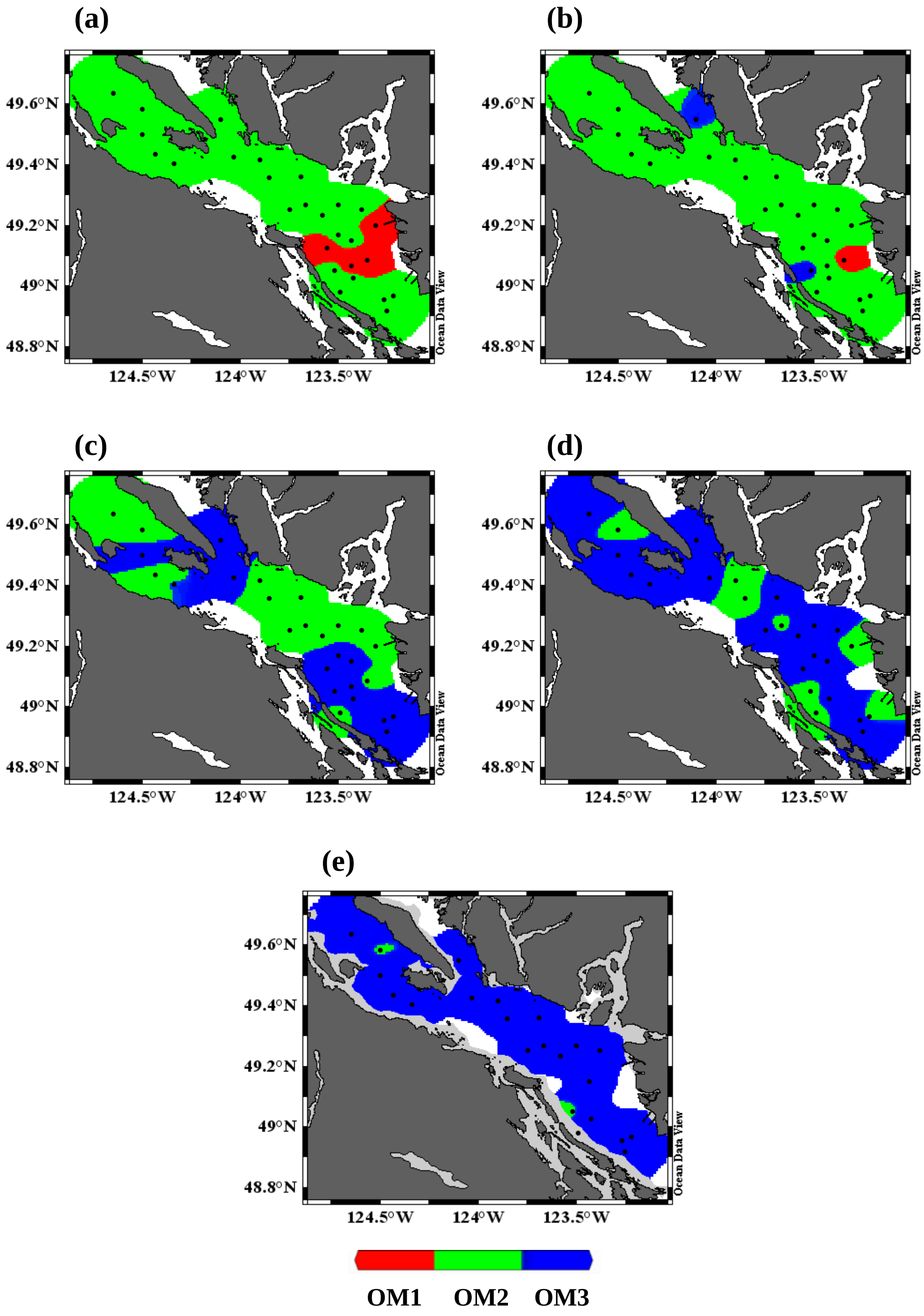

Figure 8 - Spatial distribution of the OMs at (a) surface, (b) 5m, (c) 10 m, (d) 15m, and (e) 20 m depth. Dots represent sampling stations in July.

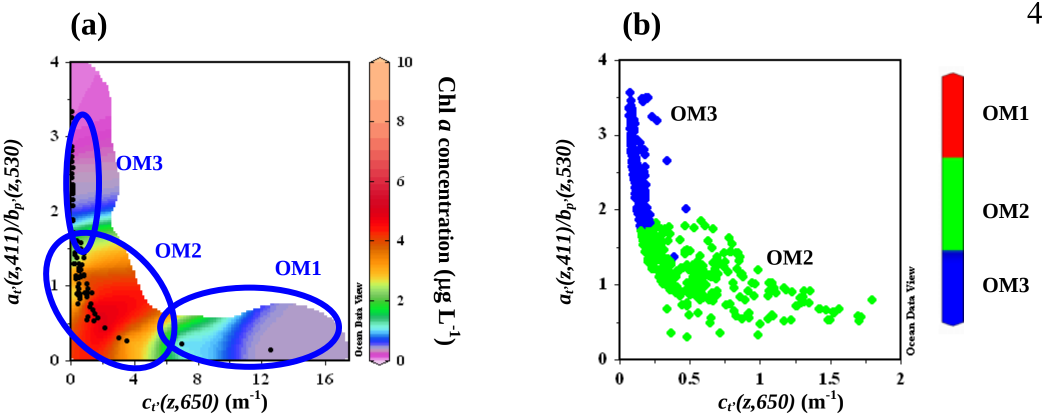

Figure 9 - Relationships between absorption-to-particulate scattering ratio $a_{t'}(z,411)/b_{p'}(z,530)$ and total attenuation at 650 nm $c_{t'}(z,650)$ in (a) April and (b) July for the three OM.

OM3 waters were characterized by higher salinity and occurred below the estuarine plume (below the c-cline) and in deeper waters (Figure 8), and showed the lowest variability in attenuation (Table 2). The concentration of chl *a* was low in these waters (mean of 0.7 µg L^{-1} and maximum of 3.0 µg L^{-1}), where $a_{t'}(z,411)$ was at least twice as high as $b_{p'}(z,530)$ (Figure 9). Increasingly high $a_{t'}(z,411)/b_{p'}(z,530)$ (1.03 to 2.55 in April and 1.37 to 3.56 in July) and very low $c_{t'}(z,650)$ values (0.14 to 0.52 m^{-1} in April and 0.07 to 0.48 m^{-1} in July) were seen in OM3 waters.

The characterisation of the optical water masses was also evident from the relationship between $a_{t'}(z,411)$ and $c_{t'}(z,650)$, which was linear up to an inflection point where $c_{t'}(z,650)$ was approximately 5.0 m^{-1} (Figure 10), indicating the strong contribution of absorption to the total attenuation in OM2 and OM3. Scattering contributed strongly to the total attenuation after the inflection point. The same pattern was observed in OM1.

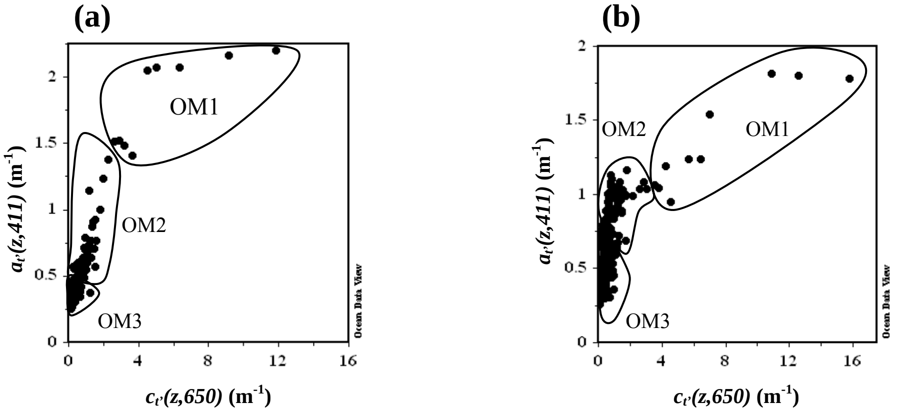

Figure 10 - Relationship between $a_{t'}(z,411)$ and $c_{t'}(z,650)$ in (a) April and (b) July. OM1 waters were under direct influence of the Fraser River. OM2 and OM3 waters were those waters below the inflection point that indicated the higher influence of particulate scattering on attenuation.

To characterise further the roles of *in situ* $a_{p'}(z,\lambda)$, $a_{c'}(z,\lambda)$, and $b_{p'}(z,\lambda)$ to $c_{t'}(z,\lambda)$ in each optical water mass, their average percentage contributions at three wavelengths were calculated (Figure 11). The results showed that, in each of the three water masses, the individual contributions varied in magnitude in both April and July, but generally followed the same pattern. In OM1, scattering by particles (including phytoplankton, detritus, and mineral sediments) dominated the total attenuation at 411 nm ($a_{p'} \approx 18\%$, $b_{p'} \approx 77\%$; values averaged for April and July cruises) and at 530 nm ($a_{p'} \approx 6\%$, $b_{p'} \approx 93\%$). At 650 nm, particulate scattering was responsible for most of the attenuation ($b_{p'} \approx 98\%$), and the small absorption component was due almost equally to CDOM and particles.

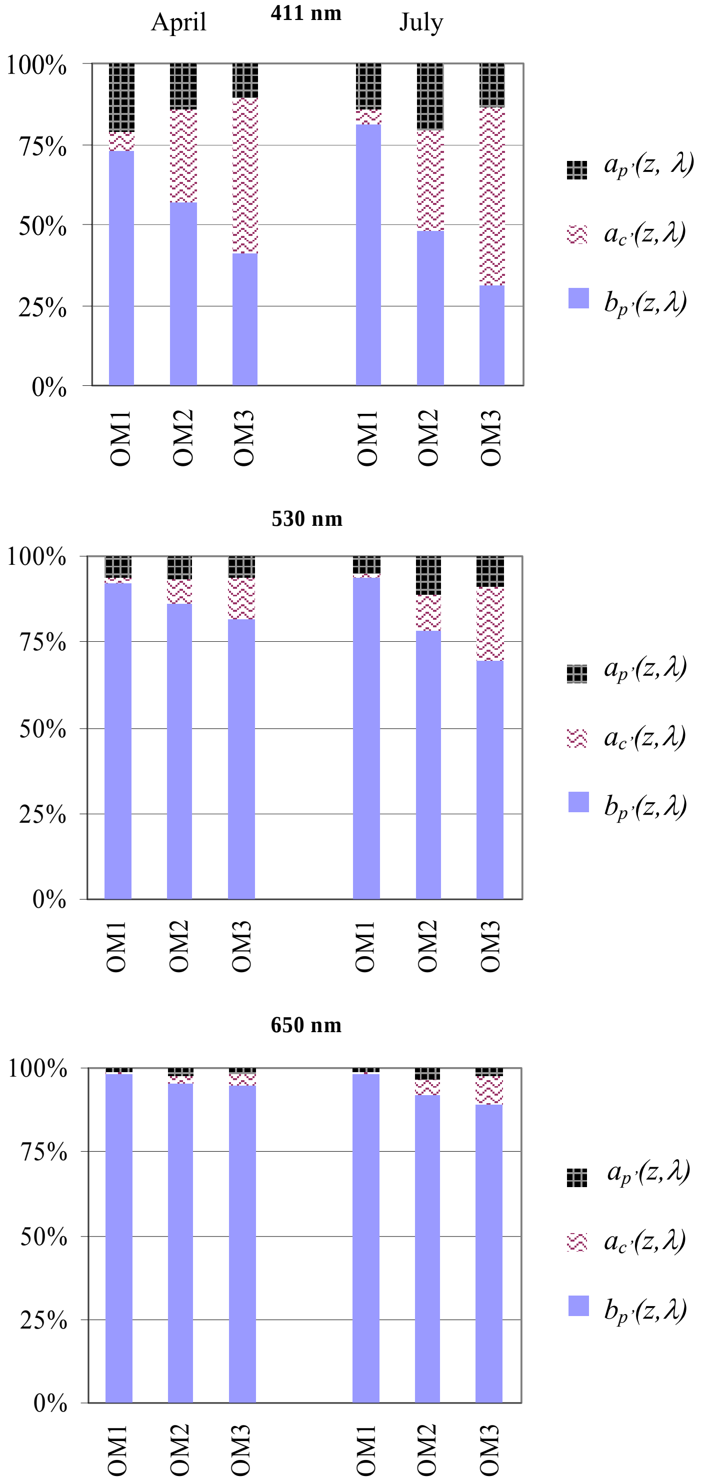

Figure 11 - Contribution of *in situ* particulate scattering, $b_{p'}(z, \lambda)$, CDOM absorption, $a_{c'}(z, \lambda)$, and particulate absorption, $a_{p'}(z, \lambda)$, coefficients to total beam attenuation coefficient, $c_{t'}(z,\lambda)$, at 411 nm, 530 nm, and 650 nm in April and July 2006.

In OM2, particulate scattering and absorption contributed strongly to the attenuation of light at 411 nm; however, CDOM absorbed more ($a_{c'} \approx 30\%$) than did the particles ($a_{p'} \approx 17\%$). In this water mass, particulate scattering dominated attenuation at 530 nm ($b_{p'} \approx 82\%$) while CDOM and particles contributed equally to the total absorption ($a_{p'} \approx a_{c'} \approx 9\%$). Similarly, at 650 nm, particles were responsible for most of the attenuation due to scattering ($b_{p'} \approx 94\%$); particles and CDOM contributed equally to absorption in April, but CDOM dominated in July ($a_{c'} \approx 5\%$).

Conversely, OM3 showed a distinct optical behaviour at 411 nm where absorption, particularly that of CDOM ($a_{c'} \approx 53\%$ of a_T) played a larger role in the total attenuation. At 530 nm and 650 nm, particles dominated attenuation due to scattering ($b_{p'}(z,530) \approx 76\%$; $b_{p'}(z,650) \approx 92\%$), as in OM1 and OM2, but absorption by CDOM exceeded absorption by particles ($a_{c'}(z,530) \approx 17\%$; $a_{c'}(z,650) \approx 6\%$).

The observed pattern of IOPs for each optical water mass was the result of the variability in the optical constituents in these waters. The relationships among IOPs and optical constituents were explored for each defined optical water mass. As expected, in OM1, $b_{p'}(z,650)$ had significant relationships with TSM ($r^2_{\mathrm{April}} = 0.62$; $r^2_{\mathrm{July}} = 0.63$). In OM2, TSM showed relative lower positive relationships with $b_{p'}(z,650)$ ($r^2_{\mathrm{April}} = 0.41$; $r^2_{\mathrm{July}} = 0.26$), and in OM3, the relationship between these variables in April was very low and not statistically significant (at 95% confidence level; $r^2_{\mathrm{April}} = 0.16$) but statistically significant in July (r^2_{July} = 0.23). These correlations accord with the decreasing influence of TSM on scattering from OM1 to OM3. Chl *a* and $a_{t'}(z,675)$ were significantly positively correlated in April, except in OM2 (r^2_{OM1} = 0.82, r^2_{OM3}=0.54); however in July, they were significantly correlated in all water masses but OM1 (r^2_{OM2} = 0.61, r^2_{OM3} = 0.52).

Contrary to expectations, the relationships between the measured *in situ* CDOM fluorescence and *in situ* $a_{c'}(z,411)$ were not statistically significant. It is possible that the weak relationships were due to the characteristics of the fluorometer used in this study; it was not capable of measuring autochthonous CDOM because the excitation and emission wavelengths utilized are only suitable for C-region fluorophores, which characterize terrigenous CDOM (Coble, 1996; Conmy *et al.*, 2004; Guéguen *et al.*, 2005). Apart from the limitations of the fluorometer, the observed lower correlation, specifically in April, may be a result of the quality of the CDOM absorption data, reflected in the fact that CDOM absorption did not vary significantly with depth (Table 3). The 0.2 µm filter used to collect $a_{c'}(z,\lambda)$ must be completely purged of air (Twardowski *et al.*, 1999; WET Labs, 2008), and this was not always the case in April. Nevertheless, the $a_{c'}(z,\lambda)$ data from April followed similar trend and magnitude of $a_{c'}(z,\lambda)$ data acquired in July, for which the acquisition method had been improved, thus suggesting that the CDOM absorption data were accurate.

Relationships between *in situ* and spectrophotometric CDOM absorption for all OMs were not statistically significant in April ($r^2_{April} = 0.08$); however, this was not the case in July ($r^2_{July} = 0.36$). Table 3 presents CDOM absorption statistics as well as the mean of $\overline{S}$ for each OM. Table 4 presents the relationship between CDOM fluorescence and CDOM absorption.

Table 3 - $a_{c'}(z,411)$, $a_{Cspec}(z,411)$, their r^2 and $\overline{S}$ for each OM (mean ± 1 S.D. and ranges).

	April				July			
	$a_{c'}(z,411)$ (m^{-1})	$a_{Cspec}(z,411)$ (m^{-1})	r^2	$\overline{S}$ (nm^{-1})	$a_{c'}(z,411)$ (m^{-1})	$a_{Cspec}(z,411)$ (m^{-1})	r^2	$\overline{S}$ (nm^{-1})
OM1	0.37 ± 0.15 0.21 - 0.64	1.01 ± 0.49 0.52 - 1.50	0.10	0.01650 ± 0.00111 0.01575-0.01777	0.30 ± 0.03 0.25 - 0.37	0.53 ± 0.06 0.44 - 0.60	0.31	0.01539 ± 0.00091 0.01438-0.01684
OM2	0.37 ± 0.21 0.18 - 1.54	0.37 ± 0.14 0.19 - 0.78	0.08	0.01798 ± 0.00356 0.01162-0.02767	0.31 ± 0.10 0.18 - 1.66	0.50 ± 0.15 0.22 - 0.76	0.25	0.01499 ± 0.00220 0.00798-0.01851
OM3	0.34 ± 0.15 0.10 - 1.28	0.35 ± 0.08 0.21 - 0.47	0.05	0.01716 ± 0.00352 0.01172-0.02547	0.28 ± 0.10 0.18 - 1.58	0.27 ± 0.07 0.15 - 0.44	0.28	0.01670 ± 0.00334 0.00953-0.02186

Table 4 - Relationships between CDOM fluorescence and *in situ* and laboratory CDOM absorptions.

r^2	April		July	
	$f_C(z)$ x $a_{c'}(411)$	$f_C(z)$ x $a_{Cspec}(411)$	$f_C(z)$ x $a_{c'}(411)$	$f_C(z)$ x $a_{Cspec}(411)$
OM1	0.30	0.77	0.05	0.14
OM2	0.25	0.72	0.10	0.38
OM3	0.05	0.49	0.05	0.16

3.2.2 Radiometric Quantities and Reflectance Analysis

The underwater light field of the SoG can be generalized in terms of the influence of the plume of the Fraser River on its surface waters within the euphotic zone (i.e., above $Z_{1\%}$). Variations in the magnitude of the depth profile of $E_d(0\text{-},z,PAR)$ indicated higher attenuation of light in the first metres at stations close to the river than at more distant stations (Figure 12). In the case of stations S2-3 and S3-2 (not shown), this high attenuation was due to CDOM absorption and TSM scattering. Chl *a* fluorescence peaks were present in the $L_u(0\text{-},z,\lambda)$ spectra at around 685 nm at stations distant from the Fraser River. Chl *a* absorption troughs were visually apparent when the magnitude of the fluorescence peak was not so high as to hide its signal (Figure 13).

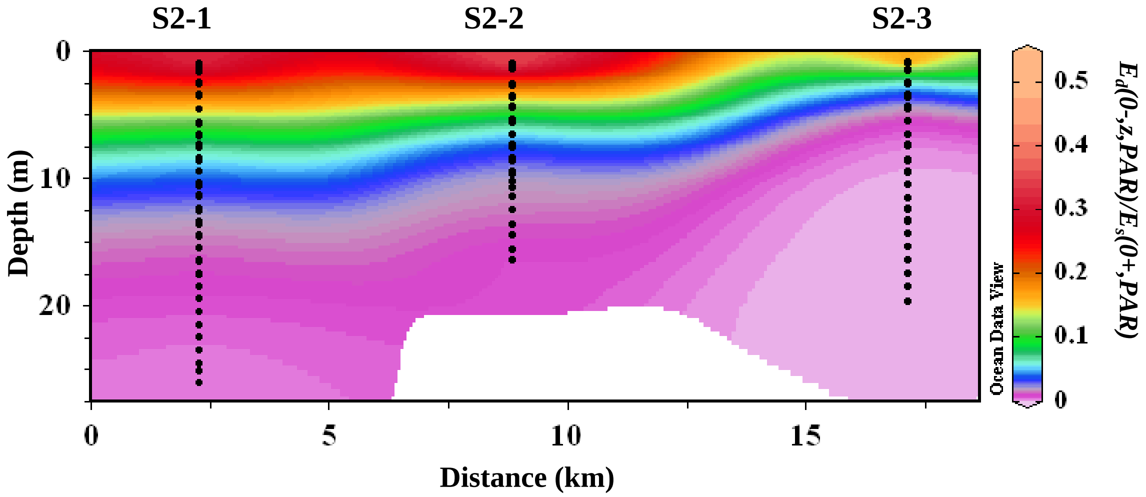

Figure 12 - Vertical profile of $E_d(0\text{-},z,PAR)/E_s(0+,PAR)$ showing the attenuation of $E_d(0\text{-},z,PAR)$ closer to the Fraser River (station S2-3). Less than 15% of $E_d(0\text{-},z,PAR)$ was found below 3 m at S2-3 in April and July.

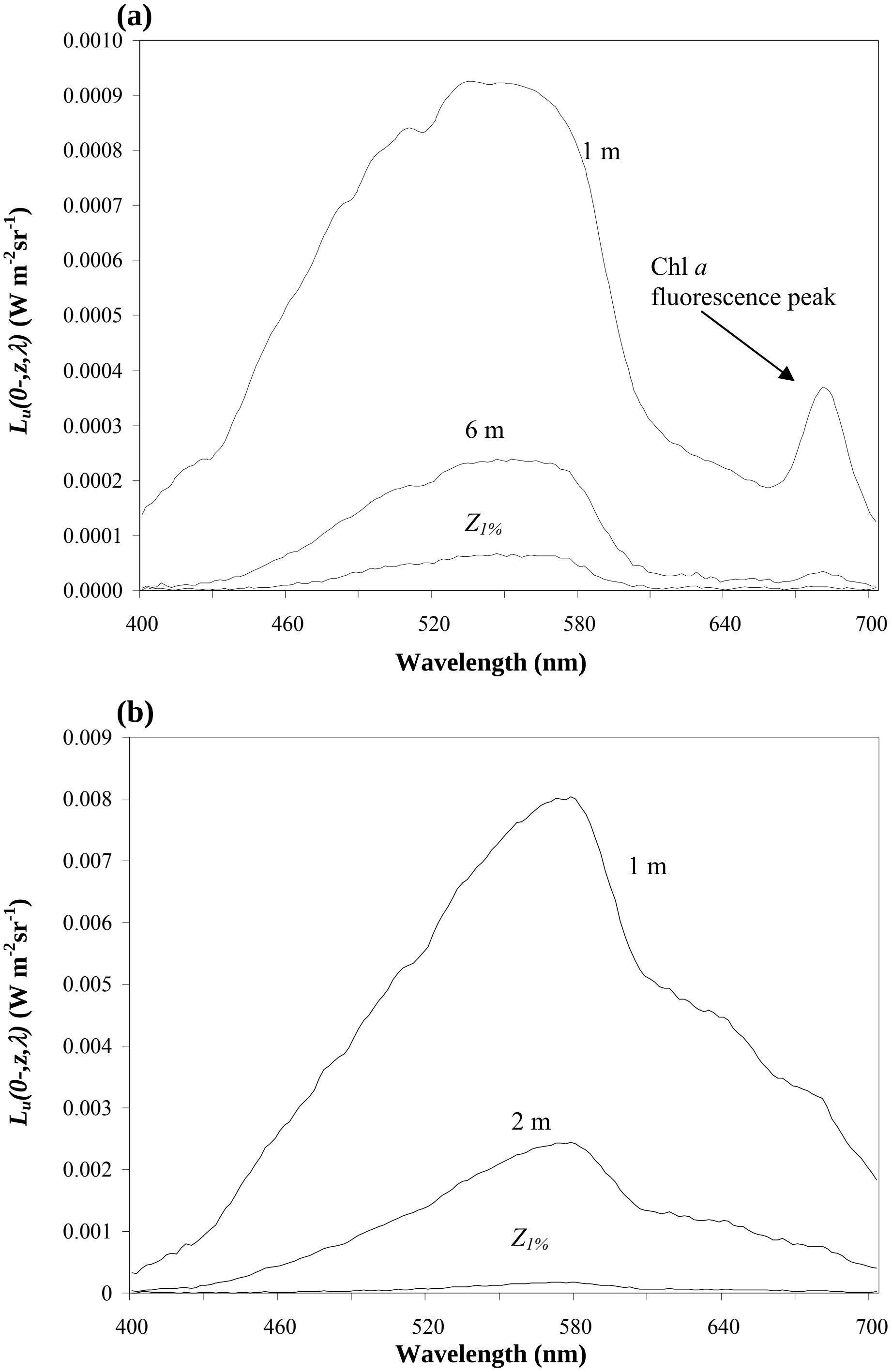

Figure 13 - In-water upwelling radiance, $L_u(0\text{-},z,\lambda)$, for stations S6-2 and S2-3 in July 2006 at three depths: 1 m, ½ $Z_{1\%}$, and $Z_{1\%}$. (a) Presence of chl *a* fluorescence around 685 nm at S6-2 and (b) lack of chl *a* fluorescence peak at S2-3 because of the high particulate scattering due to the high sediment load attributed to the discharge of the Fraser River.

The AOPs depend both on the IOPs of those waters and on the directional structure of the light field in those waters (Mobley, 1994). Thus, the spectral shapes of reflectance $R_r(0\text{-},z,\lambda)$ were affected by the water optical constituents. $R_r(0\text{-},z,\lambda)$ spectra varied in shape and magnitude in April and July, and according to their distance to the Fraser River. In general, $R_r(z,\lambda)$ spectra were a combination of *estuarine*, *fjord*, and *coastal* water types according to those defined by Roesler & Perry (1995), with magnitudes below 0.014 sr^{-1} in April and 0.012 sr^{-1} in July, except for those stations close to the Fraser River, where reflectance values were around 0.021 sr^{-1} in April and 0.040 sr^{-1} in July (Figure 14). Their classification roughly follows the optical classification developed here, with *estuarine* type being similar to OM1, *fjord* type being similar to OM2, and *coastal* type being a variation of OM2 more than OM3. Peaks around 550-590 nm reflected estuarine conditions and were seen at all stations in April with the exception of station S2-1. The reflectance spectra of station S2-1 resembled fjord conditions, which is characterised by a lower slope in the short wavelengths. There were however variations within those spectra with the lower slopes between 400 nm and the green peak being caused by CDOM and phytoplankton (Chang *et al.*, 2006). In July, $R_r(z,\lambda)$ profiles were typical of estuarine conditions with the exception of S4-1, S6-1, and S6-2. The $R_r(z,\lambda)$ spectra of S6-2 were probably a result of the dilution of the estuarine waters of the SoG. A closer inspection of the $R_r(z,\lambda)$ spectra of S6 and S6-1 indicated the northward transition from estuarine conditions (S6) into a mix of estuarine and fjord conditions (S6-1), and finally into fjord conditions (S6-2) (Figure 15). This was probably due to the circulation patterns in that region where the northward/southward circulation diluted (or prevented) the riverine and estuarine waters (Waldichuk, 1957; Thomson, 1981).

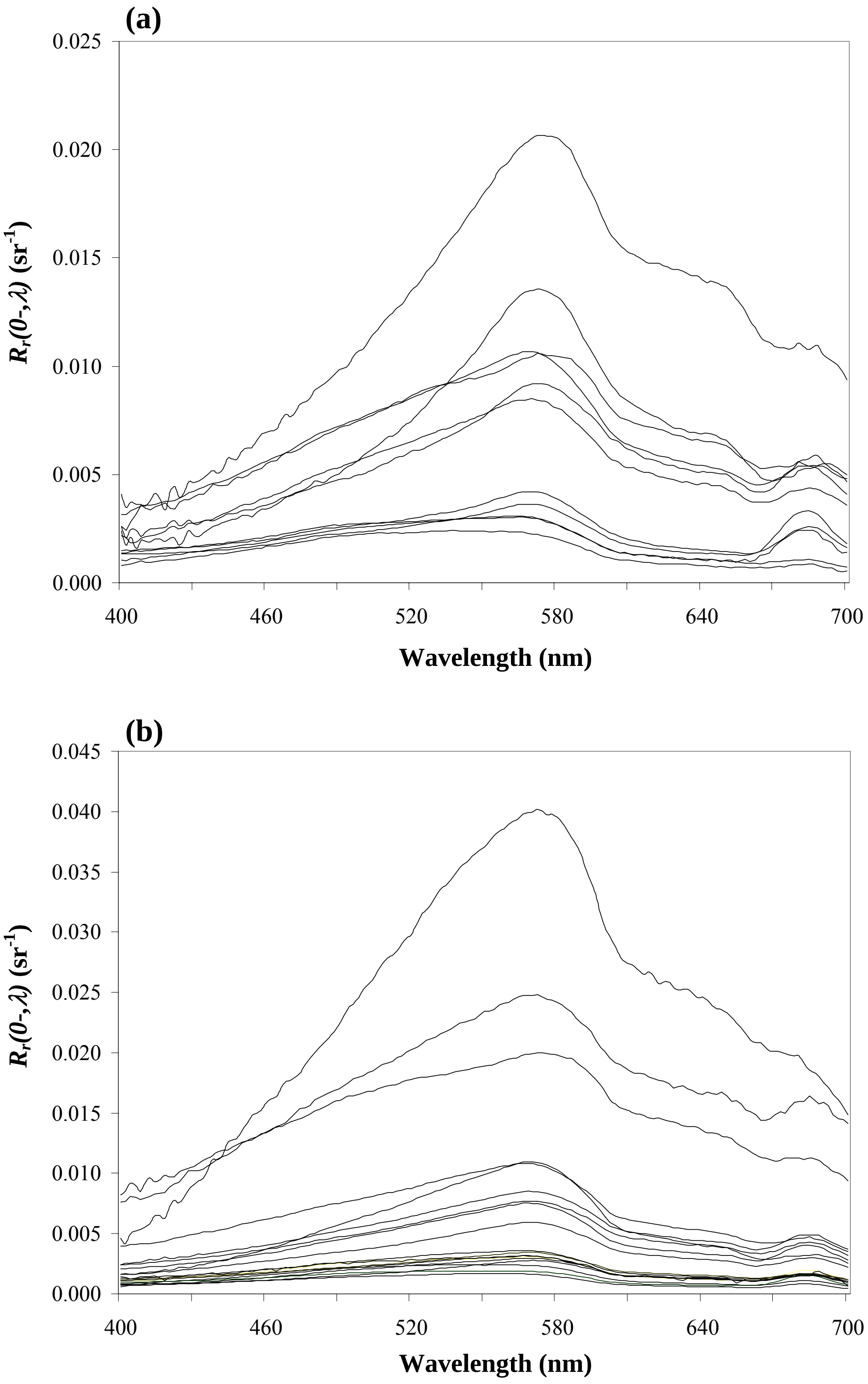

Figure 14 - Hyperspectral reflectance at the surface, $R_r(0\text{-},\lambda)$, in (a) April and (b) July 2006 for all stations.

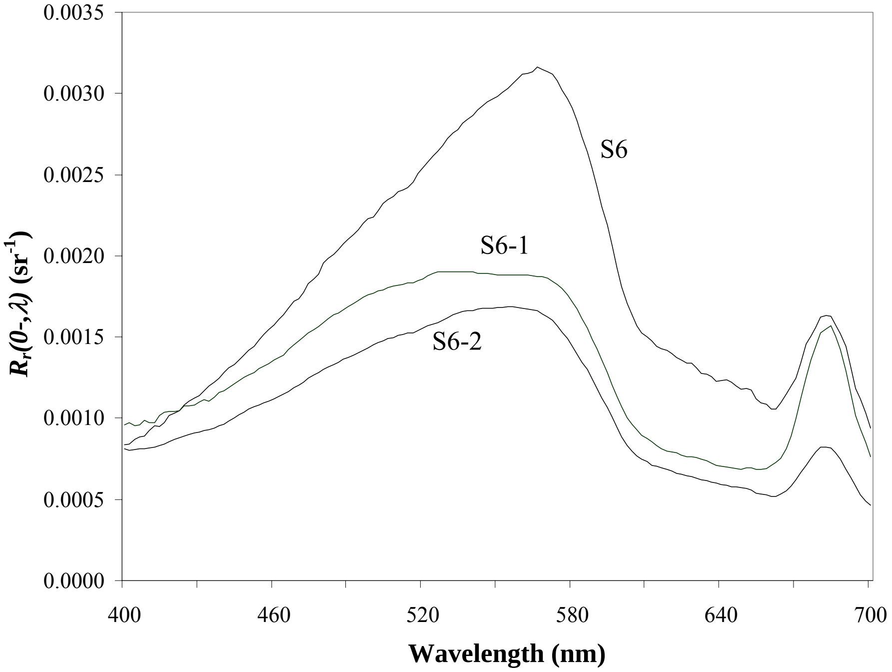

Figure 15 - Hyperspectral reflectance at the surface, $R_r(0\text{-},\lambda)$, in July 2006 for stations S6, S6-1, and S6-2 showing the transition from *estuarine* conditions at S6 into *fjord* conditions at S6-2.

In terms of the optical water masses defined here, the magnitudes of surface (first metre) reflectance means of OM1 in April and July were higher than those of OM2 and OM3, which were closer to each other (Figure 16). The reflectances of OM2 and OM3 were spectrally flatter when compared to the riverine plume waters of OM1. The high magnitude of $R_r(0\text{-},z,\lambda)$ between 550 and 600 nm was a consequence of the high scattering caused by TSM, which was the dominant optical constituent in OM1. The spectral dominance of CDOM was the cause behind the lower slopes of $R_r(0\text{-},z,\lambda)$ in OM2, where absorption by CDOM contributed more than the absorption and scattering by TSM to the total attenuation at 411 nm (Figure 11). The trend of decreasing influence of TSM continued into OM3, where $R_r(0\text{-},z,\lambda)$ was lowest and flattest of all three optical water masses. The peak at around 570 nm was still visible in April but not in July. Total absorption was dominated by CDOM in all wavelengths in OM3 in April and July; however, total attenuation was dominated by particulate scattering in the mid and longer wavelengths (from around 500 to 700 nm).

The optical signature of chl *a* was evident from the reflectance profiles of OM2 and OM3 and it was a direct result of those stations distant from the Fraser River. As expected, reflectance spectra at stations S2-3 and S3-2 did not exhibit the typical chl *a* fluorescence peak at around 685 nm whereas all the remaining stations exhibited a strong reflectance signal (Figure 17). This corroborated previous findings of TSM contribution to attenuation being much higher than the optical contribution of chl *a* in OM1.

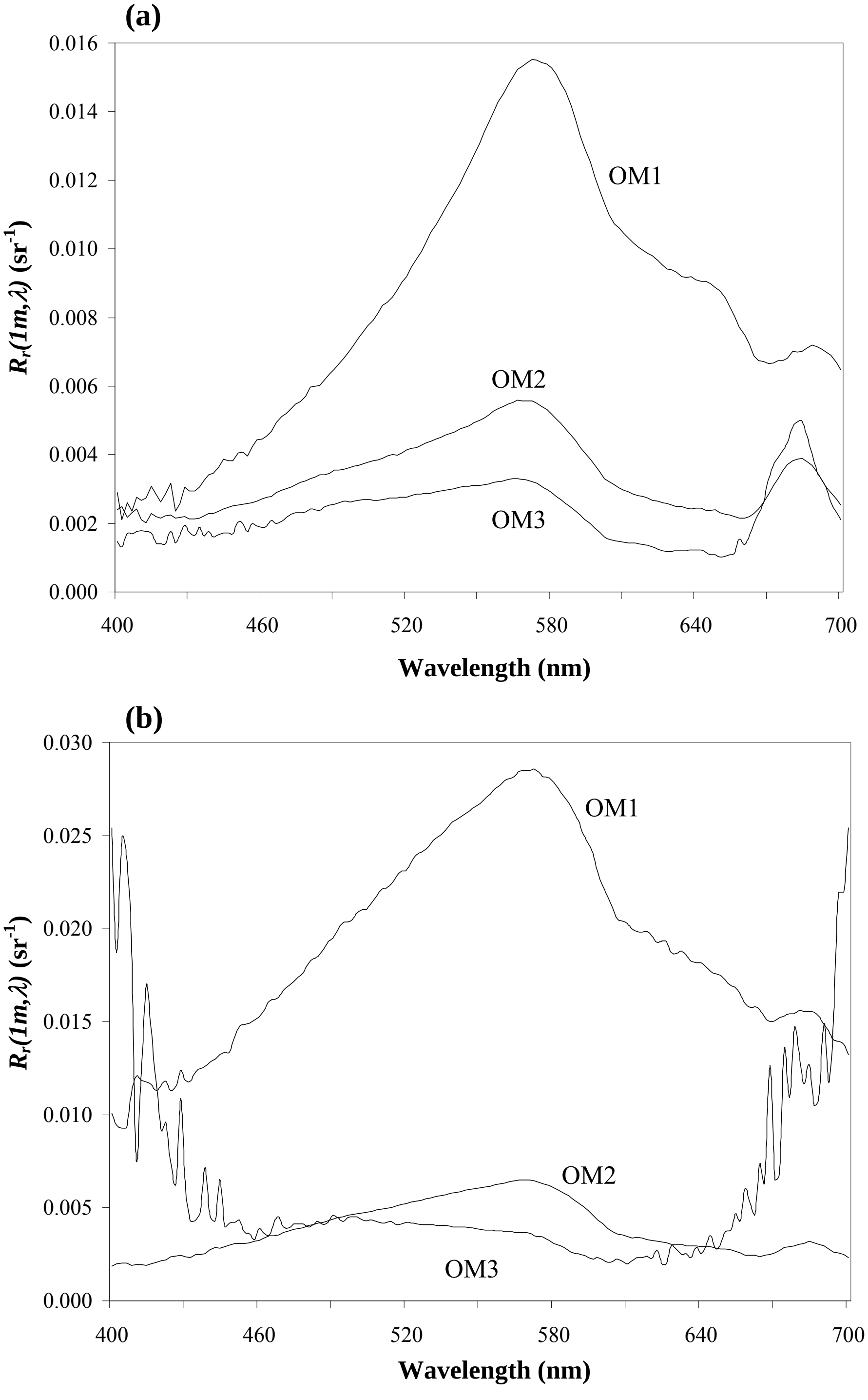

Figure 16 - Reflectance means for the first metre of each OM in (a) April and (b) July 2006.

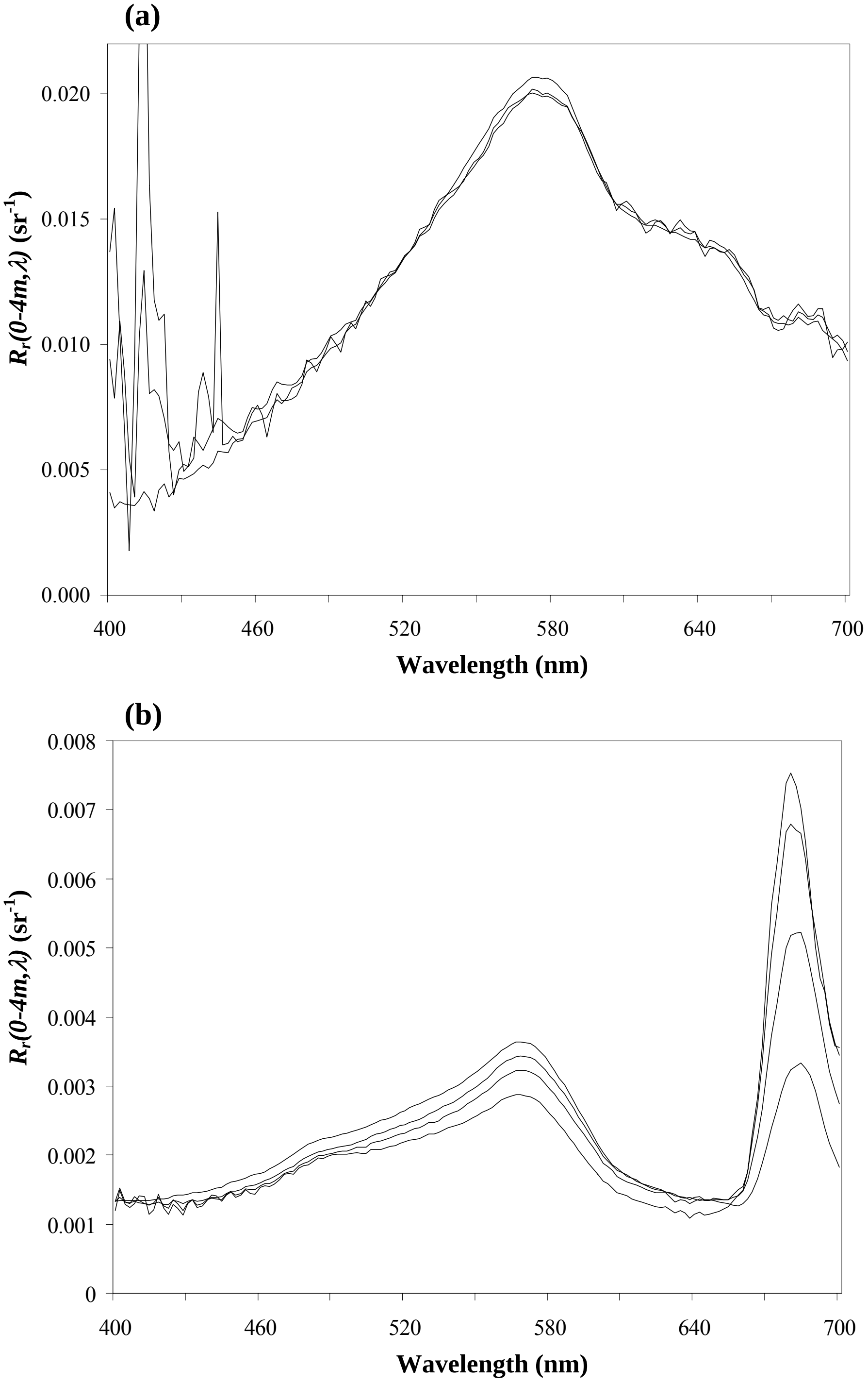

Figure 17 - Reflectance for the top four metres in April 2006 showing the absence and presence of the chl *a* fluorescence peak at 685 nm for stations (a) S2-3 and (b) S4-1, respectively.

3.2.3 Apparent Optical Properties - How the OMs Relate to Jerlov's Optical Water Types

Optical classifications of water masses have been proposed in the past (Jerlov, 1976; Pelevin & Rutkovskaya, 1977; Smith & Baker, 1978) with either $K_{Ed}(z,\lambda)$ or various IOPs being employed in the classification schemes. However, the use of AOPs for the purposes of classifying water masses is not as reliable as the use of IOPs (Prieur & Sathyendranath, 1981). The combination of different IOPs and the use of a clustering algorithm seemed to yield reasonable results here, with three optical water masses being classified. Nevertheless, the use of the classification scheme developed by Jerlov (1976) is still widely used by many researchers (Howard-Williams *et al.*, 1995; Reinart *et al.*, 1998; Højerslev & Aarup, 2002; Wild-Allen *et al.*, 2002) because of its simplicity and ease of comparison between water masses around the world.

In situ $K_{Ed}(z,\lambda)$ spectra for each optical water mass in April and July were compared to the Jerlov coastal water types (Jerlov, 1976) (Figure 18). OM1 waters were the most turbid of all three optical classes and were closer to the eastern side of the Strait. In April, $K_{Ed}(z,\lambda)$ values of OM1 exceeded those of Jerlov's most turbid coastal water type, coastal water type 9, throughout the visible spectral range, which is not unexpected since the Fraser River is an extraordinary source of particulates and organic matter (Milliman, 1980; Kostaschuk *et al.*, 1995; Luternauer *et al.*, 1998; Barrie & Currie, 2000; Stecko & Bendell-Young, 2000; Johannessen *et al.*, 2005), and Jerlov's classification scheme was based on coastal waters not directly affected by rivers of the magnitude of the Fraser River. In July, OM1 closely matched Jerlov type 9 in the short wavelengths but $K_{Ed}(z,\lambda)$ exceeded those of Jerlov's above 500 nm. Reinart *et al.* (2003) and Arst *et al.* (2008) encountered similar situations, albeit in their study of very turbid lakes, where $K_{Ed}(z,\lambda)$ values were one or two orders of magnitude higher than Jerlov's water type 9. The optical similarity between OM1 waters and turbid lake waters was due to the presence of high concentrations of TSM and CDOM that caused the high attenuation of light (both scattering and absorption) at surface throughout the visible optical spectrum. As the distance from the Fraser River increased, the magnitudes of the AOPs and IOPs decreased.

OM2 waters were found at all stations in April and July. Closer to the Fraser River, these waters were found below OM1, and as the distance from the river increased they were found at surface, extending down to the top of OM3. Because of their relatively larger distance to the South Arm of the Fraser River, the concentrations of the water optical constituents were lower at those stations. This in turn decreased the magnitudes of the AOPs and IOPs making these waters less turbid than OM1 waters. OM2 in April was of Jerlov type 7 until approximately 570 nm and somewhere between Jerlov types 7 and 9 above 570 nm (Figure 18). In July, OM2 was somewhere between Jerlov types 5 and 7.

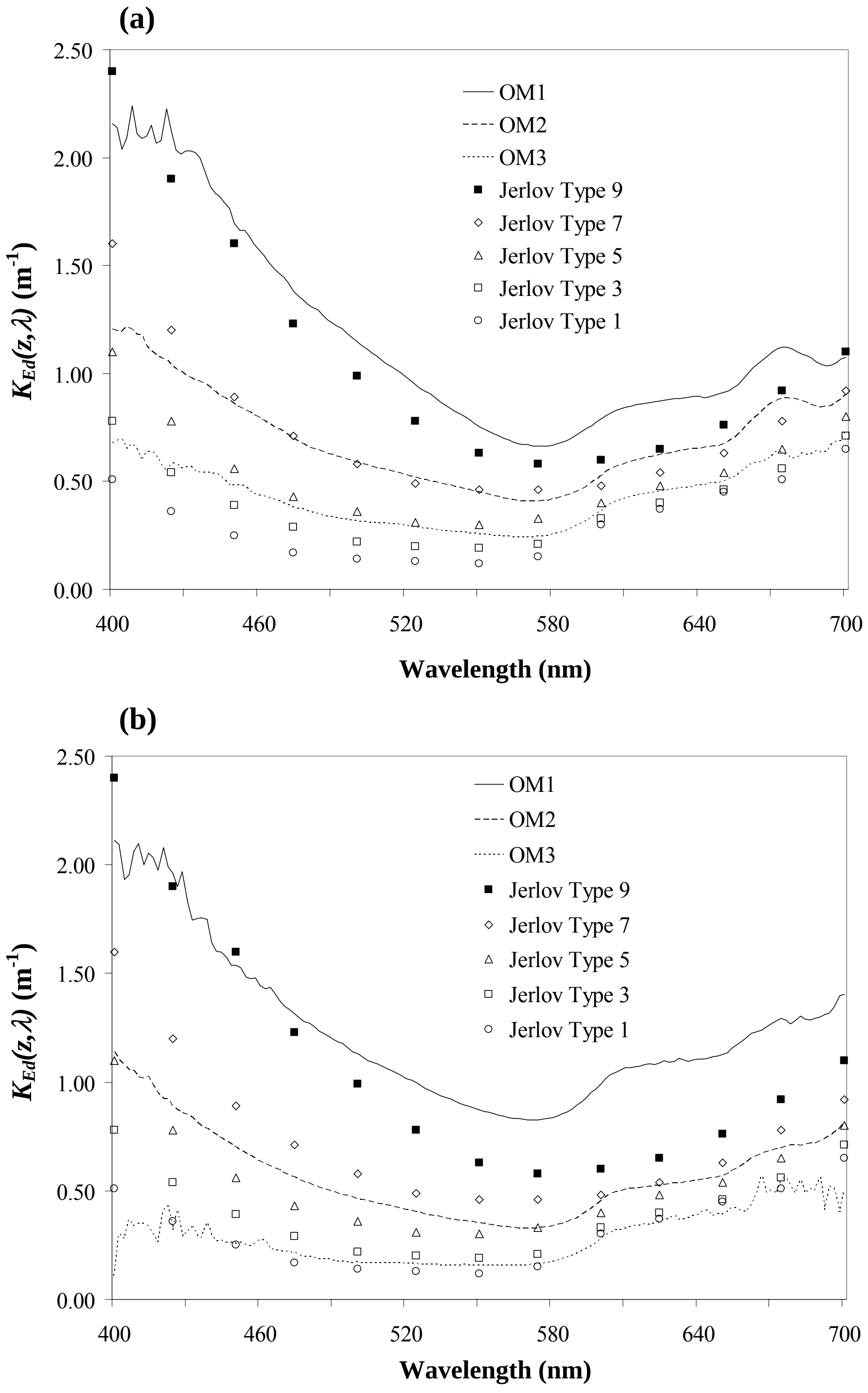

Figure 18 - $K_{Ed}(z,\lambda)$ **for (a) April and (b) July optical water masses (lines) and Jerlov water types (symbols).**

OM3 waters were the clearest of all three optical water masses, particularly in July, when OM3 could be considered Jerlov's type 1 (Figure 18). In April, OM3 waters were somewhere between Jerlov's types 3 and 5. The decrease in turbidity with depth was expected since the plume of the Fraser River carries TSM and CDOM at surface, giving OM1 its pronounced green hue, as seen in the reflectance peaks around 570 nm (Figure 16). In OM1 in April, $K_{Ed}(z,\lambda)$ was higher than in July in the short wavelengths because of the higher concentrations of CDOM. Similarly to $K_{Ed}(z,\lambda)$, $K_{Lu}(z,\lambda)$ spectra showed that the attenuation of upwelling radiance was the highest in OM1 and the lowest in OM3 (Figure 19). As well, higher $K_{Lu}(z,\lambda)$ values were also found in April with troughs between 550 and 600 nm.

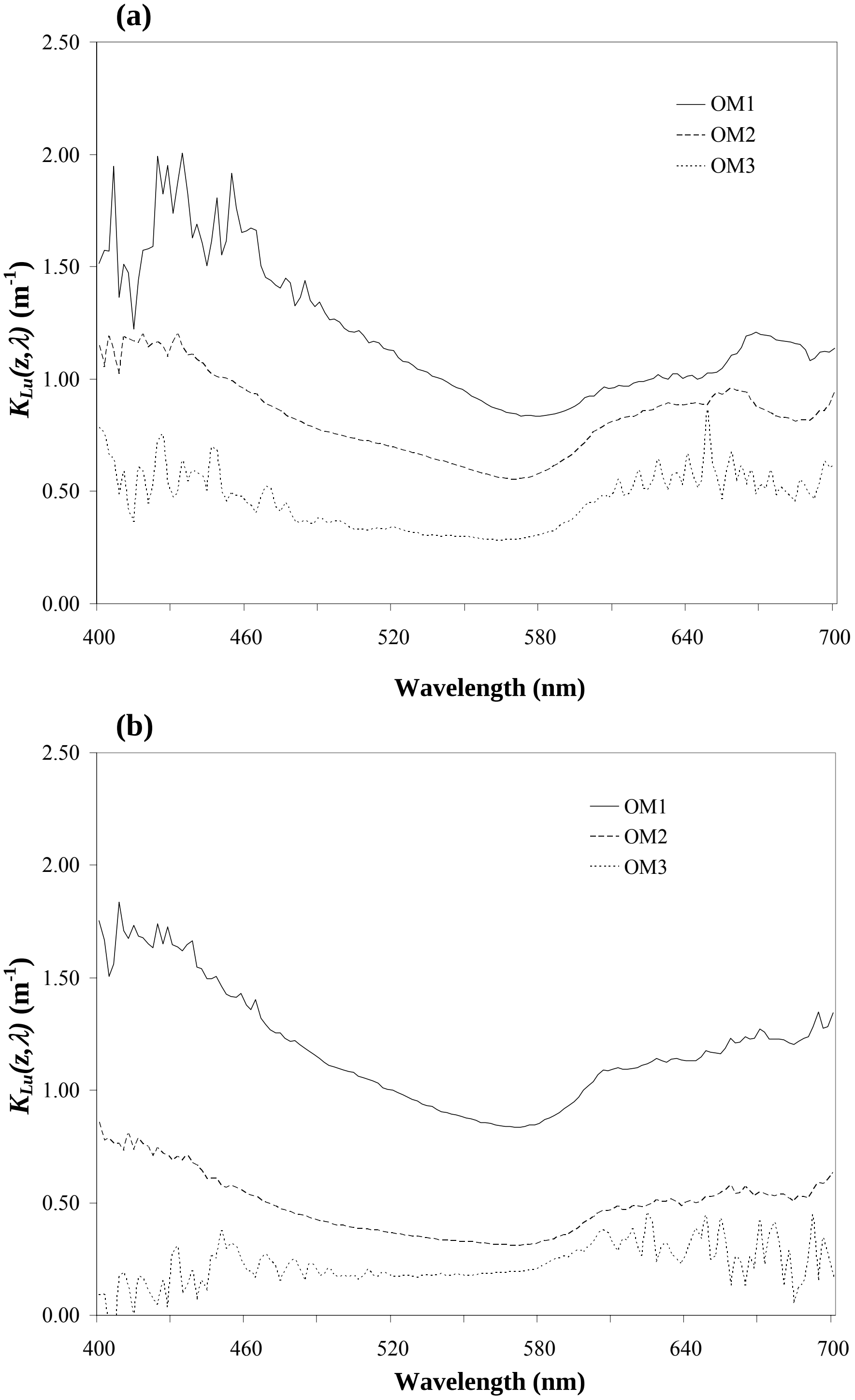

Figure 19 - $K_{Lu}(z,\lambda)$ for (a) April and (b) July optical water masses.

3.3 Radiative Transfer Modelling

Modelled data were compared with measured data in order to gain some confidence in the derived variables, thus validating Hydrolight simulations. For brevity, optical results will be presented for five wavelengths (411 nm, 530 nm, 650 nm, 675 nm, and 686 nm). Overall, Hydrolight output presented strong relationships with the measured optical data. The modelled and *in situ* radiometric quantities $E_d(0\text{-},z,\lambda)$ and $L_u(0\text{-},z,\lambda)$ were significantly related, as were the modelled and *in situ* diffuse attenuation coefficients $K_{Ed}(z,\lambda)$ and $K_{Lu}(z,\lambda)$ (Table 5). The relationship between modelled and measured radiance reflectance, $R_r(0\text{-},z,\lambda)$, was highest at 530 nm, and quite lower at the other wavelengths. $E_o(0\text{-},z,PAR)$ and $K_{Eo}(z,PAR)$ were also modelled in Hydrolight (Table 6).

Table 5 - Relationships between measured and modelled variables.

r^2	411		530		650		675		686	
	April	July	April	July	April	July	April	July	April	July
$E_d(0\text{-},z,\lambda)$	0.83	0.92	0.79	0.94	0.93	0.92	0.93	0.91	0.94	0.93
$L_u(0\text{-},z,\lambda)$	0.79	0.85	0.75	0.87	0.93	0.96	0.87	0.96	0.84	0.97
$K_{Ed}(z,\lambda)$	0.67	0.62	0.88	0.85	0.60	0.68	0.53	0.38	0.60	0.51
$K_{Lu}(z,\lambda)$	0.17	0.33	0.81	0.81	0.25	0.30	0.22	0.30	0.30	0.28
$R_r(0\text{-},z,\lambda)$	0.00*	0.02*	0.68	0.73	0.38	0.13	0.38	0.23	0.35	0.32

* statistically not significant at significance level of 0.05

Hydrolight also calculated some IOPs that were not measured *in situ*, such as chlorophyll absorption, $a_{chl}(z,\lambda)$, and total backscattering, $b_{bt}(z,\lambda)$ (Tables 7). Particulate backscattering, $b_{b'}(z,\lambda)$, is the result of pure water backscattering, $b_{bw}(z,\lambda)$, subtracted from $b_{bt}(z,\lambda)$. In general, $b_{b'}(z,\lambda)$ was highest in OM1 waters due to the presence of suspended particles, decreasing in magnitude toward OM3 and with depth (Figure 20; Table 7). The same general behaviour was observed with the backscattering ratios $b_{b'}(z,\lambda)/b_{p'}(z, \lambda)$. In order to assess the wavelength dependence of the backscattering coefficient and infer on the quality of the optical constituents present in the OMs, the parameter *B* of McKee & Buckingham (2005) was modified to

$$B_{wd} = [b_{b'}(z,411)/b_{p'}(z,411)] \,/\, [b_{b'}(z,675)/b_{p'}(z,675)] \tag{41}$$

using modelled backscattering coefficients and *in situ* particulate scattering coefficients. The relationship between B_{wd} and $b_{p'}(z,675)/a_{t'}(z,675)$ indicated that, in general, OM1 waters had less variability and lower wavelength dependence ($B_{wd} \approx 1.0$ in April and July) than OM2 and OM3 waters, where the backscattering coefficient had greater and more variable wavelength dependence (Figure 21). In general, this greater wavelength dependence of the scattering coefficient could be attributed to the presence of phytoplankton in OM2, thus dominating the particulate scattering and backscattering. Conversely, the lower wavelength dependence exhibited in OM1 and associated higher $b_{p'}(z,675)/a_{t'}(z,675)$ was caused by the higher concentrations of TSM in these waters.

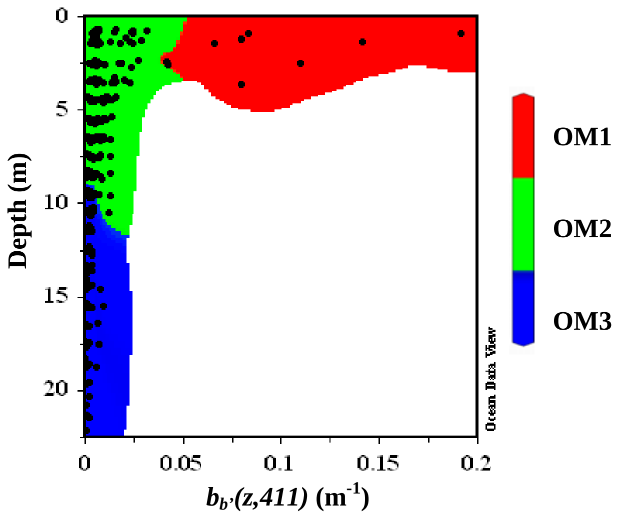

Figure 20 - Modelled backscattering coefficient at 411 nm for all stations in July in each optical water mass.

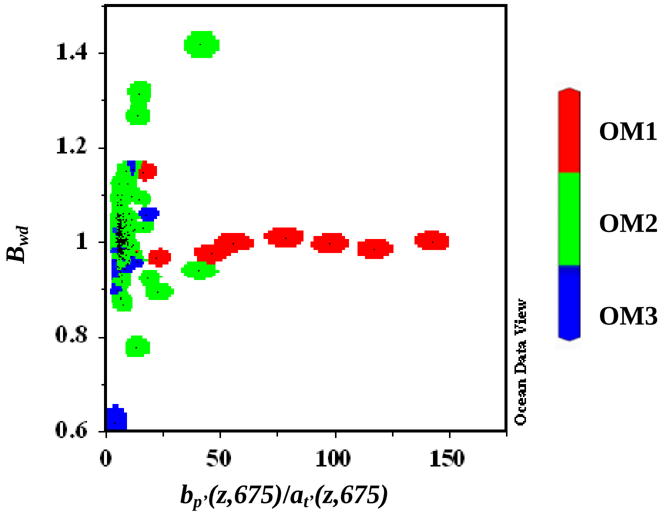

Figure 21 - In general, particulate backscattering in OM1 showed lower wavelength dependence than in OM2 and OM3 where B_{wd} was usually higher. This example illustrates only July stations.

Variations in the concentrations of optical constituents modified the light field in the optical water masses, which translated into effects on the IOPs and AOPs of these waters. These spectral changes in the light fields were more pronounced at shallow stations closer to the Fraser River where radiation was strongly attenuated (mainly caused by high scattering due to suspended sediments). These water masses were usually OM1 and OM2. As such, the relationship between physical depth and scalar optical depth was steeper for OM3 waters due to their lower attenuation values and shallower for OM1 and OM2 waters caused by their higher attenuation coefficients due to higher concentrations of particles (Figure 22).

Table 6 - Modelled $E_o(0-,z,PAR)$ and $K_{Eo}(z,PAR)$ (mean ± 1 S.D. and range) in April and July for the OMs.

	April		July	
	$E_o(0-,z,PAR)$ (μE m^{-2} s^{-1})	$K_{Eo}(z,PAR)$ (m^{-1})	$E_o(0-,z,PAR)$ (μE m^{-2} s^{-1})	$K_{Eo}(z,PAR)$ (m^{-1})
OM1	143.96 ± 132.46 15.20 - 398.00	0.99 ± 0.22 0.75 – 1.43	255.47 ± 210.47 16.70 – 628.00	1.48 ± 0.93 0.54 – 3.41
OM2	198.90 ± 183.29 18.9 - 780.00	0.32 ± 0.08 0.14 – 0.47	206.63 ± 276.27 2.03 – 1490	0.35 ± 0.25 0.00 – 1.40
OM3	62.80 ± 73.21 5.20 – 405.00	0.27 ± 0.21 0.12 - 0.88	29.10 ± 24.15 3.92 - 122	0.25 ± 0.51 0.00 - 3.66

Table 7 - Hydrolight output for five wavelengths (mean ± 1S.D.).

		411		530		650		675		686	
		April	July	April	July	April	July	April	July	April	July
$\bar{\mu}(z,\lambda)$	OM1	0.77±0.03	0.67±0.05	0.61±0.03	0.52±0.06	0.62±0.05	0.55±0.09	0.66±0.05	0.57±0.10	0.65±0.04	0.57±0.09
	OM2	0.81±0.04	0.82±0.03	0.71±0.06	0.74±0.05	0.78±0.05	0.80±0.05	0.73±0.07	0.75±0.07	0.69±0.08	0.70±0.12
	OM3	0.85±0.02	0.90±0.02	0.76±0.04	0.78±0.04	0.84±0.03	0.85±0.03	0.64±0.14	0.63±0.16	0.52±0.20	0.49±0.30
$E_d(0-,z,\lambda)$ (x 10^2) (W m^{-2} nm^{-1})	OM1	0.91±1.83	2.19±3.27	8.55±8.00	14.57±11.30	7.00±6.10	10.24±8.13	5.26±5.52	8.28±7.56	4.53±4.74	6.95±6.46
	OM2	1.96±3.51	3.44±8.51	17.76±14.04	19.18±23.15	6.75±8.25	8.23±13.96	3.70±5.38	5.75±11.49	3.33±4.86	4.84±9.93
	OM3	0.67±2.16	0.02±0.04	7.04±6.30	4.40±3.82	1.44±3.04	0.21±0.32	0.85±2.45	0.06±0.10	0.70±2.01	0.04±0.07
$L_u(0-,z,\lambda)$ (x 10^2) (W m^{-2} sr^{-1} nm^{-1})	OM1	0.002±0.005	0.015±0.024	0.078±0.082	0.25±0.26	0.058±0.066	0.17±0.23	0.037±0.048	0.13±0.18	0.04±0.04	0.11±0.15
	OM2	0.003±0.005	0.005±0.011	0.074±0.078	0.059±0.070	0.013±0.0.22	0.013±0.025	0.016±0.020	0.015±0.024	0.022±0.027	0.018±0.028
	OM3	0.001±0.002	$3.53 \cdot 10^{-5} \pm 5.99 \cdot 10^{-5}$	0.023±0.026	0.010±0.007	0.001±0.003	$2.19\ 10^{-4} \pm 2.49\ 10^{-4}$	0.003±0.005	$6.54\ 10^{-4} \pm 6.26\ 10^{-4}$	$4.44\ 10^{-3} \pm 6.73\ 10^{-3}$	$9.21\ 10^{-4} \pm 8.78\ 10^{-4}$
$K_{Ed}(z,\lambda)$ (m^{-1})	OM1	2.28±0.52	2.01±0.67	0.69±0.14	0.84±0.35	0.68±0.06	0.87±0.22	0.87±0.06	1.01±0.19	0.86±0.05	1.03±0.09
	OM2	0.75±0.22	0.73±0.27	0.26±0.08	0.26±0.10	0.52±0.07	0.49±0.06	0.69±0.13	0.61±0.09	0.67±0.10	0.63±0.10
	OM3	0.48±0.09	0.43±0.10	0.15±0.03	0.15±0.03	0.42±0.02	0.42±0.02	0.48±0.11	0.45±0.10	0.46±0.13	0.42±0.13
$K_{Lu}(z,\lambda)$ (m^{-1})	OM1	2.43±0.65	2.31±0.69	0.86±0.22	1.12±0.34	0.92±0.17	1.18±0.27	1.08±0.16	1.24±0.30	1.07±0.20	1.21±0.34
	OM2	0.78±0.28	0.73±0.30	0.31±0.12	0.29±0.14	0.64±0.20	0.57±0.26	0.46±0.23	0.47±0.20	0.43±0.22	0.45±0.19
	OM3	0.47±0.07	0.42±0.11	0.145±0.03	0.14±0.03	0.38±0.20	0.42±0.21	0.32±0.19	0.46±0.55	0.31±0.19	0.40±0.26
$R_r(0-,z,\lambda)$ (x 10^3) (sr^{-1})	OM1	2.00±0.51	6.00±2.00	8.00±2.00	17.00±7.00	7.00±3.00	15.00±10.00	6.00±2.00	13.00±8.00	6.50±2.00	13.60±7.50
	OM2	1.58±0.58	1.70±0.60	4.00±1.95	4.00±3.00	1.53±0.83	1.78±1.78	9.00±10.00	8.00±9.00	12.00±10.00	14.40±17.90
	OM3	1.40±0.29	1.45±0.42	3.00±1.00	2.00±1.44	1.60±1.15	1.83±1.66	28.00±27.00	29.00±28.00	45.60±40.70	50.80±43.04
$b_{b'}(z,\lambda)$ (m^{-1})	OM1	0.041±0.015	0.091±0.050	0.038±0.015	0.088±0.052	0.036±0.014	0.083±0.052	0.035±0.015	0.082±0.053	0.035±0.014	0.082±0.053
	OM2	0.007±0.005	0.008±0.006	0.008±0.005	0.007±0.006	0.007±0.005	0.007±0.006	0.006±0.005	0.006±0.005	0.007±0.005	0.007±0.006
	OM3	0.002±0.001	0.002±0.002	0.003±0.002	0.002±0.001	0.002±0.002	0.002±0.001	0.002±0.001	0.002±0.001	0.002±0.001	0.002±0.001
$b_{b'}(z,\lambda)/b_{p'}(z,\lambda)$	OM1	0.010±0.003	0.014±0.006	0.010±0.003	0.014±0.007	0.010±0.003	0.014±0.007	0.010±0.003	0.014±0.007	0.010±0.003	0.014±0.007
	OM2	0.009±0.005	0.012±0.006	0.009±0.005	0.012±0.007	0.009±0.005	0.012±0.007	0.009±0.005	0.012±0.007	0.009±0.005	0.012±0.007
	OM3	0.008±0.004	0.011±0.007	0.008±0.004	0.011±0.007	0.008±0.004	0.011±0.007	0.008±0.004	0.011±0.007	0.008±0.004	0.011±0.007
$a_{chl}(z,\lambda)$ (m^{-1})	OM1	0.118±0.034	0.077±0.048	0.067±0.019	0.043±0.027	0.051±0.015	0.033±0.021	0.078±0.023	0.050±0.031	0.056±0.016	0.036±0.023
	OM2	0.137±0.046	0.100±0.047	0.077±0.026	0.057±0.026	0.059±0.020	0.043±0.020	0.090±0.030	0.066±0.031	0.065±0.021	0.047±0.022
	OM3	0.075±0.044	0.060±0.044	0.042±0.025	0.034±0.025	0.032±0.019	0.026±0.019	0.049±0.029	0.040±0.030	0.035±0.021	0.028±0.021
$E_o(0-,z,\lambda)$ (x 10^2) (µE m^{-2} s^{-1})	OM1	1.20±2.42	3.24±4.85	13.50±12.62	25.69±20.53	10.93±9.74	17.62±14.94	7.97±8.50	13.86±13.51	6.90±7.31	11.63±11.50
	OM2	2.44±4.34	4.14±10.05	24.89±19.88	14.62±28.28	8.93±11.14	10.15±16.76	4.87±7.15	7.07±13.76	4.49±6.56	6.03±12.00.
	OM3	0.81±2.60	0.03±0.05	9.27±8.33	5.52±4.68	1.75±3.70	0.25±0.39	1.05±2.96	0.07±0.12	0.88±2.44	0.06±0.10
$E_d(0-,z,\lambda)/E_s(0+,z,\lambda)$	OM1	0.008±0.014	0.127±0.393	0.073±0.089	0.078±0.095	0.090±0.107	0.193±0.470	0.072±0.095	0.088±0.148	0.073±0.110	0.080±0.122
	OM2	0.011±0.034	0.030±0.072	0.066±0.109	0.134±0.165	0.033±0.065	0.070±0.122	0.020±0.045	0.052±0.102	0.021±0.042	0.047±0.110
	OM3	0.013±0.043	0.000±0.001	0.077±0.118	0.021±0.022	0.025±0.068	0.001±0.002	0.018±0.057	0.001±0.001	0.018±0.049	0.001±0.001
$E_o(0-,z,\lambda)/E_o(0+,z,\lambda)$	OM1	0.016±0.031	0.029±0.047	0.154±0.141	0.216±0.180	0.159±0.141	0.152±0.130	0.113±0.121	0.117±0.114	0.114±0.120	0.111±0.110
	OM2	0.021±0.036	0.031±0.064	0.172±0.111	0.152±0.137	0.071±0.076	0.079±0.110	0.039±0.051	0.055±0.091	0.040±0.052	0.053±0.090
	OM3	0.014±0.042	0.000±0.001	0.120±0.106	0.036±0.022	0.029±0.062	0.002±0.003	0.018±0.049	0.001±0.001	0.017±0.046	0.001±0.001

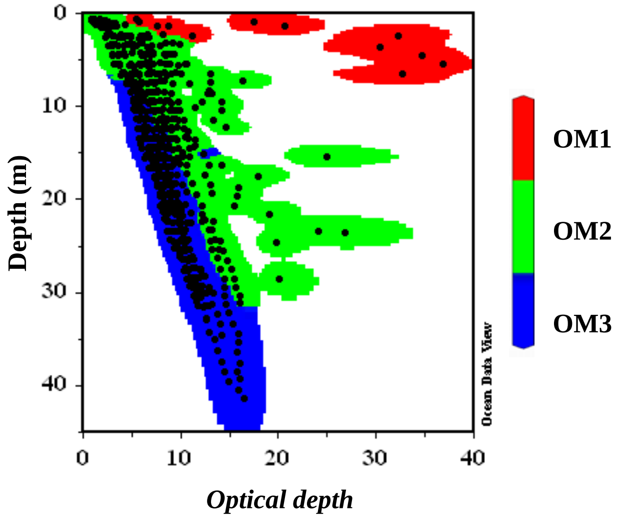

Figure 22 - Optical depth for July stations in each optical water mass. The slopes of the optical depths were much steeper for OM2 and OM3 than for OM1 because of their attenuation coefficients.

Average cosine values given by equation 21 and modified to underwater light fields (Equation 42) describe the total underwater irradiance distribution.

$$\bar{\mu}(z,\lambda) = \frac{E_d(0-,z,\lambda) - E_u(0-,z,\lambda)}{E_o(0-,z,\lambda)} \tag{42}$$

The high scattering of OM1 waters created a very diffuse light field thus yielding low $\bar{\mu}(z,\lambda)$ values (Figure 23). Conversely, OM3 waters presented the highest $\bar{\mu}(z,\lambda)$ values indicating that these were the clearest waters of all three optical water masses. In general, lower $\bar{\mu}(z,\lambda)$ indicate higher scattering and backscattering coefficients. Consequently, $\bar{\mu}(z,\lambda)$ was lowest closest to the Fraser River and highest away from the river and at depth. Additionally, the absorption-to-scattering ratios $a_{t'}(z,411)/b_{p'}(z,411)$ and $a_{t'}(z,411)/b_{p'}(z,530)$ were lower closer to the Fraser River than at stations away from the direct influence of the river (Figure 24).

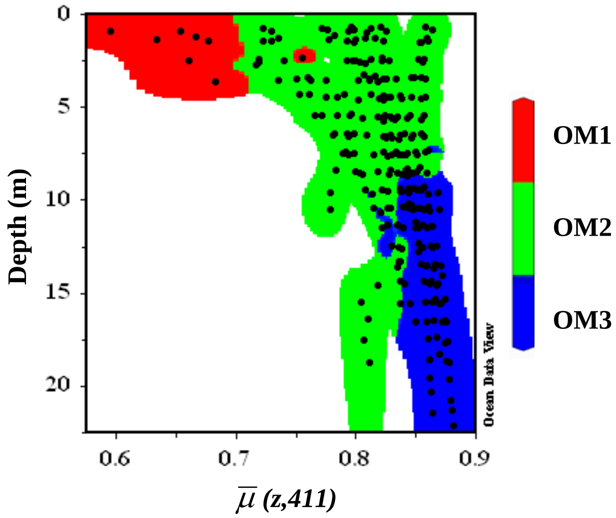

Figure 23 - Average cosines for all three optical water masses in July. OM1 had the lowest average cosines because of their high attenuation due to particulate scattering.

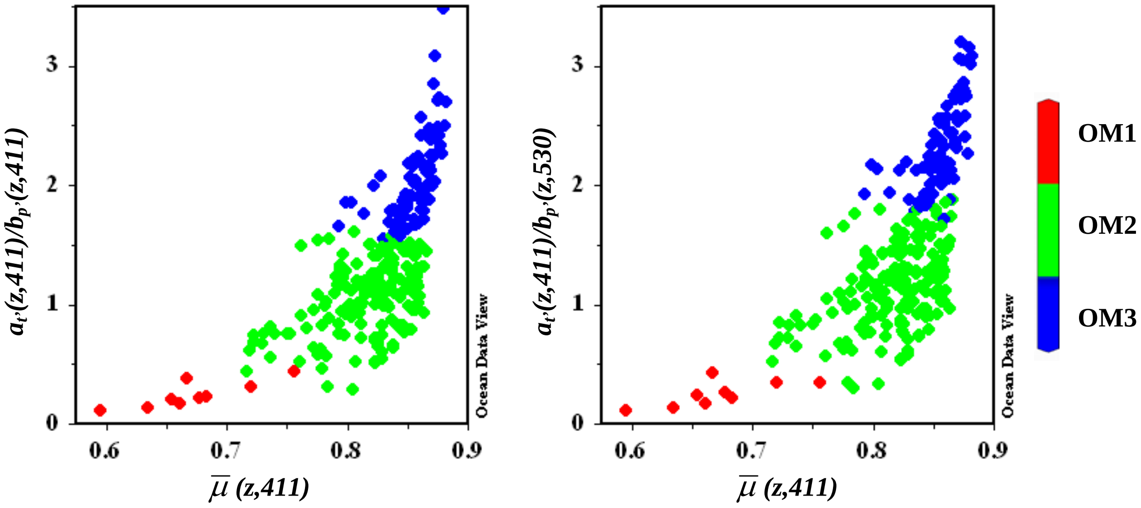

Figure 24 - Relationship between average cosine at 411 nm and absorption-to-scattering ratios in July.

Absorption by chlorophyll-bearing particles, $a_{chl}(z,\lambda)$, was modelled in Hydrolight based on the chlorophyll concentrations given by the HPLC. The highest concentrations of phytoplankton and $a_{chl}(z,\lambda)$ were found in OM2 waters (Figure 25), and occasionally in OM1. The relationships between $a_{chl}(z,675)$ and chl *a* concentration were high ($r^2_{Apr} = 0.88$, $r^2_{Jul} = 0.95$).

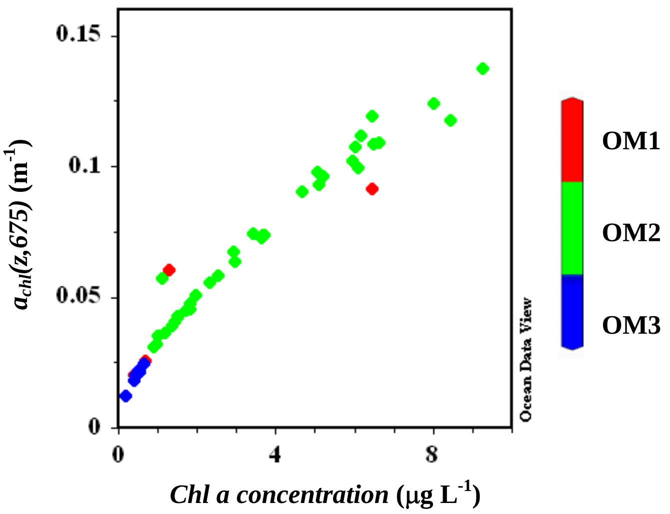

Figure 25 - Relationship between chl *a* concentration and modelled chl *a* absorption at 675 nm in July for all three optical water masses.

Scalar irradiances, $E_o(0\text{-},z,\lambda)$, at the wavelengths specified above were dominated by green-red wavelengths as most of the shorter wavelengths were absorbed in the water column by CDOM and phytoplankton. The profiles of normalised scalar irradiances, $E_o(0\text{-},z,\lambda)/E_o(0\text{+},\lambda)$, demonstrated that blue (411 nm) and long red (675 nm, 686 nm) wavelengths were quickly attenuated within the first five metres to levels below 10% of the total incident $E_o(0\text{+},\lambda)$ (Figure 26).

Modelled and *in situ* downwelling PAR, $E_d(0\text{-},z,PAR)$, were significantly correlated (r_{April}= 0.95, r_{July} = 0.97). PAR scalar irradiance, $E_o(0\text{-},z,PAR)$, was modelled by Hydrolight and used to assess the amount of light available to phytoplankton. This is because $E_o(0\text{-},z,PAR)$, unlike $E_d(0\text{-},z,PAR)$, is the integral of the radiances over all angles around a point and not just the downwelling component of irradiance (Mobley, 2001). Phytoplankton cells should be able to utilize irradiances for photosynthesis from all directions (Bergmann *et al.*, 2004).

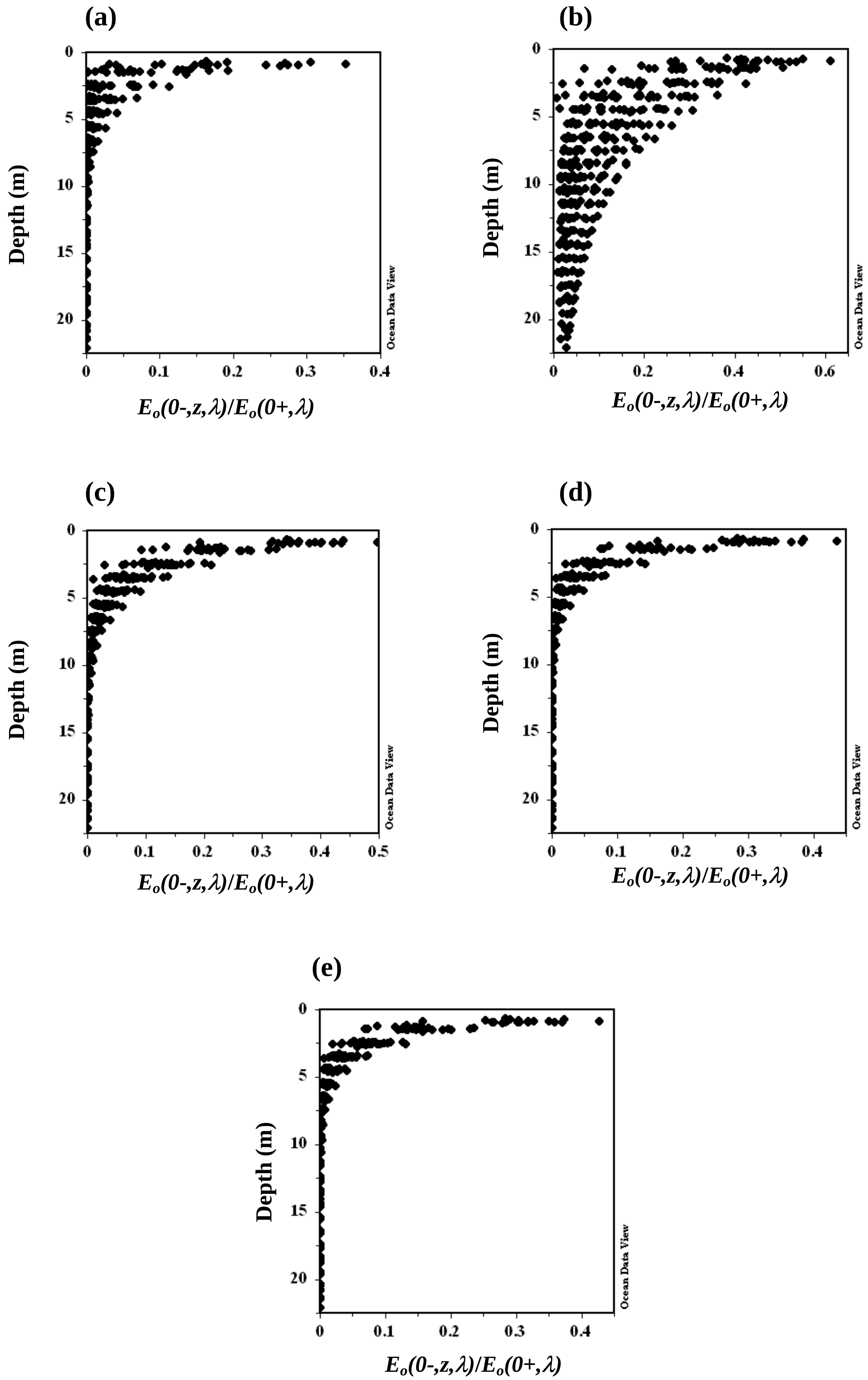

Figure 26 – Ratio between in-water downwelling scalar irradiance and above-water downwelling scalar irradiance in April and July at (a) 411 nm, (b) 530 nm, (c) 650 nm, (d) 675 nm, and (e) 686 nm for all stations.

3.4 Comparison of OM Classification Methods

The optical water mass classification scheme developed here made use of IOPs measured *in situ*. The clustering of $c_{t'}(z,411,650)$, $a_{t'}(z,411)/b_{p'}(z,411)$, and $a_{t'}(z,411)/b_{p'}(z,530)$ was the best representation of the optical characteristics of the water masses of the SoG when compared to their hydrographic characteristics.

The modelled data provided by Hydrolight allowed for the further examination of this optical classification. Substituting particulate backscattering coefficient, $b_{b'}(z,\lambda)$, for $c_{t'}(z,\lambda)$ yielded similar results to the initial OM classification, with a correlation r of 0.67 in April and 0.94 in July, which turned out to be the best (Table 8). Other combinations yielded much weaker correlations; the clustering algorithm correctly classified OM1 waters but was not able to provide as clear a distinction between OM2 and OM3 as that provided by the original combination of attenuation and absorption-to-scattering ratios. It is apparent that the ratios $a_{t'}(z,411)/b_{p'}(z,411)$ and $a_{t'}(z,411)/b_{p'}(z,530)$ proved to be essential in distinguishing the three optical water masses.

The clustering of modelled AOPs proved more difficult to clearly define optical water masses than with IOPs. Different clustering strategies were employed using some of the modelled variables: $K_{Ed}(z,\lambda)$, $R_r(0\text{-},z,\lambda)$, and $\overline{\mu}(z,\lambda)$. The clustering of $\overline{\mu}(z,411,530,650)$ yielded OMs similar to those obtained from IOPs with a correlation coefficient r of 0.64 in April and 0.52 in July. Table 8 presents the best correlations.

Table 8 - Correlations between clustering of optical water masses using the parameters of section 3.2 and and clusterings using modelled IOPs and AOPs. All correlations were significant at a 99% confidence level.

Correlation r	April	July
$b_{b'}(z,411,650)$ $a_{t'}(z,411)/b_{p'}(z,411)$ $a_{t'}(z,411)/b_{p'}(z,530)$	0.67	0.94
$\overline{\mu}\ (z,411,530,650)$	0.64	0.52
$R_r(0\text{-},z,411,650)$ $K_{Ed}(z,411)/K_{Ed}(z,530)$	0.39	0.46
$R_r(0\text{-},z,411,650)$ $K_{Ed}(z,411)/K_{Ed}(z,650)$	0.44	0.54
$R_r(0\text{-},z,411,650)$ $K_{Ed}(z,411)/K_{Ed}(z,530)$ $K_{Ed}(z,411)/K_{Ed}(z,650)$	0.59	0.51

Chapter 4: Discussion

4.1 Optical Water Masses

The results of the vertical and horizontal distributions of the IOPs, AOPs, radiometric quantities, and optical constituents of the waters of the SoG within the euphotic zone provided a glimpse of optical dynamics in the SoG for the first time. For the study period, which represented the beginning of spring and summer conditions, the optical variability of these waters was a function of the assemblage of optical constituents, which in turn was related to the discharge of the Fraser River and the oceanographic conditions of the SoG.

April was characterized by lower river discharge than July, as well as lower temperatures, presenting a scenario more similar to that of winter conditions than of summer in the waters of the SoG (Waldichuk, 1957; Thomson, 1981; Li *et al.*, 2000). Salinities were similar during both cruises, although in July, when the river discharge was high, the low-salinity waters which defined the Fraser River plume were fresher and covered a larger area than they did in April (Figure 3). These waters with relatively lower salinities were also clearly defined in terms of their inherent optical properties, being classified as OM1 or plume waters. OM2 or estuarine waters were mostly located at the c-cline, thus their transitional nature. OM3 were deeper, northern waters less influenced by the Fraser River. Regardless of the classification of the optical water masses, scattering by particles in general prevailed over absorption in the attenuation of light, except in the short wavelengths for deeper waters or waters farther from the discharge of the Fraser River (OM3 and OM2, respectively), where absorption started to play a more important role in the attenuation of light (Figure 11). Figure 27 illustrates this pattern spatially, where $a_{t'}(z,411)/b_{p'}(z,411)$ increased considerably from OM1 to OM3, thus showing the increased importance of absorption to attenuation at short wavelengths.

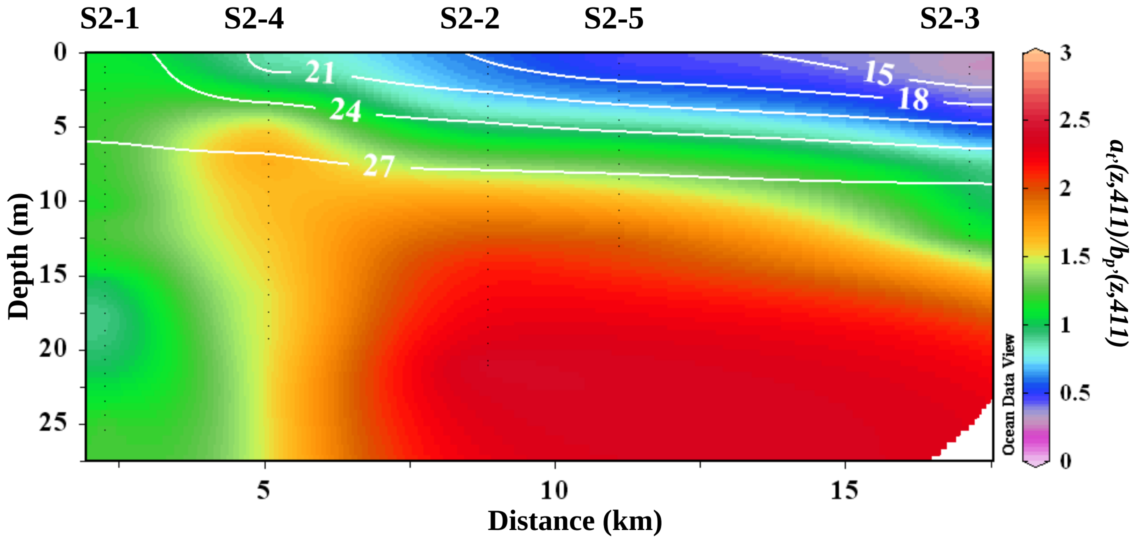

Figure 27 - Transect of stations (from West to East) S2-1, S2-4, S2-2, S2-5, and S2-3 in July 2006. Ratio between absorption, $a_{t'}(z,411)$, and particulate scattering , $b_{p'}(z,411)$, increased from OM1 to OM3, thus showing the increased importance of absorption to attenuation at short wavelengths. Colours depict $a_{t'}(z,411)/b_{p'}(z,411)$ and isolines depict salinity.

For OM1 waters, where the attenuation of light was the highest, the high wavelength-independent contribution of particulate scattering to attenuation was mostly due to the Fraser River discharge that carried a large load of particles into the SoG in the spring and summer. In these waters, particulate matter is known to be dominated by the inorganic fraction, mostly fine clays, silts, and very fine sand (Kostaschuk *et al.*, 1998). These fine particles that originate in the Fraser watershed (glaciated mountains, forested areas) are known to attenuate radiation strongly (Gallie & Murtha, 1992). The measured high values of attenuation throughout the sampled spectrum (~ 16.0 m^{-1}, Figure 6a) reflected the high loads of inorganic particles, as shown in other estuaries of the world, such as in the North and Baltic Seas (Babin *et al.*, 2003), Rhode River in Chesapeake Bay (Gallegos *et al.*, 2005), and rivers in France and in the UK (Doxaran *et al.*, 2006). These values were much higher than those measured by Johannessen *et al.* (2006) at the South Arm of the Fraser River at surface (~2.0 m^{-1} at 660 nm), but of around the same magnitude for other locations in the world. The difference in magnitude could be probably attributed to different optical constituent assemblages, perhaps with a higher concentration of scatterers at the time of sampling for this study. Furthermore, the absence of the absorption peak at 675 nm in these waters (Figure 6a) when compared to the waters under lower influence of the riverine discharge (Figure 7a), suggests that inorganic particles dominated the attenuation of light in spite of the presence of phytoplankton, as has been reported for similar waters (Blondeau-Patissier *et al.*, 2004). Nonetheless, to differentiate accurately between the influences of inorganic minerals and phytoplankton in the scattering by particles, one would need to estimate the index of refraction n based on *in situ* measurements of backscattering. The index of refraction is a proxy for TSM concentrations, as high n values indicate the presence of inorganic minerals, whereas phytoplankton and organic detritus usually have lower n values due to their higher water content (Babin *et al.*, 2003; Boss *et al.*, 2004; Stramski *et al.*, 2004).

It is possible that scattering by particles was responsible for the low chl *a* concentration observed in OM1 as a result of shading, as has been observed in other estuaries, such as the Amazon and San Francisco Bay (Edmond *et al.*, 1981; Cloern, 1987). However, according to Bergmann *et al.* (2004) it is also possible that particulate scattering caused an increase of diffuse light in the water, and therefore enough light was redirected downward and still available below the plume waters for absorption by phytoplankton. This would explain in part why the highest concentrations of chl *a* were found not in the river plume but rather below the plume, in OM2. However, *in situ* and modelled data collected in this study showed that it was not the case here. Other authors have found high concentrations of chl *a* below the plume waters of the SoG (Harrison *et al.*, 1991; Li *et al.*, 2000). Another possible explanation would be entrainment of deepwater nutrients directly into the base of the Fraser River plume as well as the advection of phytoplankton (Mackas & Harrison, 1997; Yin *et al.*, 1997b).

In OM1 waters, particles also dominated the measured total absorption, even though CDOM concentration was highest in this water mass. Most notably, CDOM concentrations in April were much higher than those in July, at times more than doubled (station S2-3) (32.1 ppb QSDE in April; 15.7 ppb QSDE in July). The Fraser River watershed drains approximately one quarter of British Columbia (Cameron, 1996) with the Fraser River injecting large quantities of DOC, and consequently CDOM, into the waters of the SoG, similarly to other estuaries of the world (Blough *et al.*, 1993; Del Castillo *et al.*, 1999; Højerslev & Aarup, 2002). However, the sources of DOC are unclear, possibly being associated with logging (Cameron *et al.*, 1995) and not likely attributed to pulp mill effluents (Johannessen *et al.*, 2003). Furthermore, the higher concentrations of CDOM in April were probably due to the flushing of DOC out of soil early in the snowmelt (Hornberger *et al.*, 1994). It is possible that most of the allochthonous CDOM carried by the river in April around the beginning of the freshet was able to remain within OM1 and OM2, considering that the residence time of the plume is around one day and 10-40 days below the plume (Pawlowicz *et al.*, 2007). On the other hand, in July, when solar exposure was much higher and increased photobleaching more likely, lower concentrations of CDOM were measured. It would be hard to assess the nature of CDOM since photobleaching of almost all CDOM can occur within days depending on the incident radiation and depth (Vähätalo & Wetzel, 2004). As suggested by Vodacek *et al.* (1997) for Middle Atlantic Bight waters, lower concentrations of CDOM may also have resulted from the mixing of different water masses.

Despite the predominance of particulate scattering in all three optical water masses (except at short wavelengths), scattering in OM2 and OM3 was between one to two orders of magnitude lower than in OM1 (Figures 6 and 7), similar to results found in waters with lower TSM in the Baltic Sea (Babin *et al.*, 2003), Lake Michigan (Bergmann *et al.*, 2004), and the Rhode River estuary (Gallegos *et al.*, 2005). In OM2 and OM3, absorption and scattering made approximately equal contributions to attenuation at short wavelengths ($\lambda < 500$ nm), with absorption dominating attenuation in OM3 waters in April and July. This higher contribution of absorption to attenuation likely had two different origins: (1) increased concentrations of small diatoms commonly found in the

SoG in July (Harrison *et al.*, 1983; LeBlond, 1983) with decreased package effect and consequently more chl *a* available for photosynthesis (Geider & Osborne, 1987; Kirk, 1994); and (2) decomposition of phytoplankton in April, thus resulting in higher absorption by CDOM due to the breakage of phytoplankton cells as they die and sink (Johannessen *et al.*, 2008). The decay of phytoplankton after the spring bloom season would have increased the concentration of autochthonous CDOM, as verified by the larger contribution of CDOM absorption to total absorption in OM3. To support this, the low correlation between $f_C(z)$ and CDOM absorptions ($a_{c'}(z,411)$ and $a_{Cspec}(z,411)$) in April and July in OM3 (Table 4) contrasted with the high contribution of $a_{c'}(z,411)$ to total light attenuation. In other words, the low fluorescence response of CDOM at depth was most likely caused by the instrument's failure to measure autochthonous or photobleached CDOM. Furthermore, CDOM slopes in OM3 were steeper than in OM1 (Table 3) also suggesting that the CDOM in OM3 was chemically different from the CDOM in OM1 (Schofield *et al.*, 2004; Coble, 2007).

The high $a_{c'}(z,411)$ also suggests that in these deeper waters, CDOM was likely competing with phytoplankton for short wavelength radiation (Del Castillo *et al.*, 1999; Vähätalo *et al.*, 2005). Also, because primary production appears to exceed terrestrial discharge as a source of organic matter to the SoG (Johannessen *et al.*, 2003), one would expect the concentration of autochthonous CDOM to be higher than the concentration of terrigenous CDOM.

Classification of water masses according to their optical characteristics has been done typically with the use of radiometric quantities and AOPs (Aarup *et al.*, 1996a; Aarup *et al.*, 1996b; Højerslev *et al.*, 1996). This was mainly because of the wide availability of AOP sensors and the lack of optical sensors capable of measuring IOPs due to the complexity of their measurement. The use of IOPs in the classification of water masses is nevertheless more reliable because unlike the AOPs, the IOPs depend not on the ambient light distribution, but solely on the waters and on their contents (Preisendorfer, 1976; Mobley, 1994). The clustering of the IOPs and AOPs yielded results that were statistically significant. However, the performance of the IOPs in classifying the different OMs was more consistent with the biophysical and hydrographic characteristics of those waters. The clusters generated by the AOPs did not provide an accurate classification of the water masses into optical masses.

Nevertheless, the radiometric quantities and the AOPs were still useful in complementing the optical characterization of the water masses of the SoG. The profiles of radiance reflectance, $R_r(0\text{-},z,\lambda)$, were typical of estuarine/coastal waters. The attenuation of blue and red wavelengths was high, thus allowing for a high reflectance in the green wavelengths in all three OMs.

The diffuse attenuation coefficient, $K_{Ed}(z,\lambda)$, is used quite often in describing the characteristics of a water body, because it is a rate of light decrease with depth. Overall, $K_{Ed}(z,\lambda)$ was similar in magnitude to those observed in the Jerlov water types for all

OMs, from the most turbid OM1, with high $K_{Ed}(z,\lambda)$, to the clearest OM3, with the lowest $K_{Ed}(z,\lambda)$. $K_{Eo}(z,PAR)$ (Table 6) in April and July were similar to those reported by Stockner *et al.* (1979) and Harrison *et al.* (1991) in the waters of the SoG during winter-spring conditions with $K_{Eo}(z,PAR)$ values ranging from 0.11 m^{-1} to 2.90 m^{-1} and values decreasing away from the influence of the Fraser River. The average cosines were quite low in OM1 (Table 7) because of the high diffuse scalar irradiances, $E_o(0\text{-},z,\lambda)$, increasing toward OM3, where $E_o(0\text{-},z,\lambda)$ was lowest. Green wavelengths, represented by $E_o(0\text{-},z,530)$, were the only wavelengths below 20 m with $E_o(0\text{-},z,530)/E_o(0+,530)$ above 10% due to the high absorption of blue wavelengths by CDOM and chl *a* and high absorption of red wavelengths by chl *a*.

4.2 Light Availability for Primary Productivity

The photosynthetic activity of phytoplankton is confined to a thin layer of the upper oceans, because these organisms depend on the availability of light (Nybakken, 1988). However, the minimum light availability requirements of phytoplankton species for photosynthesis vary among species, i.e. photosynthesis only occurs when light reaching the phytoplankton is above a certain intensity. This minimum light intensity is known as the compensation irradiance ($E_c(z,PAR)$) and the depth at which photosynthetic oxygen liberation equals oxygen consumption due to respiration is called the irradiance compensation depth Z_c (Kirk, 1994). Z_c can be calculated from

$$Z_c = \frac{\ln E_o(0-,z,PAR) - \ln E_c(0-,z,PAR)}{\overline{K}_{Eo}(z,PAR)} \tag{43}$$

where $\overline{K}_{Eo}(z,PAR)$ is the mean scalar irradiance attenuation coefficient for PAR. $K_{Eo}(z,PAR)$ was obtained similarly to any of the other *K*-functions (Equations 19 and 20), $E_o(0\text{-},z,PAR)$ was modelled by Hydrolight, and $E_c(0\text{-},z,PAR)$ was obtained from Jitts *et al.* (1964).

More than 200 diatom species are found in SoG waters (Harrison *et al.*, 1983) and two of the most abundant ones in the spring and summer, *Thalassiosira nordenskiöldii* and *Skeletonema costatum*, are able to photosynthesize at extremely low levels of irradiance within the range of temperatures found in SoG waters. $E_c(0\text{-},z,PAR)$ for *T. nordenskiöldii* and *S. costatum* are 14 μE m^{-2} s^{-1} (or 3.5 W m^{-2}) and 8 μE m^{-2} s^{-1} (or 2 W m^{-2}), respectively (Jitts *et al.*, 1964).

$Z_{1\%}$ is widely regarded as the lowest limit for photosynthesis (Raymont, 1980; Kirk, 1994). However, this was not always the case for SoG waters. *In situ* $Z_{1\%}$ was statistically similar in April to Z_c for *T. nordenskiöldii* but not for *S. costatum* (Tables 9 and 10). *S. costatum* had the potential to significantly photosynthesize below the measured $Z_{1\%}$ (82% of Z_c observations were below modelled Z_c in comparison to 55% of Z_c values for *T. nordenskiöldii*) thus indicating that $E_o(Z_{1\%}, PAR)$ values should be above $E_c(Z_{1\%}, PAR)$, which was true for *S. costatum* at 82% of the stations and 55% of the stations for *T. nordenskiöldii*. In July, Z_c for both species was statistically different from $Z_{1\%}$ with 68% and 84% of Z_c values below $Z_{1\%}$ for *T. nordenskiöldii* and *S. costatum*, respectively. 63% of all stations in July presented $E_o(Z_{1\%}, PAR)$ above $E_c(Z_{1\%}, PAR)$ for *T. nordenskiöldii* and 95% for *S. costatum*.

Table 9 - Modelled and *in situ* radiometric quantities and AOPs. Modelled critical depths, Z_c, highlighted in gray were below *in situ* $Z_{1\%}$.

	Station	Modelled $E_o(0+,PAR)$ (μE m^{-2}s^{-1})	*In situ* $E_s(0+,PAR)$ (μE m^{-2}s^{-1})	Modelled $K_{Eo}(z,PAR)$ (mean) (m^{-1})	Modelled $K_{Ed}(z,PAR)$ (mean) (m^{-1})	*In situ* $Z_{1\%}$ (m)	Modelled $E_o(Z_{1\%},PAR)$ (μE m^{-2}s^{-1})	Modelled $E_d(Z_{1\%},PAR)$ (μE m^{-2}s^{-1})	*in situ* $E_d(Z_{1\%},PAR)$ (μE m^{-2}s^{-1})	*Ratio* $\frac{E_o(Z_{1\%},PAR)}{E_o(0+,PAR)}$	Z_c *T. nordenskiöldii* (m)	Z_c *S. costatum* (m)
Apr	S1-1	2579.29	1233.47	0.361	0.356	14	26.44	20.1	8.1	0.010	14.44934	15.99952
	S1	2758.51	1621.1	0.288	0.288	14	25.8	15.4	3.83	0.009	18.3451	20.28821
	S2-1	401.65	396.65	0.169	0.169	22	4.5	3.94	2.5	0.011	19.86109	23.17242
	S2-2	992.44	545.69	0.240	0.245	18	10.5	9.7	1.9	0.011	17.75462	20.08635
	S2-3	1034.46	504.26	0.998	0.963	6	10.01	7.3	0.3	0.010	4.3112	4.871937
	S3	717.82	465.08	0.181	0.182	21	7.16	5.7	3.08	0.010	21.75227	24.84407
	S3-1	924.19	428.08	0.260	0.256	14	10.23	7.84	2.37	0.011	16.11485	18.26722
	S3-2	1135.6	572.84	0.658	0.653	8	13.3	9.9	1.2	0.012	6.680637	7.531117
	S4-1	1813.64	953.38	0.221	0.220	16	19.7	15.12	4.5	0.011	22.0092	24.5414
	S4-2	2167.32	1115.7	0.337	0.338	12	21.3	16.7	4.9	0.010	14.96199	16.62257
	S4-3	2413.22	1015.45	0.478	0.491	11	25.3	18.7	4.5	0.010	10.77335	11.94409
Jul	S1-1	991.43	481.1	0.306	0.308	12	9.19	7.01	6.89	0.009	13.92187	15.75068
	S1-2	763.96	402.21	0.254	0.253	14	8.1	6.45	6.03	0.011	15.7459	17.94911
	S1	792.83	416.64	0.232	0.232	18	8.02	6.28	5.78	0.010	17.39893	19.81107
	S2-1	374.79	161.37	0.286	0.291	16	3.62	2.63	1.44	0.010	11.49409	13.45078
	S2-2	1029.63	488.54	0.400	0.400	12	10.9	8.14	3.5	0.011	10.74474	12.14378
	S2-3	2235.79	1110.2	1.957	1.900	4	16.7	9.17	1.85	0.007	2.592383	2.878338
	S3	1912.9	1107.06	0.358	0.333	9	20.2	14.5	10.76	0.011	13.73553	15.2987
	S3-1	1197.63	591.88	0.563	0.565	9	12.1	9.25	3.73	0.010	7.902385	8.896374
	S3-2	1518.99	690.59	0.648	0.618	8	13.5	10.4	4.5	0.009	7.232629	8.096234
	S3-3	1887.15	963.12	0.393	0.388	11	17.6	13.9	8.58	0.009	12.47778	13.90173
	S4-1	2848.42	1893.86	0.211	0.213	23	27.4	23.1	13.19	0.010	25.19176	27.84397
	S4-2	2748.51	1581.76	0.412	0.415	12	23.4	20.6	13.2	0.009	12.81494	14.17323
	S4-3	1622.14	988.44	0.473	0.475	9	17.1	11.6	4.57	0.011	10.04745	11.23057
	S5	3077.13	1838.95	0.381	0.387	12	30.1	23.6	14.19	0.010	14.15406	15.62286
	S5-1	2824.89	1843.5	0.264	0.268	15	29.1	23.5	17.64	0.010	20.10291	22.22266
	S5-2	2546.08	1303.71	0.442	0.441	10	23	18.2	10.03	0.009	11.77207	13.03816
	S6	2827.66	1916.74	0.255	0.257	17	27.9	22.9	16.19	0.010	20.81626	23.01084
	S6-1	2800.07	1658.27	0.237	0.237	20	27	21.4	10.5	0.010	22.35587	24.71712
	S6-2	2822.29	789.62	0.283	0.279	12	27.1	20	17.94	0.010	18.74999	20.72743

Table 10 - Paired t-test was used to check for differences between results from Table 9. All results were significant at a 95% confidence level.

Paired t-test at 95% Confidence Interval	April (n = 11)	July (n = 19)
Modelled $Z_{1\%}$ - *in situ* $Z_{1\%}$	Different (p = 0.000)	Not different (p = 0.674)
Modelled $Z_{1\%}$ - Z_c *T. nordenskiöldii*	Not different (p = 0.229)	Different (p = 0.036)
Modelled $Z_{1\%}$ - Z_c *S. costatum*	Different (p = 0.008)	Different (p = 0.000)
Modelled $E_d(Z_{1\%},PAR)$ - *in situ* $E_d(Z_{1\%},PAR)$	Different (p = 0.000)	Different (p = 0.000)
Modelled $K_{Eo}(z,PAR)$ – modelled $K_{Ed}(z,PAR)$	Not different (p = 0.463)	Not different (p = 0.183)
Modelled $E_o(Z_{1\%},PAR)$ - $E_c(z,PAR)$ *Thal*	Not different (p = 0.467)	Different (p = 0.031)
Modelled $E_o(Z_{1\%},PAR)$ - $E_c(z,PAR)$ - *Skel*	Different (p = 0.009)	Different (p = 0.000)

Reasons for some differences between $Z_{1\%}$ and Z_c can be related to the method used to obtain them. *In situ* $Z_{1\%}$ was calculated based on the ratio of $E_d(0\text{-},z,\lambda)$ and $E_s(0+,\lambda)$ whereas modelled $Z_{1\%}$ was derived from the ratio of $E_o(0\text{-},z,PAR)$ and $E_o(0+,PAR)$. As seen in Table 10, there were statistically significant differences between these variables in April. Because $E_o(0\text{-},z,PAR)$ best describes the light field in terms of primary productivity (Bergmann *et al.*, 2004), the modelled $Z_{1\%}$ was used in this analysis instead of its *in situ* counterpart. $K_{Eo}(z,PAR)$ and $K_{Ed}(z,PAR)$ were statistically identical (Table 9).

In principle, the physiology and community composition of these two phytoplankton species was not notably limited by the availability of light within the euphotic zone of the waters of the SoG according to modelled data except for a few stations (highlighted Z_c values in Table 9). Surprisingly, though stations S2-3 and S3-2 were the closest stations to the Fraser River mouths, had the highest surface TSM concentrations and highest IOPs, the modelled $E_o(Z_{1\%},PAR)$ was higher than $E_c(z,PAR)$in July. *In situ* $E_d(0\text{-},z,PAR)$ values were lower than modelled $E_d(0\text{-},z,PAR)$ probably because of the nature of data acquisition in the water column. This may have been due to Satlantic's free-falling HyperPRO profiler not always being level with the ocean surface; thus the $E_d(0\text{-},z,\lambda)$ and $L_u(0\text{-},z,\lambda)$ sensors were tilted in relation to the surface due to currents, wave action, and ship movement. At certain stations it was not possible to obtain measurements without tilt angles below the manufacturer-recommended 5° angle (SATLANTIC, 2004).

The fact that the highest concentrations of chl *a* were found in OM2 was probably related to light shading in OM1. Photoinhibition in OM2 might also explain why the highest chl *a* concentrations were not at surface. This phenomenon occurs when phytoplankton are exposed to irradiances above the point at which they become light-saturated, and it is followed by a decrease in primary productivity (Parsons *et al.*, 1984). Figure 28 clearly shows the effect of photoinhibition in April and July. The highest chl *a* concentrations were found at lower $E_o(0\text{-},z,PAR)$ between 3 m and 5 m and not at surface, similar to Tully *et al*. (1957). Thus high $E_o(0\text{-},z,PAR)$ at surface inhibited photosynthesis forcing the phytoplankton to adapt to lower depths where they could reach an optimum irradiance level suitable for maximum photosynthesis.

Just as different species have different irradiance compensation depths, they also have different irradiance optima (Raymont, 1980), which can be represented by the irradiance saturation parameter $E_k(0\text{-},z,PAR)$ (Kirk, 1994), also known as the photoacclimation parameter (Bergmann *et al.*, 2004). For the two example phytoplankton species presented here, Jitts *et al.* (1964) reported irradiance optima of around 208 μE m^{-2} s^{-1} (52 W m^{-2}) for *T. nordenskiöldii* and 700 μE m^{-2} s^{-1} (175 W m^{-2}) for *S. costatum*. In general, low chl *a* concentrations were associated with $E_o(0\text{-},z,PAR)$ above the optimum for *T. nordenskiöldii* (Figure 29), whereas higher chl *a* concentrations were usually associated with lower irradiances and below 3 m. However, these optimum values do fluctuate depending on the water temperature. For the range of SoG water temperatures found in April and July, optimum growth conditions would be around 56-420 μE m^{-2} s^{-1} (14-105 W m^{-2}) for *T. nordenskiöldii* and 208-1116 μE m^{-2} s^{-1} (52-279 W m^{-2}) for *S. costatum*, which fall within the ranges of $E_o(0\text{-},z,PAR)$ found in OM2 (Table 6). Curiously, a minimum winter value of $E_o(0+,PAR)$ of around 280 μE m^{-2} s^{-1} (70 W m^{-2}) reported by Harrison *et al.* (1983) seems to indicate that winter $E_o(0\text{-},z,PAR)$ could potentially support photosynthesis of *T. nordenskiöldii* and *S. costatum*.

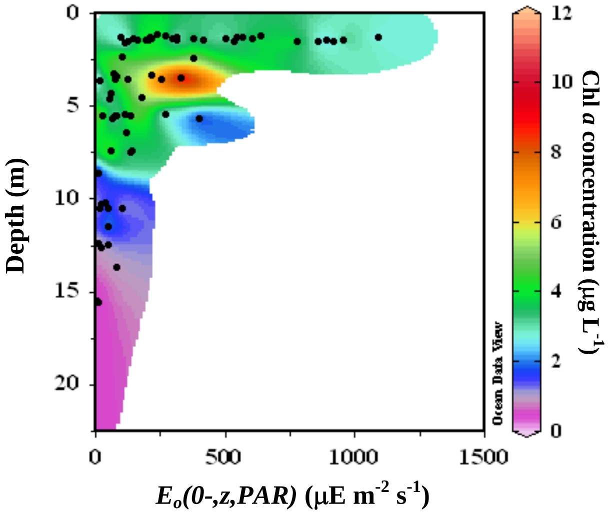

Figure 28 – Modelled downwelling scalar irradiances and chl *a* concentrations in April and July. The highest chl *a* concentrations occurred between 2.5 m and 5 m.

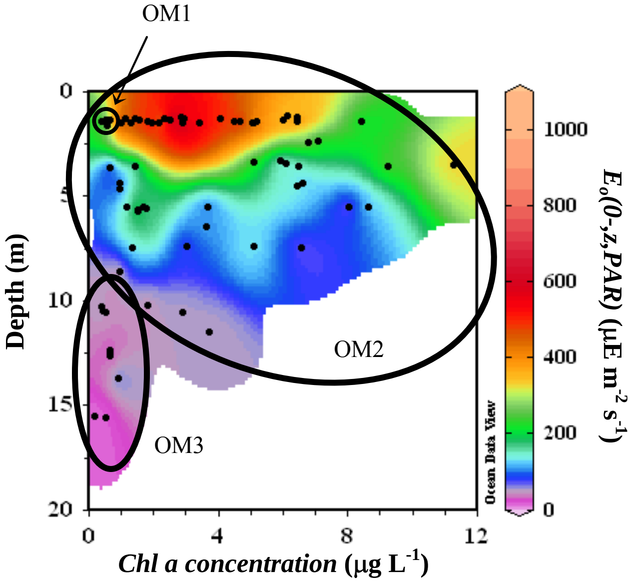

Figure 29 - Different perspective on chl *a* concentrations and modelled downwelling scalar irradiances and in April and July. High chl *a* concentrations usually occurred at lower irradiances below 2.5 m in OM2. Chl *a* concentrations in OM1 and OM3 were the lowest.

The presence of phytoplankton in OM3 waters was understandably much lower because of the lower levels of downwelling irradiance at greater depths (Figure 30) ($E_o(0\text{-},z,PAR)$ was around 62 μE m^{-2} s^{-1} in April and 29 μE m^{-2} s^{-1} in July (Table 6). Ratios of $E_o(0\text{-},z,\lambda)$ to $E_o(0+,z,\lambda)$ also indicated, with the exception of green wavelengths, that light below 5 m was already below the 1% level (Figure 26). Furthermore, an increase in chl *a* concentrations was accompanied by a decrease in scattering and backscattering (Figure 31), which in turn indicated fewer inorganic particles and the possible presence of organic particles of low index of refraction, such as flagellates and cyanophytes (Chang *et al.*, 2006), mostly in OM2. Flagellates thrive in the summer months in the SoG (Harrison *et al.*, 1983). The high chl *a* concentration and an increase in scattering (and backscattering), however, could possibly indicate the presence of phytoplankton of high index of refraction, such as diatoms in OM1 and OM2 (Twardowski *et al.*, 2001; Boss *et al.*, 2004).

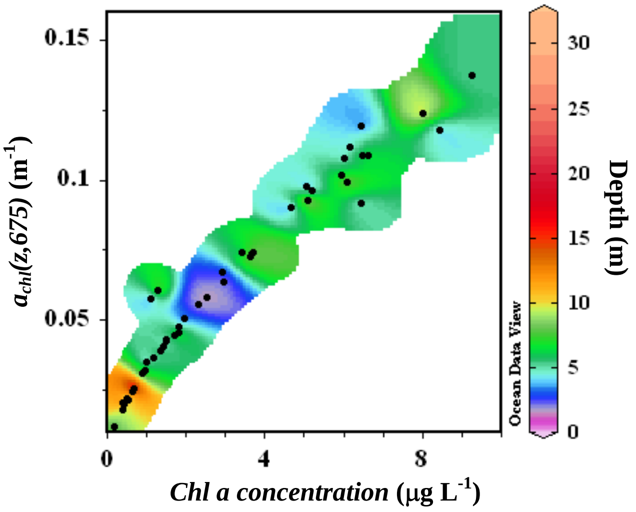

Figure 30 - Relationship between chl *a* concentrations and modelled chl a absorption at 675 nm with depth in July.

The light field available to phytoplankton showed a spectral shift toward the green wavelengths with depth. This greening of the water column would probably affect the composition of the phytoplankton species in SoG waters, with the exception of station S2-3, for which red wavelengths ($E_o(0\text{-},z,650)$) were predominant. Diatoms absorb radiation primarily in the blue and red wavelengths due to chl *a* and fucoxanthin. Unlike diatoms, cryptophytes (e.g. *Rhodomonas minuta*), rhodophytes, and cyanophytes, which occur in the SoG (Harrison *et al.*, 1983), would be the main phytoplankton groups to take advantage of this green shift in the SoG because their primary photosynthetic pigments (phycoerythrins) have maximum absorption in the green wavelengths (Rowan, 1989; Kirk, 1994).

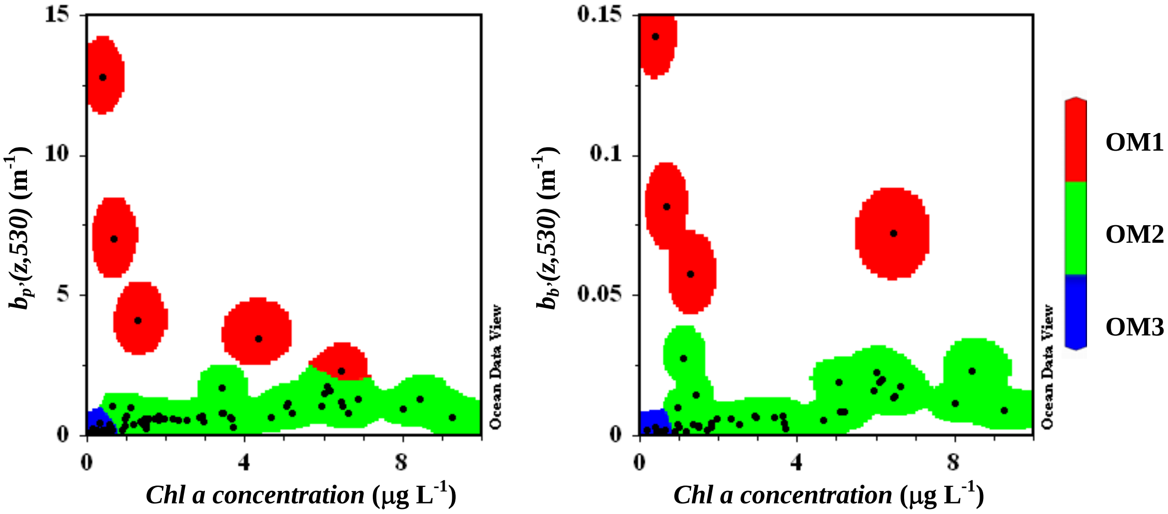

Figure 31 - Relationships between chl *a* concentrations and (a) particulate scattering coefficient at 530 nm and (b) modelled particulate backscattering coefficient in July for all three optical water masses.

Chapter 5: Conclusion

The goal of this dissertation was to combine the IOPs, AOPs, radiometric quantities, and optical constituents of the waters of the SoG in order to provide a quantitative analysis of their horizontal and vertical variabilities within $Z_{1\%}$. The importance of this research lies on it being the first to employ hyperspectral optical data and to examine all these different components together for the SoG. As such, the data and analysis presented in this research provide the most complete baseline optical information available for the waters of the SoG.

The euphotic zone of the Strait of Georgia was divided into three distinct optically-defined water masses: river plume water (OM1), estuarine plume waters (OM2), and deeper/northern waters (OM3). OM1 waters were characterized by high and spectrally-invariant particulate scattering. Particulate matter also dominated total absorption in OM1. The highest particulate scattering (around 16 m^{-1} at 650 nm) was likely due to high loads of fine inorganic particles in the water. CDOM played a minimal role on the total absorption in this zone. In OM2, unlike OM1, absorption and scattering showed spectral dependence. At short wavelengths, absorption and scattering were equally important to total attenuation, whereas scattering became predominant at longer wavelengths. In OM2 waters, absorption was equally influenced by CDOM and particles. In OM3, the contributions of absorption and scattering to attenuation were also spectrally dependent, with absorption dominating attenuation at short wavelengths. CDOM dominated total absorption, while the relatively low concentration of particles in this zone resulted in relatively lower scattering (about 0.9 m^{-1} at 650 nm). Absorption by CDOM in OM3 strongly contributed to the attenuation of light, with possibly autochthonous CDOM dominating absorption at the short wavelengths.

The three OMs had quite distinct reflectance profiles that together with the IOP characterized the waters of the SoG well. Reflectance was highest in OM1 with a distinctive peak at the green wavelengths. OM2 and OM3 presented far lower reflectances however retaining the green peak. The fluorescence peak around 685 nm was visible in most reflectance profiles of all OMs except for OM1 and OM3 in July at stations close to the mouth of the Fraser River.

The optical water masses could also be classified according to the optical classes developed by Jerlov (1976) by using their $K_{Ed}(z,\lambda)$ values. OM1 waters were more turbid than Jerlov's highest optical class due to the high concentrations of TSM and CDOM. $K_{Ed}(z,\lambda)$ decreased with depth according to the decreasing concentrations of the water optical constituents. OM3 waters were the clearest waters of all three optical water masses.

IOP data are valuable in coastal waters, as absorption and scattering can influence primary productivity. Changes in the IOPs of coastal waters occur at relatively small spatial and temporal scales, and can be easily affected by inland processes. For instance, changes in the climate may have an impact on the seasonal discharge of the Fraser River (Whitfield *et al.*, 2003), which is dependent on the snowpack and on the rainfall in the Fraser River watershed. Morrison *et al.* (2002) showed through modelling that by the end of the 21st century, the flow of the Fraser River would decrease by 18% and the freshet would occur, on average, 24 days earlier in the year when compared to current data. Consequently, changes in the magnitude and timing of the riverine discharge would possibly lead to changes in TSM and CDOM concentrations and compositions in the waters of the SoG, affecting the quantity and quality of light available for primary productivity. Thus, changes in the location and thickness of the optical water masses would ensue.

5.1 Concluding Remarks

The results presented here demonstrated that visible light was attenuated differently in the three optical water masses of the euphotic zone of the SoG, thus suggesting that the availability of visible light above $Z_{1\%}$, which is important to photosynthesis, was influenced by inorganic particulate scattering and CDOM absorption in different parts of the Strait. However, the *in situ* and modelled data showed that particles and CDOM had a minimal effect on light attenuation within OM1 and OM2. Thus, phytoplankton cells were not light-limited and had enough light available for photosynthesis in spring and summer in the euphotic waters of the SoG. While the magnitude of irradiance was not a concern, the spectral quality of the available irradiance could play a significant role in the composition of phytoplankton communities. The predominance of green-red wavelengths could increase the presence of phytoplankton groups other than diatoms. Regardless, diatom species such as *T. nordenskiöldii* and *S. costatum* will likely be present in the waters of the SoG throughout the year because of their ability to take advantage of very low irradiances for photosynthesis within the euphotic zone.

As the first baseline optical study for this region, this research was still limited to typical conditions of spring and summer. A more complete optical characterization of the waters of the SoG, and therefore a better understanding of light availability for primary productivity, would require *in situ* data for the fall and winter conditions as well for several years and in the northern and southern regions of the SoG. Nevertheless, the methods employed here may be extrapolated to other coastal seas influenced by large riverine systems.

Bibliography

Aarup, T.; Holt, N.; Højerslev, N.K. 1996a. Optical measurements in the North Sea-Baltic Sea transition zone. 2. Water mass classification along the Jutland west coast from salinity and spectral irradiance measurements. *Continental Shelf Research*, **16**(10): 1343-1353.

Aarup, T.; Holt, N.; Højerslev, N.K. 1996b. Optical measurements in the North Sea-Baltic Sea transition zone. 3. Statistical analysis of bio-optical data from the Eastern North Sea, the Skagerrak and the Kattegat. *Continental Shelf Research*, **16**(10): 1355-1377.

Allen, S. and Harris, S. 2004. *The Timing of the Spring Bloom in the Strait of Georgia: The Roles of Photo-Inhibition and of Wind Mixing*. 51st Eastern Pacific Ocean Conference, 2004. Sidney, BC. http://www-sci.pac.dfo-mpo.gc.ca/sci/EPOC2004/abstracts_e.htm.

Arar, E.J. 1997. *Method 447.0. Determination of Chlorophylls a and b and Identification of Other Pigments of Interest in Marine and Freshwater Algae Using High Performance Liquid Chromatography with Visible Wavelength Detection.* National Exposure Laboratory, U.S. Environmental Protection Agency, Cincinatti, Ohio. 20 p.

Arst, H. 2003. *Optical properties and remote sensing of multicomponental water bodies*. Springer Verlag, Berlin. 231 p.

Arst, H.; Erm, A.; Herlevi, A.; Kutser, T.; Lepparanta, M.; Reinart, A.; Virta, J. 2008. Optical properties of boreal lake waters in Finland and Estonia. *Boreal Environment Research*, **13**(2): 133-158.

Babin, M.; Morel, A.; Fournier-Sicre, V.; Fell, F.; Stramski, D. 2003. Light scattering properties of marine particles in coastal and open ocean waters as related to the particle mass concentration. *Limnology and Oceanography*, **48**(2): 843-859.

Baker, A. and Spencer, R.G.M. 2004. Characterization of dissolved organic matter from source to sea using fluorescence and absorbance spectroscopy. *Science of The Total Environment*, **333**(1-3): 217-232.

Barocio-León, O.A.; Millán-Núñez, R.; Santamaría-del-Ángel, E.; González-Silvera, A.; Trees, C.C.; Orellana-Cepeda, E. 2008. Bio-optical characteristics of a phytoplankton bloom event off Baja California Peninsula (30-31 degrees N). *Continental Shelf Research*, **28**(4-5): 672-681.

Barrie, J.V. and Currie, R.G. 2000. Human impact on the sedimentary regime of the Fraser River Delta, Canada. *Journal of Coastal Research*, **16**(3): 747-755.

Bergmann, T.; Fahnenstiel, G.; Lohrenz, S.; Millie, D.; Schofield, O. 2004. Impacts of a recurrent resuspension event and variable phytoplankton community composition on remote sensing reflectance. *Journal of Geophysical Research-Oceans*, **109**(C10S15): doi:10.1029/2002JC001575.

Binding, C.E.; Bowers, D.G.; Mitchelson-Jacob, E.G. 2003. An algorithm for the retrieval of suspended sediment concentrations in the Irish Sea from SeaWiFS ocean colour satellite imagery. *International Journal of Remote Sensing*, **24**(19): 3791-3806.

Bissett, W.P.; Schofield, O.; Cullen, J.J.; Miller, W.L.; Pluedemann, A.J.; Mobley, C.D. 2001. Resolving the Impacts and Feedback of Ocean Optics on Upper Ocean Ecology. *Oceanography*, **14**(3): 30-53.

Blondeau-Patissier, D.; Tilstone, G.H.; Martinez-Vicente, V.; Moore, G.F. 2004. Comparison of bio-physical marine products from SeaWiFS, MODIS and a bio-optical model with *in situ* measurements from Northern European waters. *Journal of Optics A: Pure and Applied Optics*, **6**(9): 875-889.

Blough, N.V. and Del Vecchio, R. 2002. Chromophoric DOM in the Coastal Environment. **In**: Hansell, D. A.and Carlson, C. A. (Ed.). *Biogeochemistry of Marine Dissolved Organic Matter,* Academic Press, San Diego. p. 509-546.

Blough, N.V.; Zafiriou, O.C.; Bonilla, J. 1993. Optical Absorption Spectra of Waters from the Orinoco River Outflow - Terrestrial Input of Colored Organic Matter to the Caribbean. *Journal of Geophysical Research-Oceans*, **98**(C2): 2271-2278.

Boss, E.; Pegau, W.S.; Lee, M.; Twardowski, M.; Shybanov, E.; Korotaev, G.; Baratange, F. 2004. Particulate backscattering ratio at LEO 15 and its use to study particle composition and distribution. *Journal of Geophysical Research-Oceans*, **109**(C1): doi: 10.1029/2002JC001514

Bowers, D.G. and Binding, C.E. 2006. The optical properties of mineral suspended particles: A review and synthesis. *Estuarine, Coastal and Shelf Science*, **67**(1-2): 219-230.

Bricaud, A.; Morel, A.; Prieur, L. 1981. Absorption by Dissolved Organic Matter of the Sea (Yellow Substance) in the UV and Visible Domains. *Limnology and Oceanography*, **26**(1): 43-53.

Cameron, E.M. 1996. Hydrogeochemistry of the Fraser River, British Columbia: Seasonal Variation in Major and Minor Components. *Journal of Hydrology*, **182**(1-4): 209-225.

Cameron, E.M.; Hall, G.E.M.; Veizer, J.; Krouse, H.R. 1995. Isotopic and Elemental Hydrogeochemistry of a Major River System - Fraser River, British Columbia, Canada. *Chemical Geology*, **122**(1-4): 149-169.

Carder, K.L.; Steward, R.G.; Chen, R.F.; Hawes, S.; Lee, Z.; Davis, C.O. 1993. AVIRIS Calibration and Application in Coastal Oceanic Environments - Tracers of Soluble and Particulate Constituents of the Tampa Bay Coastal Plume. *Photogrammetric Engineering and Remote Sensing*, **59**(3): 339-344.

Chang, G.C.; Barnard, A.H.; McLean, S.; Egli, P.J.; Moore, C.; Zaneveld, J.R.V.; Dickey, T.D.; Hanson, A. 2006. *In situ* optical variability and relationships in the Santa Barbara Channel: implications for remote sensing. *Applied Optics*, **45**(15): 3593-3604.

Chang, G.C.; Dickey, T.D.; Schofield, O.M.; Weidemann, A.D.; Boss, E.; Pegau, W.S.; Moline, M.A.; Glenn, S.M. 2002. Nearshore physical processes and bio-optical properties in the New York Bight. *Journal of Geophysical Research-Oceans*, **107**(C9): 3133, doi:10.1029/2001JC001018.

Chen, R.F.; Bissett, P.; Coble, P.; Conmy, R.; Gardner, G.B.; Moran, M.A.; Wang, X.C.; Wells, M.L.; Whelan, P.; Zepp, R.G. 2004. Chromophoric dissolved organic matter (CDOM) source characterization in the Louisiana Bight. *Marine Chemistry*, **89**(1-4): 257-272.

Chen, R.F. and Gardner, G.B. 2004. High-resolution measurements of chromophoric dissolved organic matter in the Mississippi and Atchafalaya River plume regions. *Marine Chemistry*, **89**(1-4): 103-125.

Clesceri, L.S.; Greenberg, A.E.; Eaton, A.D. 1998. 2540 D. Total Suspended Solids Dried at 103-105°C. **In**: Clesceri, L. S.; Greenberg, A. E.; Eaton, A. D. (Ed.). *Standard Methods for the Examination of Water and Wastewater,* American Public Health Association, Washington, D.C. p. 2-57 - 2-58.

Cleveland, J.S. 1995. Regional Models for Phytoplankton Absorption as a Function of Chlorophyll-a Concentration. *Journal of Geophysical Research-Oceans*, **100**(C7): 13333-13344.

Cloern, J.E. 1987. Turbidity as a Control on Phytoplankton Biomass and Productivity in Estuaries. *Continental Shelf Research*, **7**(11-12): 1367-1381.

Coble, P.; Hu, C.; Gould, R.W.; Chang, G.; Wood, A.M. 2004. Colored Dissolved Organic Matter in the Coastal Ocean: An Optical Tool for Coastal Zone Environmental Assessment and Management. *Oceanography*, **17**(2): 50-59.

Coble, P.G. 1996. Characterization of marine and terrestrial DOM in seawater using excitation emission matrix spectroscopy. *Marine Chemistry*, **51**(4): 325-346.

Coble, P.G. 2007. Marine Optical Biogeochemistry: The Chemistry of Ocean Color. *Chemical Reviews*, **107**(2): 402-418.

Cohen, J.E.; Small, C.; Mellinger, A.; Gallup, J.; Sachs; Jeffrey; Vitousek, P.M.; Mooney; A., H. 1997. Estimates of Coastal Populations. *Science*, **278**(5341): 1209c-1213,10.1126/science.278.5341.1209c.

Collins, A.K. 2005. *A 1D Ocean Mixing Model of the Strait of Georgia. Ecological Responses to Physical Forcing*. M.Sc. Thesis. University of British Columbia. Vancouver, BC. 144 p.

Conmy, R.N.; Coble, P.G.; Chen, R.F.; Gardner, G.B. 2004. Optical properties of colored dissolved organic matter in the Northern Gulf of Mexico. *Marine Chemistry*, **89**(1-4): 127-144.

Cullen, J.J.; Ciotti, A.M.; Davis, R.F.; Lewis, M.R. 1997. Optical detection and assessment of algal blooms. *Limnology and Oceanography*, **42**(5): 1223-1239.

Del Castillo, C.E.; Coble, P.G.; Morell, J.M.; Lopez, J.M.; Corredor, J.E. 1999. Analysis of the optical properties of the Orinoco River plume by absorption and fluorescence spectroscopy. *Marine Chemistry*, **66**(1-2): 35-51.

Del Castillo, C.E.; Gilbes, F.; Coble, P.G.; Muller-Karger, F.E. 2000. On the dispersal of riverine colored dissolved organic matter over the West Florida Shelf. *Limnology and Oceanography*, **45**(6): 1425-1432.

Dickey, T.; Lewis, M.; Chang, G. 2006. Optical oceanography: Recent advances and future directions using global remote sensing and in situ observations. *Reviews of Geophysics*, **44**(RG1001): doi:10.1029/2003RG000148.

Dickey, T.D. 1991. The Emergence of Concurrent High-Resolution Physical and Biooptical Measurements in the Upper Ocean and Their Applications. *Reviews of Geophysics*, **29**(3): 383-413.

Dickey, T.D. 2002. A Vision of Oceanographic Instrumentation and Technologies in the Early Twenty-First Century. **In**: Hempel, G.; Summerhayes, C. P.; Field, J. G. (Ed.). *Oceans 2020 : Science, Trends, and the Challenge of Sustainability,* Island Press, Washington D.C. p. 209-254.

Dickey, T.D. 2003. Emerging ocean observations for interdisciplinary data assimilation systems. *Journal of Marine Systems*, **40**: 5-48.

Doxaran, D.; Cherukuru, N.; Lavender, S.J. 2006. Apparent and inherent optical properties of turbid estuarine waters: measurements, empirical quantification relationships, and modeling. *Applied Optics*, **45**(10): 2310-2324.

Edmond, J.M.; Boyle, E.A.; Grant, B.; Stallard, R.F. 1981. The chemical mass balance in the Amazon plume I: The nutrients. *Deep Sea Research Part A. Oceanographic Research Papers*, **28**(11): 1339-1374.

Environment Canada 2006. *Fraser River at Hope (08MF005).* http://scitech.pyr.ec.gc.ca/waterweb.

Frette, O.; Stamnes, J.J.; Stamnes, K. 1998. Optical remote sensing of marine constituents in coastal waters: a feasibility study. *Applied Optics*, **37**(36): 8318-8326.

Gallegos, C.L. 2005. Optical water quality of a blackwater river estuary: the Lower St. Johns River, Florida, USA. *Estuarine, Coastal and Shelf Science*, **63**(1-2): 57-72.

Gallegos, C.L.; Jordan, T.E.; Hines, A.H.; Weller, D.E. 2005. Temporal variability of optical properties in a shallow, eutrophic estuary: Seasonal and interannual variability. *Estuarine, Coastal and Shelf Science*, **64**(2-3): 156-170.

Gallegos, C.L. and Neale, P.J. 2002. Partitioning spectral absorption in case 2 waters: discrimination of dissolved and particulate components. *Applied Optics*, **41**(21): 4220-4233.

Gallie, E.A. and Murtha, P.A. 1992. Specific Absorption and Backscattering Spectra for Suspended Minerals and Chlorophyll-a in Chilko Lake, British Columbia. *Remote Sensing of Environment*, **39**(2): 103-118.

Geider, R.J. and Osborne, B.A. 1987. Light Absorption by a Marine Diatom - Experimental Observations and Theoretical Calculations of the Package Effect in a Small *Thalassiosira* Species. *Marine Biology*, **96**(2): 299-308.

Griffin, D.W. and Kellogg, C.A. 2004. Dust Storms and Their Impact on Ocean and Human Health: Dust in Earth's Atmosphere. *EcoHealth*, **1**(3): 284-295.

Guéguen, C.; Guo, L.D.; Tanaka, N. 2005. Distributions and characteristics of colored dissolved organic matter in the Western Arctic Ocean. *Continental Shelf Research*, **25**(10): 1195-1207.

Harrison, P.J.; Clifford, P.J.; Cochlan, W.P.; Yin, K.; St. John, M.A.; Thompson, P.A.; Sibbald, M.J.; Albright, L.J. 1991. Nutrient and Plankton Dynamics in the Fraser River Plume, Strait of Georgia, British Columbia. *Marine Ecology Progress Series*, **70**(3): 291-304.

Harrison, P.J.; Fulton, J.D.; Taylor, F.J.R.; Parsons, T.R. 1983. Review of the Biological Oceanography of the Strait of Georgia - Pelagic Environment. *Canadian Journal of Fisheries and Aquatic Sciences*, **40**(7): 1064-1094.

Hobson, L.A. and McQuoid, M.R. 1997. Temporal variations among planktonic diatom assemblages in a turbulent environment of the southern Strait of Georgia, British Columbia, Canada. *Marine Ecology Progress Series*, **150**(1-3): 263-274.

Højerslev, N.K. and Aarup, T. 2002. Optical measurements on the Louisiana Shelf off the Mississippi River. *Estuarine, Coastal and Shelf Science*, **55**(4): 599-611.

Højerslev, N.K.; Holt, N.; Aarup, T. 1996. Optical measurements in the North Sea-Baltic Sea transition zone. 1. On the origin of the deep water in the Kattegat. *Continental Shelf Research*, **16**(10): 1329-1342.

Hooker, S.B.; Zibordi, G.; Berthon, J.F.; Brown, J.W. 2004. Above-water radiometry in shallow coastal waters. *Applied Optics*, **43**(21): 4254-4268.

Hornberger, G.M.; Bencala, K.E.; McKnight, D.M. 1994. Hydrological Controls on Dissolved Organic-Carbon During Snowmelt in the Snake River near Montezuma, Colorado. *Biogeochemistry*, **25**(3): 147-165.

Howard-Williams, C.; Davies-Colley, R.; Vincent, W.F. 1995. Optical properties of the coastal and oceanic waters off South Island, New Zealand: Regional variation. *New Zealand Journal of Marine and Freshwater Research*, **29**(4): 589-602.

Jerlov, N.G. 1976. *Marine Optics*. Elsevier Scientific Pub. Co., New York, NY. 231 p.

Jitts, H.R.; McAllister, C.D.; Stephens, K.V.; Strickland, J.D.H. 1964. The Cell Division Rates of Some Marine Phytoplankters as a Function of Light and Temperature. *Journal of the Fisheries Research Board of Canada*, **21**(1): 139-157.

Johannessen, S.C.; Macdonald, R.W.; Paton, D.W. 2003. A sediment and organic carbon budget for the greater Strait of Georgia. *Estuarine, Coastal and Shelf Science*, **56**(3-4): 845-860.

Johannessen, S.C.; Masson, D.; Macdonald, R.W. 2006. Distribution and cycling of suspended particles inferred from transmissivity in the Strait of Georgia, Haro Strait and Juan de Fuca Strait. *Atmosphere-Ocean*, **44**(1): 17-27.

Johannessen, S.C.; O'Brien, M.C.; Denman, K.L.; Macdonald, R.W. 2005. Seasonal and spatial variations in the source and transport of sinking particles in the Strait of Georgia, British Columbia, Canada. *Marine Geology*, **216**(1-2): 59-77.

Johannessen, S.C.; Potentier, G.; Wright, C.A.; Masson, D.; Macdonald, R.W. 2008. Water column organic carbon in a Pacific marginal sea (Strait of Georgia, Canada). *Marine Environmental Research*, **66**: S49-S61.

Kirk, J.T.O. 1994. *Light & Photosynthesis in Aquatic Ecosystems. 2^{nd} Ed.* Cambridge University Press, Cambridge, UK. 509 p.

Kostaschuk, R.A.; Luternauer, J.L.; Barrie, J.V.; Leblond, P.H.; Vondeichmann, L.W. 1995. Sediment Transport by Tidal Currents and Implications for Slope Stability: Fraser River Delta, British Columbia. *Canadian Journal of Earth Sciences*, **32**(7): 852-859.

Kostaschuk, R.A.; Luternauer, J.L.; Church, M.A. 1998. Sedimentary Processes in the Estuary. **In**: Clague, J. J.; Luternauer, J. L.; Mosher, D. C. (Ed.). *Geology and Natural Hazards of the Fraser River Delta, British Columbia, Bulletin 525,* Geological Survey of Canada. p. 41-56.

Kowalczuk, P.; Cooper, W.J.; Whitehead, R.F.; Durako, M.J.; Sheldon, W. 2003. Characterization of CDOM in an organic-rich river and surrounding coastal ocean in the South Atlantic Bight. *Aquatic Sciences*, **65**(4): 384-401.

Kowalczuk, P.; Olszewski, J.; Darecki, M.; Kaczmarek, S. 2005. Empirical relationships between coloured dissolved organic matter (CDOM) absorption and apparent optical properties in Baltic Sea waters. *International Journal of Remote Sensing*, **26**(2): 345-370.

Lalli, C.M. and Parsons, T.R. 1997. *Biological Oceanography: An Introduction. 2nd Ed.* Butterworth-Heinemann, Oxford, UK. 314 p.

Laurs, R.M. 1989. *Review of Satellite Applications to Fisheries*. Geoscience and Remote Sensing Symposium, IGARSS '89, 1989. p. 2037-2040

LeBlond, P.H. 1983. The Strait of Georgia - Functional Anatomy of a Coastal Sea. *Canadian Journal of Fisheries and Aquatic Sciences*, **40**(7): 1033-1063.

Levinton, J.S. 2001. *Marine Biology: Function, Biodiversity, Ecology. 2nd Ed.* Oxford University Press, New York, NY. 514 p.

Li, M.; Gargett, A.; Denman, K. 2000. What determines seasonal and interannual variability of phytoplankton and zooplankton in strongly estuarine systems? Application to the semi-enclosed estuary of Strait of Georgia and Juan de Fuca Strait. *Estuarine, Coastal and Shelf Science*, **50**(4): 467-488.

Luternauer, J.L.; Mosher, D.C.; Clague, J.J.; Atkins, R.J. 1998. Sedimentary Environments of the Fraser Delta. **In**: Clague, J. J.; Luternauer, J. L.; Mosher, D. C. (Ed.). *Geology and Natural Hazards of the Fraser River Delta, British Columbia, Bulletin 525,* Geological Survey of Canada. p. 27-39.

Masson, D. and Cummins, P.F. 2004. Observations and modeling of seasonal variability in the Straits of Georgia and Juan de Fuca. *Journal of Marine Research*, **62**(4): 491-516.

Masson, D. and Peña, A. 2009. Chlorophyll distribution in a temperate estuary: The Strait of Georgia and Juan de Fuca Strait. *Estuarine, Coastal and Shelf Science*, **82**(1): 19-28.

McKee, D. and Cunningham, A. 2005. Evidence for wavelength dependence of the scattering phase function and its implication for modeling radiance transfer in shelf seas. *Applied Optics*, **44**(1): 126-135.

Milliman, J.D. 1980. Sedimentation in the Fraser River and its Estuary, Southwestern British Columbia (Canada). *Estuarine and Coastal Marine Science*, **10**(6): 609-633.

Mobley, C.D. 1994. *Light and Water. Radiative Transfer in Natural Waters.* Academic Press, Inc., San Diego, California. 592 p.

Mobley, C.D. 1995. The Optical Properties of Water. **In**: Bass, M. (Ed.). *Handbook of Optics, I,* McGraw-Hill, New York, NY. p. 43.3-43.56.

Mobley, C.D. 2001. Radiative Transfer in the Ocean. **In**: Thorpe, S. A.; Turekian, K. K.; Steele, J. H. (Ed.). *Encyclopedia of Ocean Sciences,* Academic Press, San Diego, CA. p. 2321-2330.

Morel, A. 1991. Light and Marine Photosynthesis - a Spectral Model with Geochemical and Climatological Implications. *Progress in Oceanography*, **26**(3): 263-306.

Morrison, J.; Quick, M.C.; Foreman, M.G.G. 2002. Climate change in the Fraser River watershed: flow and temperature projections. *Journal of Hydrology*, **263**(1-4): 230-244.

Nybakken, J.W. 1988. *Marine Biology: An Ecological Approach. 2nd Ed.* Harper Collins Publishers, New York, NY. 514 p.

Oliver, M.J.; Schofield, O.; Bergmann, T.; Glenn, S.; Orrico, C.; Moline, M. 2004. Deriving *in situ* phytoplankton absorption for bio-optical productivity models in turbid waters. *Journal of Geophysical Research-Oceans*, **109**: C07S11, doi:10.1029/2002JC001627.

Parsons, T.R.; Takahashi, M.; Hargrave, B. 1984. *Biological Oceanographic Processes. 3rd*. Pergamon Press, Oxford, UK. 330 p.

Pawlowicz, R.; Allen, S.; Dower, J.; Lee, R.; Harris, S.; Halverson, M.; Riche, O.; Bird, T. 2004. *STRATOGEM - The Strait of Georgia Ecosystem Project*. **In**: (Ed.). Proceedings of the 2003 Georgia Basin/Puget Sound Research Conference, 2004. http://www.psat.wa.gov/Publications/03_proceedings/PAPERS/ORAL/10d_pawl.pdf

Pawlowicz, R.; Riche, O.; Halverson, M. 2007. The circulation and residence time of the Strait of Georgia using a simple mixing-box approach. *Atmosphere-Ocean*, **45**(4): 173-193.

Pelevin, V.N. and Rutkovskaya, V.A. 1977. On the Optical Classification of Ocean Waters from the Spectral Attenuation of Solar Radiation. *Oceanology*, **17**(1): 28-32.

Pope, R.M. and Fry, E.S. 1997. Absorption spectrum (380-700 nm) of pure water. II. Integrating cavity measurements. *Applied Optics*, **36**(33): 8710-8723.

Preisendorfer, R.W. 1976. *Hydrologic Optics V.1*. U.S. Dept. of Commerce, National Oceanic and Atmospheric Administration, Honolulu, HI. 218 p.

Prieur, L. and Sathyendranath, S. 1981. An Optical Classification of Coastal and Oceanic Waters Based on the Specific Spectral Absorption Curves of Phytoplankton Pigments, Dissolved Organic-Matter, and Other Particulate Materials. *Limnology and Oceanography*, **26**(4): 671-689.

Raymont, J.E.G. 1980. *Plankton and Productivity in the Oceans. Vol. 1: Phytoplankton. 2nd Ed.* Pergamon Press, Oxford, England. 489 p.

Reinart, A.; Arst, H.; Blanco-Sequeiros, A.; Herlevi, A. 1998. Relation between underwater irradiance and quantum irradiance in dependence on water transparency at different depths in the water bodies. *Journal of Geophysical Research-Oceans*, **103**(C4): 7749-7752.

Reinart, A.; Herlevi, A.; Arst, H.; Sipelgas, L. 2003. Preliminary optical classification of lakes and coastal waters in Estonia and south Finland. *Journal of Sea Research*, **49**(4): 357-366.

Roesler, C.S. and Perry, M.J. 1995. In Situ Phytoplankton Absorption, Fluorescence Emission, and Particulate Backscattering Spectra Determined from Reflectance. *Journal of Geophysical Research-Oceans*, **100**(C7): 13279-13294.

Rowan, K.S. 1989. *Photosynthetic pigments of algae*. Cambridge University Press, Cambridge, England. 334 p.

Santos, A.M.P. 2000. Fisheries oceanography using satellite and airborne remote sensing methods: a review. *Fisheries Research*, **49**(1): 1-20.

Sathyendranath, S.; Lazzara, L.; Prieur, L. 1987. Variations in the Spectral Values of Specific Absorption of Phytoplankton. *Limnology and Oceanography*, **32**(2): 403-415.

SATLANTIC 2004. *ProSoft User Manual 7.7*. Satlantic, Inc., Halifax, NS. 59 p.

Schofield, O.; Arnone, R.A.; Bissett, P.; Dickey, T.; Davis, C.; Finkel, Z.; Oliver, M.; Moline, M. 2004. Watercolors in the Coastal Zone. What Can We See? *Oceanography*, **17**(2): 24-31.

Smith, R.C. and Baker, K.S. 1978. Optical Classification of Natural Waters. *Limnology and Oceanography*, **23**(2): 260-267.

Stecko, J.R.P. and Bendell-Young, L.I. 2000. Contrasting the geochemistry of suspended particulate matter and deposited sediments within an estuary. *Applied Geochemistry*, **15**(6): 753-775.

Stockner, J.G.; Cliff, D.D.; Shortreed, K.R.S. 1979. Phytoplankton Ecology of the Strait of Georgia, British Columbia. *Journal of the Fisheries Research Board of Canada*, **36**(6): 657-666.

Stramski, D.; Boss, E.; Bogucki, D.; Voss, K.J. 2004. The role of seawater constituents in light backscattering in the ocean. *Progress in Oceanography*, **61**(1): 27-56.

Sullivan, J.M.; Twardowski, M.S.; Zaneveld, J.R.V.; Moore, C.M.; Barnard, A.H.; Donaghay, P.L.; Rhoades, B. 2006. Hyperspectral temperature and salt dependencies of absorption by water and heavy water in the 400-750 nm spectral range. *Applied Optics*, **45**(21): 5294-5309.

Takahashi, M.; Fujii, K.; Parsons, T.R. 1973. Simulation Study of Phytoplankton Photosynthesis and Growth in the Fraser River Estuary. *Marine Biology*, **19**(2): 102-116.

Thomson, R.E. 1981. Oceanography of the British Columbia coast. *Canadian Special Publication of Fisheries and Aquatic Sciences*, **56**: 291 p.

Tully, J. and Dodimead, A.J. 1957. Properties of the Water in the Strait of Georgia, British Columbia, and Influencing Factors. *Journal of the Fisheries Research Board of Canada*, **14**(3): 241-319.

Twardowski, M.S.; Boss, E.; Macdonald, J.B.; Pegau, W.S.; Barnard, A.H.; Zaneveld, J.R.V. 2001. A model for estimating bulk refractive index from the optical backscattering ratio and the implications for understanding particle composition in case I and case II waters. *Journal of Geophysical Research-Oceans*, **106**(C7): 14129-14142.

Twardowski, M.S. and Donaghay, P.L. 2001. Separating in situ and terrigenous sources of absorption by dissolved materials in coastal waters. *Journal of Geophysical Research-Oceans*, **106**(C2): 2545-2560.

Twardowski, M.S.; Sullivan, J.M.; Donaghay, P.L.; Zaneveld, J.R.V. 1999. Microscale quantification of the absorption by dissolved and particulate material in coastal waters with an ac-9. *Journal of Atmospheric and Oceanic Technology*, **16**(6): 691-707.

Vähätalo, A.V. and Wetzel, R.G. 2004. Photochemical and microbial decomposition of chromophoric dissolved organic matter during long (months-years) exposures. *Marine Chemistry*, **89**(1-4): 313-326.

Vähätalo, A.V.; Wetzel, R.G.; Paerl, H.W. 2005. Light absorption by phytoplankton and chromophoric dissolved organic matter in the drainage basin and estuary of the Neuse River, North Carolina (USA). *Freshwater Biology*, **50**(3): 477-493.

Van Duin, E.H.S.; Blom, G.; Los, F.J.; Maffione, R.; Zimmerman, R.; Cerco, C.F.; Dortch, M.; Best, E.P.H. 2001. Modeling Underwater Light Climate in Relation to Sedimentation, Resuspension, Water Quality and Autotrophic Growth. *Hydrobiologia*, **444**(1-3): 25-42.

Vantrepotte, V.; Brunet, C.; Meriaux, X.; Lecuyer, E.; Vellucci, V.; Santer, R. 2007. Bio-optical properties of coastal waters in the Eastern English Channel. *Estuarine, Coastal and Shelf Science*, **72**(1-2): 201-212.

Vodacek, A.; Blough, N.V.; DeGrandpre, M.D.; Peltzer, E.T.; Nelson, R.K. 1997. Seasonal variation of CDOM and DOC in the Middle Atlantic Bight: Terrestrial inputs and photooxidation. *Limnology and Oceanography*, **42**(4): 674-686.

Waldichuk, M. 1957. Physical Oceanography of the Strait of Georgia, British Columbia. *Journal of the Fisheries Research Board of Canada*, **14**(3): 321-486.

Ware, D.M. and Thomson, R.E. 2005. Bottom-Up Ecosystem Trophic Dynamics Determine Fish Production in the Northeast Pacific. *Science*, **308**(5726): 1280-1284,doi: 10.1126/science.1109049.

WET Labs 2008. *ac Meter Protocol*. WET Labs, Inc., Philomath, OR. 58 p.

Whitfield, P.H.; Wang, J.Y.; Cannon, A.J. 2003. Modelling future streamflow extremes - floods and low flows in Georgia basin, British Columbia. *Canadian Water Resources Journal*, **28**: 633-656.

Wild-Allen, K.; Lane, A.; Tett, P. 2002. Phytoplankton, sediment and optical observations in Netherlands coastal water in spring. *Journal of Sea Research*, **47**(3-4): 303-315.

World Resources Institute 1996. *World Resources 1996-97*. Oxford University Press, New York, NY. 365 p.

Woźniak, B.; Dera, J.; Ficek, D.; Majchrowski, R.; Ostrowska, M.; Kaczmarek, S. 2003. Modelling light and photosynthesis in the marine environment. *Oceanologia*, **45**(2): 171-245.

Yin, K.D.; Harrison, P.J.; Beamish, R.J. 1997a. Effects of a fluctuation in Fraser River discharge on primary production in the central Strait of Georgia, British Columbia, Canada. *Canadian Journal of Fisheries and Aquatic Sciences*, **54**(5): 1015-1024.

Yin, K.D.; Harrison, P.J.; Goldblatt, R.H.; Beamish, R.J. 1996. Spring bloom in the central Strait of Georgia: Interactions of river discharge, winds and grazing. *Marine Ecology Progress Series*, **138**(1-3): 255-263.

Yin, K.D.; Harrison, P.J.; Goldblatt, R.H.; St. John, M.A.; Beamish, R.J. 1997b. Factors controlling the timing of the spring bloom in the Strait of Georgia estuary, British Columbia, Canada. *Canadian Journal of Fisheries and Aquatic Sciences*, **54**(9): 1985-1995.

Zaneveld, J.R.V.; Kitchen, J.C.; Moore, C.C. 1994. The Scattering Error Correction of Reflecting Tube Absorption Meters. **In**: Jaffe, J. S. (Ed.). *Ocean Optics XII, Proceedings of the International Society for Optical Engineering (SPIE), 2258*. p. 44-55.

Zhang, T.; Ramakrishnan, R.; Livny, M. 1997. BIRCH: A new data clustering algorithm and its applications. *Data Mining and Knowledge Discovery*, **1**(2): 141-182.

Appendix A: HPLC Procedure

The method used here was modified from Method 447.0 of the U.S. Environmental Protection Agency (Arar, 1997). This was done in order to accommodate for a larger number of pigment standards instead of only chlorophyll *a* and chlorophyll *b*. Standards of known concentration of 19'-butanoyloxyfucoxanthin, 19'-hexanoyloxyfucoxanthin, alloxanthin, β-carotene, chlorophyll c_2, chlorophyll c_3, diadinoxanthin, fucoxanthin, peridinin, and zeaxanthin were obtained from DHI Water & Environment (Denmark). Chlorophyll *a* and chlorophyll *b* stock standard solutions were made using dry standards obtained from Sigma (Canada). Major differences with regard to Method 447.0 were:

- Eluent A: 75% (v/v) methanol / 20% 0.5 M ammonium acetate. The ammonium acetate solution was filtered through a 0.45 μm filter before being mixed with methanol;
- Eluent B: 85% (v/v) acetonitrile / 15% DI;
- The procedure ended up being 35 min long according to the gradient below:

Time (min)	Flow (mL min^{-1})	Eluent A (%)	Eluent B (%)	Eluent C (%)
0.0	1	100	0	0
2.0	1	0	100	0
20.0	1	0	31	69
27.0	1	0	100	0
30.0	1	100	0	0
35.0	1	100	0	0